UNIVERSIDAD DE CHILE
FACULTAD DE CIENCIAS FÍSICAS Y MATEMÁTICAS
DEPARTAMENTO DE INGENIERÍA ELÉCTRICA

DEGRADATION OF THE GLOBAL NAVIGATION SATELLITE SYSTEM POSITIONING ACCURACY CAUSED BY IONOSPHERIC DISTURBANCE SOURCES

TESIS PARA OPTAR AL GRADO DE DOCTOR EN INGENIERÍA ELÉCTRICA

JUAN CARLOS VALDÉS ABREU

PROFESOR GUÍA:
MARCOS DÍAZ QUEZADA

MIEMBROS DE LA COMISIÓN:
CESAR AZURDIA MEZA
MARINA STEPANOVA
JUAN VALDIVIA HEPP
JUAN BAEZ SOTO
MANUEL BRAVO SEPULVEDA

Este trabajo ha sido parcialmente financiado por National Agency for Research and Development (ANID)/Scholarship Program/Doctorado Nacional/2018: 21181599

SANTIAGO DE CHILE
2023

RESUMEN DE LA TESIS PARA OPTAR AL GRADO DE
DOCTOR EN INGENIERÍA ELÉCTRICA
POR: JUAN CARLOS VALDÉS ABREU
FECHA: 2023
PROF. GUÍA: DR. MARCOS DÍAZ QUEZADA

DEGRADACIÓN DE LA PRECISIÓN DE POSICIONAMIENTO EN EL SISTEMA GLOBAL DE NAVEGACIÓN POR SATÉLITE DEBIDO A FUENTES DE PERTURBACIÓN IONOSFÉRICA

Las perturbaciones ionosféricas son un problema importante para los sistemas de radiocomunicación y navegación basados en el espacio. Los cambios ionosféricos pueden perturbar al Sistema Global de Navegación por Satélite (GNSS) porque está basado en radioenlaces. Esta investigación proporciona una metodología para evaluar la degradación de la precisión GNSS debido a fuentes de perturbaciones ionosféricas. La metodología estandariza los datos para facilitar la comparación entre diferentes perturbaciones ionosféricas. El estudio se basa en el contenido total de electrones (TEC) ionosférico y los errores de posicionamiento utilizando receptores GNSS alrededor del mundo. Los mapas ionosféricos globales se crearon utilizando la interpolación Kriging ordinaria. La posición aparente se obtuvo usando posicionamiento de punto preciso con resolución de ambigüedades. Este trabajo presenta la evaluación de los efectos causados por actividades geomagnéticas y un eclipse solar sobre la precisión GNSS. Las actividades geomagnéticas causaron mayores errores en magnitud que el eclipse, pero el eclipse aumentó el tiempo de convergencia de los receptores. Los errores fueron más severos durante variaciones ionosféricas en ambas crestas de la Anomalía de Ionización Ecuatorial (Caribe y Sudamérica) y en la Anomalía Magnética del Atlántico Sur. Los efectos también fueron notorios en la costa oeste Sudamericana (Chile) y Norteamérica.

ABSTRACT OF THE THESIS FOR THE DEGREE
OF DOCTOR IN ELECTRICAL ENGINEERING
AUTHOR: JUAN CARLOS VALDÉS ABREU
DATE: 2023
ADVISOR: DR. MARCOS DÍAZ QUEZADA

DEGRADATION OF THE GLOBAL NAVIGATION SATELLITE SYSTEM POSITIONING ACCURACY CAUSED BY IONOSPHERIC DISTURBANCE SOURCES

Ionospheric disturbances are a major problem for space-based navigation and radiocommunication systems. Global Navigation Satellite System (GNSS) can be perturbed by ionospheric changes because it is a radio-link-based system. This research provides a methodology to evaluate the degradation of the GNSS positioning accuracy caused by ionospheric disturbance sources. The methodology enables data standardization to facilitate the comparison between different ionospheric disturbances. The study is based on ionospheric total electron content (TEC) and positioning errors using GNSS receivers around the world. The global TEC maps were created using ordinary Kriging interpolation and the apparent position was obtained using the precise point positioning with ambiguity resolution mode. This work presents the evaluation of the effects of geomagnetic activities and a solar eclipse on georeferencing precision using the methodology proposed. While the magnitude errors due to geomagnetic activities were larger than those caused by the solar eclipse, the impacts of the eclipse lengthened the GNSS receivers' convergence times. The positioning errors were more severe during ionospheric changes in both crests of the Equatorial Ionization Anomaly region (Caribbean and South America) and in the South Atlantic Magnetic Anomaly. The effects were also notorious on the west coast of South America (Chile) and North America.

Por ser quienes más me han amado, los que me dieron la vida y los deseos de vivir. Por guiarme y aconsejarme. Por siempre confiar en mí, estar a mi lado y darme fuerzas cuando no había esperanzas. A ustedes, mamá y papá, por batallar a mi lado hasta el final.

Delfina Abreu Séneca, 18 de Octubre de 1954 a 28 de Febrero de 2009.

Juan Valdés Lameré, 6 de Noviembre de 1948 a 12 de Julio de 2010.

A la memoria de mis mayores y de Luis Cimino Quiñones.

¡Qué su luz siempre me guíe y acompañe!

Agradecimientos

A mis padres Delfina y Juan, a quienes les debo lo que soy y seré, lo estaré eternamente. A mis abuelos. A Cimino, por las lecciones, experiencia, intercambios durante tantos años, por ser mi segundo padre, mi tutor permanente y ejemplo a seguir.

A mi esposa, novia, compañera, amiga y mi amor: Yohadne. Muchas gracias por su amor, dedicación, comprensión, apoyo incondicional en todo momento y paciencia en momentos difíciles, por su trabajo. A Miriam, Yennis, Jennifer (nuestra princesa), Alina, Hilda y Humberto por su fe, alegría, apoyo y energía y confianza.

A mi advisor Marcos Díaz a quién aprecio y admiro por su trayectoria, su profesionalidad e inteligencia. A Patty, Espe y a su familia por acogernos y hacernos sentir en familia. Gracias por el apoyo incondicional, los recursos, el tiempo invertido y por ser no solo testigos, sino también partícipes de la realización de este sueño.

Evelyn Elisa y José Alejandro por toda su colaboración, esfuerzo, visión e impulso para el despegue inicial. A Daniel, Rodolfo (Fito), Osmell, Reiniel, Danilo, María Felicia, Anneris, Gabrielito, Erena, Emilio, Andy Luis Romero, Williams Roig, Ismelis Iglesias, Jorge Mario, Ana Laura y Ana Doris. A todos por siempre estar en los buenos y malos momentos, por todo su apoyo incondicional y comprensión durante tanto tiempo.

Alex Becerra, Camilo Rojas, Carlos González, Cristobal, Elías, Fernanda, Francisco Anguita, Gerardo, Gustavo, Ignacio, Isis, Javier Rojas, Jose Ogalde, José Pedreros, Julian, Matías Vidal, Miguel Martínez, Rodrigo Muños, Rodrigo Silva, Samuel Gutiérrez, Tamara, a todos los miembros del SUCHAI y de SPEL por todo su cariño, apoyo y por cada momento compartido. Aunque hace tiempo que no nos vemos, todos han contribuido a mi desarrollo personal y profesional, me han hecho sentir en casa y me han ayudado a combatir el gorrión.

A Cesar Azurdia, Claudio Pérez, Cristina, Diego Reyes, Jorge Silva, Juan Alejandro Valdivia, Juan Pérez, Loreto Soto, Marina Estepanova, Miguel Patiño, Mileana, Mónica Lipari, Patricio Mena, Sandra Céspedes, Alexis Yañez, Erika Latorre, al personal de postgrado, al personal docente y no docente del DIE, de la U. Chile y de la USACH; porque su apoyo y aporte, son vitales en mi formación como profesional.

A Manuel Bravo, el primero que me guió en el procesamiento de datos GNSS y siempre estar disponible. A Juan Carlos Báez por siempre estar, por sus invaluables aportes, por su apoyo científico–técnico y personal. A Rodrigo Severino, por su valiosos consejos sobre el tratamiento de datos y apoyo logístico. A Gopi Seemala, Ciraolo por sus sugerencias sobre

el TEC. A Yury Yasyukevich por recomendar nuestras investigaciones. A Loreto Arriagada, GEOCOM y SIRGAS por los talleres y seminarios. A Claudio Brunini por su colaboración.

A Alex Echeverría, Cristopher, Daniel Montofre, Javiera Meneses, Matías Sandoval, Nicolás Ortega, Nicolás Ramos, Sebastián Sepúlveda, Rosa Andrea Cisterna, Hernán Hernández, Lisset, Paulo Sentegui, Raquel (Bu), Samuel Montejo, Vanesa y fundamentalmente a Sandy por todos sus por sus consejos y guía. A Raydel (Pepillo) porque después del largo camino, después superar el primer baneo, salimos, llegamos, cumplimos, vencimos y vimivos.

A Pedro Luis García, Jorge Luis Chiroldes, Juan Carlos Céspedes, Alain, Tahirí, a los miembros de SELPER-Cuba y la Union Nacional de Ingenieros y Arquitectos de la Construcción de Cuba, por la confianza, consejos personales y profesionales, recursos y dedicación para potenciar los proyectos satelitales. A los miembros de la Cátedra Aeroespacial del InSTEC. A Francisco Mendieta y Carlos Duarte de la Agencia Espacial Mexicana.

A María del Carmen, Sandianes, Marante, Amado, Arzola, Céspedes, Véliz, Justo, Oscar, Lesly, a mis profesores y compañeros de la Universidad Tecnológica de La Habana (Cujae); por brindarme conocimientos y afianzar el amor a mi especialidad. A mis estudiantes.

A las personas especiales que nos dejaron recientemente y no pudieron ver la culminación de este trabajo. Al profe José Ángel Amador (CO2JA), por su total apoyo en tiempo, consejos personales y profesionales, su ayuda y confianza en los momentos críticos, por sumarse activamente en nuestros proyectos satelitales. A Juan Hierrezuelo por sus enseñanzas y consejos. A la profe Mirna, por su cariño, preocupación, por ser mi tutora anímica y espiritual. A Sara, personal de apoyo de la Cujae, por sus recomendaciones, su cariño y ánimo.

A las becas y fondos científicos que apoyaron este trabajo: National Agency for Research and Development (ANID)/Scholarship Program/Doctorado Nacional/2018–21181599 (CONICYT Doctoral Grant Number 21181599); Anillo 10677, ACT1405; ANID–FONDECYT grants 1151476, 1211144, 1221907; ANID AFB180004; Air Force Office of Scientific Research under award numbers FA9550–18–1–0249, FA9550–20–1–0189 y FA9550–19–1–0384.

A los centros e instituciones por poner a disposición del público datos como los que se utilizaron en este trabajo, tales como: el Centro Sismologico Nacional de la Universidad de Chile (CSN); Red Argentina de Monitoreo Satelital Continuo (RAMSAC); Instituto Brasileiro de Geografia e Estatística (IBGE); International GNSS services (IGS); UNAVCO; Geoscience Australia; African Geodetic Reference Frame (AFREF); Low-Latitude Ionospheric Sensor Network (LISN); CDDIS y OMNIWeb Plus Data Documentation de la NASA; AIUB Data Center of Bern University in Switzerland; GFZ Helmholtz Centre Potsdam; WDC for Geomagnetism, Kyoto; ESA´s Swarm mission; USGS Earthquake Hazards Program; Precise Point Positioning of Canadian Spatial Reference System (CSRS-PPP).

En fin, de corazón agradezco a todos los que apoyaron este trabajo doctoral, en un sentido o en otro, porque todo lo vivido me ha hecho más fuerte. Además, me ha otorgado mayor desarrollo profesional y personal lo que me permitirá contribuir de manera efectiva a la creación de nuevos conocimientos, investigaciones y a la formación de las nuevas generaciones.

¡Muchas gracias!

Table of Content

List of Tables

List of Figures

List of Acronyms

3D-RMS	3D positioning root mean square
AE	Auroral Electrojet index
AFREF	African Geodetic Reference
AGW	Atmospheric Gravity Waves
AIUB	Data Center of Bern University in Switzerland
Ap	Daily averaged geomagnetic activity
APPS	Automatic Precise Point Service
C1	Start of partial eclipse
C4	End of partial eclipse
CDDIS	Crustal Dynamics Data Information System
CME	Coronal Mass Ejection
CSN	National Seismological Center at University of Chile
CSRS-PPP	Precise Point Positioning of Canadian Spatial Reference System
DCB	Differential Code Biases
DF	Dual-Frequency
DF-GNSS	Dual-Frequency Global Navigation Satellite System
DoY	Day of year
Dst	Disturbance storm time index
DVTEC	Differential vertical total electron content
EIA	Equatorial Ionization Anomaly
EQ	Earthquake
ESA	European Union Agency
foF2	Critical frequency of the plasma
GAPS	GNSS Analysis and Positioning Software
GDGPS	Global Differential GPS
GE	Greatest eclipse
GNSS	Global Navigation Satellite System
GPS	Global Positioning System
hmF2	Height of maximum electron concentration
HPH	High Potential Hazard
HPI	High Potential Incident

IBGE	Institute of Brazilian Geography and Statistics
IGS	International GNSS Service
IMF-Bz	Z component of Interplanetary Magnetic Field
INS	Inertial navigation systems
IPP	Ionospheric Pierce Point
Kp	Planetary K-index
LEO	Low Earth Orbit
LISN	Low-Latitude Ionospheric Sensor Network
LP	Langmuir probe
MOT	Eclipse maximum obscuration time
MPO	Maximum percentage of obscuration
Mw	Moment magnitude
NASA	National Aeronautics and Space Administration
NAVSTAR-GPS	Navigation System using Timing and Ranging Global Positioning System
Ne	Electron density
P1	First external contact
P4	Last external contact
PPP	Precise Point Positioning
PPP-AR	Precise Point Positioning with ambiguity resolution
PRN	Pseudo Random Noises
RAMSAC	Argentine Continuous Satellite Monitoring Network
RINEX	Receiver Independent Exchange
RMS	Root mean square
RNSS	Radio navigation satellite service
ROT	Rate of TEC
ROTI	Rate of change of the TEC Index
SA	Selective Availability
SAMA	South Atlantic Magnetic Anomaly
SC	Solar cycle
STEC	Slant total electron content
SYM-H	Longitudinally Symetric Horizontal component disturbance
TAD	Traveling Atmospherics Disturbances
TEC	Total electron content
TECu	Total electron content unit
TID	Traveling Ionospheric Disturbances
UAV	Unmanned Aerial Vehicles
UNAVCO	University NAVSTAR Consortium
UT	Universal Time
VTEC	Vertical total electron content
WDC	World Data Center

Chapter 1

Introduction

This Chapter gives the motivations of work (Section 1.1); the problem to be explored (Section 1.2). Section 1.4 defines the overarching objectives and specific aims. Section 1.5 describes the significance and the practical outcomes and contributions of this research. Section 1.6 outlines the remaining chapters of this manuscript.

1.1 Motivation

Radio waves have become increasingly vital in satellite communication and radionavigation infrastructure in recent times. A radionavigation satellite service (RNSS) is a set of satellites that use radio waves to provide a service of geolocalization or radionavigation. The Global Navigation Satellite System (GNSS) is an example of radionavigation satellite service and it is, in essence, a communications system space-Earth [1]. GNSSs are constellations made up of several satellites, e.g. the United States' NAVSTAR-GPS (Navigation System using Timing and Ranging Global Positioning System), Russia's GLONASS (Global Navigation Satellite System), European Union's Galileo, and China's BeiDou that transmit data about their spatial and temporal location [2, 3]. These data are transmitted at different frequencies in L band and they are received by satellite observation instruments. The data can be processed in real-time or post-process.

Modern society, industry, and science use GNSS-based technologies more and more often: GNSS-based operations of the unmanned airborne, floating, and land vehicles, GNSS assisted landing procedures for commercial aviation, GNSS positioning for rescue operations, estimating the route using smartphone GNSS data [4], GNSS sport watches [5], etc. (Fig. 1.1).

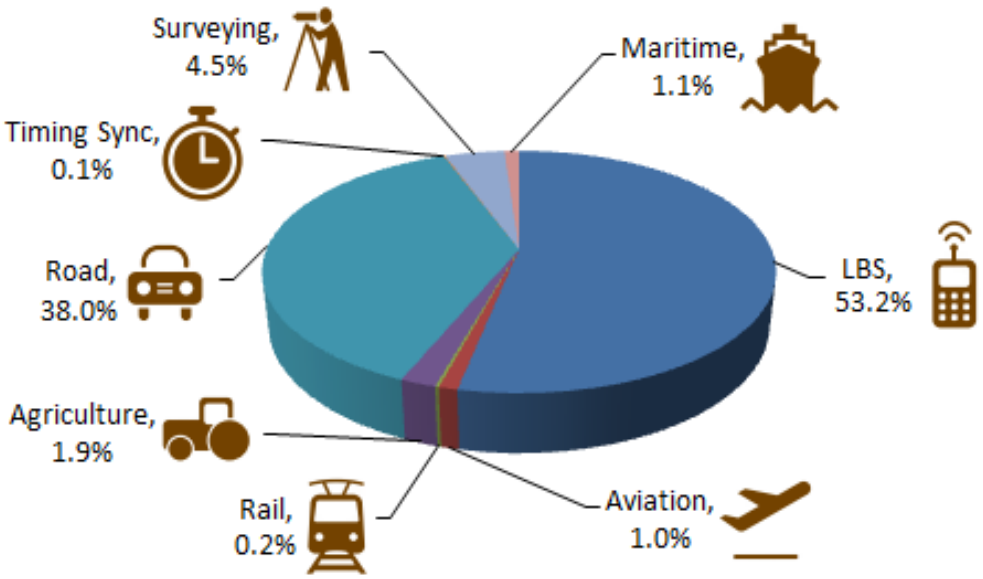

Figure 1.1: Distribution of cumulative global revenue from GNSS chipset sales projected for the 2013–2023 period (Adapted from Teunissen and Montenbruck [1]).

GNSS has different applications in areas such as [6, 7, 8]:

- Fiscal control, border surveillance, and other defense tasks.
- In the emergency services, in the monitoring and control of forest fires.
- Assist firefighters and rescuers in search and rescue work, as well as in the transfer of emergency material.
- Security, such as remote monitoring and surveillance devices.
- In agribusiness, it allows, among others, the monitoring and supervision of precision agriculture tasks.

The use of GNSS, through an unmanned aerial vehicle (UAV), commonly known as a drone, represents a great alternative in high-risk or difficult-to-access areas. In engineering, drones collaborate in supervision tasks even in large projects; while in mining, they are a solution to perform tasks that until recently were very dangerous for mining officials [9, 10].

Vehicular Ad-hoc Networks use GNSS to obtain accurate location information in combination with laser scanners, inertial navigation systems (INS), radar, and/or other sensors [11, 12, 13, 14, 15, 16]. These combinations are used in a wide variety of applications such as UAV to operate autonomously, tracking vehicle fleets, cargo, rental vehicles, bank cash vans, etc. Devices receiving GNSS information have access to precise location information as well as extremely accurate time data required by law [17]. A key application is the ability to respond quickly to an emergency or contingency issue.

GNSS kinematic solutions started to play an essential role in seismology because they proved the capability of GNSS to resolve seismic waves generated by moderate-to-strong earthquakes at distances of a few kilometers up to thousands of kilometers [18].

GNSS has different applications in Chile, among which are [19, 20]:

- The possibility of controlling and managing vehicle fleets, in accordance with international standards, knowing the kilometers traveled or the routes used
- Manage the safety of people and assets, monitoring the instantaneous location and status of any asset, making it easy to recover a vehicle in the event of theft or unauthorized use. An example is mining which is affected by the theft of machinery.
- Optimize operations, it allows to measure, control and optimize all activities.
- Another application is to alert about possible collisions or audit cases of possible accidents by analyzing reports of HPI (High Potential Incident) and HPH (High Potential Hazard) events. GNSS is already implemented at mining sites, such as those of Anglo American, BHP Billiton, Antofagasta Minerals, Minera Los Pelambres, Codelco, etc.
- Also in exploration, as well as in forestry tasks, where in addition to security devices, having a global positioning system, reports can be reviewed or received in real-time and thus comply with the security requirements required by law.
- A key application is the ability to respond quickly to an emergency or contingency issue.

The applications described above and others are greatly affected by the errors that the GNSS position, which can mean a difference in its use, causing a high economic and social impact. Many error sources affect positioning using GNSS, such as clock offsets, multipath, and the receiver. However one of the largest errors in GNSS positioning is attributable to the delay in the atmosphere. The GNSS signal from the satellite traverses through the vacuum of space until it reaches the Earth's atmosphere. The GNSS signal experiences refraction, diffraction, and a decrease in the apparent speed upon reaching the Earth's atmosphere, in particular the ionosphere. Subsequently, this induces an apparent delay in the transit time of the signal from the satellite to the receiver [21, 22]. Then, ionospheric variability is one of the main threats to GNSS-based techniques such as ionospheric parameter measurement and precise positioning.

The ionosphere is the part of the Earth's upper atmosphere starting in the mesosphere and extending beyond the thermosphere and ranging from 60–1000 km in altitude (Fig. 1.2). This layer is the ionized part of the atmosphere and consists of free electrons and positively charged ions (atmospheric plasma); it is less than 0.1% the mass of the atmosphere.

Total electron content (TEC) is a parameter needed in corrections for propagation effects of the ionosphere in some radio system applications [24]. This parameter is one of the physical parameters to characterize the spatial and temporal structure, and variability of the ionosphere [25, 26]. The TEC in the atmosphere is defined as the number of free electrons contained in a column of the atmosphere of unit area, and it is expressed in TEC units (TECu), where 1 TECu = 10^{16} e/m^2. TEC value calculation is usually based on GNSS data. TEC shows the electron content from the satellite to the ground. It is assumed that TEC variations reflect the changes in the ionospheric F-region because the main contribution to the electron content is mostly provided by F-region [27, 28].

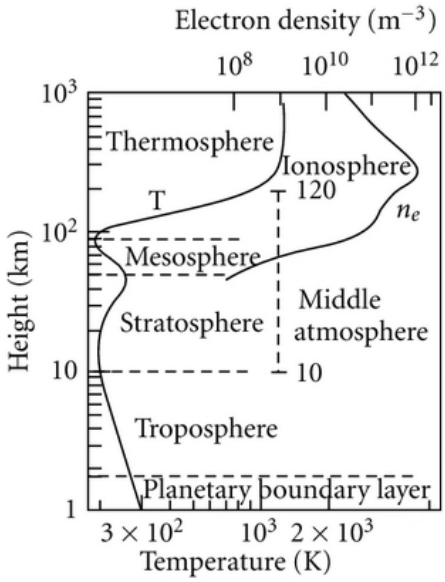

Figure 1.2: Layers of the atmosphere: troposphere, stratosphere, mesosphere, and thermosphere (Adapted from Singh, et. al [23]).

1.2 Statement of Problem

The ionospheric TEC disturbances can be caused by different sources, such as, solar terminator [29], solar flares [30, 31, 32], geomagnetic storms [33, 34], solar eclipses [29, 35], thunderstorm/lightning [36, 37, 38], tropical cyclones [29, 34, 39], earthquakes [34, 40, 41], volcanic eruptions [42, 43], tsunamis [44, 45], rocket launches [29], etc. These sources of ionospheric disturbances are a major problem for space-based communication and navigation systems.

Perturbations in the ionosphere, in particular electrons, can produce disturbances in space-based technology and its products, such as communication disruptions due to refraction, dispersion, Faraday rotation, fading, and group delay [46]. Then, ionospheric disruption sources constitute a significant problem for space-based navigation and communication systems. However, GNSS can be perturbed by ionospheric changes because it is a radio-link-based system. The literature review showed that GNSS receivers positioning performance is degraded in the presence of these source occurrences, such as geomagnetic storms, solar eclipses, earthquakes, and tsunamis, among others.

Solar activity is one of the most important drivers of ionospheric variations on a global scale. Also, during a geomagnetic storm, the ionosphere can be greatly perturbed through the Sun-solar wind-magnetosphere-ionosphere-atmosphere coupling process. But there are not many studies related to the impact of the GNSS positioning accuracy of a moderate geomagnetic storm. Moreover, a solar eclipse causes regular ionospheric effects that are not yet fully understood. Few authors have analyzed the GNSS positioning errors caused by the influence of solar eclipses. Enhancements, depletions, and/or oscillations in the ionospheric TEC influence the signal between a satellite (GNSS/communication) and a receiver. In particular, the signal delay is affected differently depending on the signal frequency, resulting in a reduction in the accuracy of multifrequency GNSS receivers.

Additionally, given the tendency to include teleoperated and/or autonomous (ground, maritime, and aerial) applications and other high-precision activities in several industries around the world, the performance of the technology supporting this activity needs to be carefully reviewed. One of those systems' most important components is the GNSS, which enables receiver localization virtually anywhere around the globe. Mining, agriculture, and fishing are all key economic activities in Chile that are exploring the transition to a more teleoperated or autonomous operation. Due to this necessity, it is crucial to investigate the robustness of the GNSS throughout the country especially when ionospheric disturbance sources are generated.

On other hand, in South America (Chile sector), there is a high occurrence of earthquakes (EQs) of great magnitude that can disturb the ionosphere. Furthermore, the estimation of the positioning of GNSS receivers in this country is also affected by the behavior of the Equatorial Ionization Anomaly (EIA) [47, 48, 49], the South Atlantic Magnetic Anomaly (SAMA) [50, 51, 52], the Weddell Sea Anomaly [53], and the gravity waves over the Andes Mountains [54, 55] that alter their behavior in response to the presence of sources of ionospheric disturbance like those listed above (intensifying and/or weakening).

Moreover, December 2019 marked the start of Solar Cycle 25 (`https://www.weather.gov/news/201509-solar-cycle`, last accessed on 2 July 2022). The solar cycle is the cycle that the Sun's magnetic field goes through approximately every 11 years. During solar maximum, geomagnetic storms occur more often, and their frequency fluctuates with the sunspot cycle. The geomagnetic and geophysical conditions during Solar Cycle 25 are shown in Annex A (see Figure A.1, and Table A.1). Then, the new solar cycle is critical to unraveling the relationship between solar activity and positioning errors in the GNSS receivers thanks to a large number of GNSS stations available around the world, gathering relevant data. Therefore, a methodology is needed to process the data in a standardized manner that facilitates comparison between different cycles and kinds of disturbance ionospheric sources.

1.3 Hypotheses

1. Ionospheric TEC disturbances produce GNSS positioning estimation errors in magnitude and duration.
2. The degradation of GNSS positioning accuracy has different distinguishing features depending on the source that caused the ionospheric disturbance.
3. There is a bidirectional relationship between TEC changes and the occurrence of GNSS positioning errors.

1.4 Objectives

1.4.1 General Objective

The main objective of this doctoral thesis is to provide a methodology to evaluate the degradation of the Global Navigation Satellite System positioning accuracy caused by ionospheric disturbance sources, such as geomagnetic storms and solar eclipses.

1.4.2 Specific Objectives

1. To propose a methodology to study the GNSS positioning errors caused by ionospheric disturbance sources.
2. To evaluate the proposed methodology by studying the effects that a moderate geomagnetic storm has over the GNSS georeferencing precision red in terms of magnitude and duration.
3. To analyze the ionospheric behavior during a solar eclipse and its impact on GNSS positioning accuracy in terms of magnitude and duration by applying the presented methodology.
4. To compare contributions to the degradation of GNSS positioning accuracy due to a geomagnetic storm and a solar eclipse.

1.5 Contributions

In literature, ionospheric most studies focus on the climatology of the occurrence of ionospheric irregularities. However, few works provide a quantitative performance analysis of GNSS positioning errors in magnitude and duration as a function of TEC disturbances. Therefore, the presentation of this analysis to the scientific community is a great contribution to the country's science.

GNSS positioning errors can be used to estimate the robustness of L-band communications during ionospheric disturbances. Because GNSS positioning accuracy depends on the quality of the signal reaching the GNSS receiver, which can be affected by refraction, dispersion, fading, and group delay, among others, provoked by the ionospheric variations according to Recommendation ITU-R P.531 [46]. Furthermore, the TEC behavior allows quantitative estimation of the effects of ionospheric changes on radiocommunications. Therefore, the present thesis proposes a new methodology to process the data in a standardized manner that facilitates the comparison of ionospheric TEC changes and GNSS positioning between different cycles and kinds of ionospheric disturbance sources.

Regarding the data processing methodology, the present work contributes fundamentally to the interpretation of the data. Consequently, it will help advance understanding of how the Equatorial Ionization Anomaly and the South Atlantic Magnetic Anomaly can affect GNSS georeferencing accuracy during geomagnetic storms and solar eclipses.

On the other hand, the present work contributes to the study of the induced effects on the ionosphere due to geomagnetic storms and solar eclipses. The work is also important because it will provide a better understanding of the processes that control the ionosphere and that can cause GNSS positioning errors.

In addition, this doctoral research creates a new research niche in various areas, such as the study and modeling of ionospheric disturbances in the radio communication channels; the analysis of the robustness of the mobile-satellite service during ionospheric disturbances; and the identification of the type of ionospheric disturbance source according to the magnitude of the positioning errors.

1.6 Outlines

This doctoral thesis is organized according to "Format 2: New optional doctoral thesis format based on two accepted/published WoS/ISI journal papers" (https://www.die.cl/sitio/proceso-de-doctorado/, last accessed 29 June 2022).

As a result of this doctoral thesis, two WoS/ISI journal papers were published. As Format 2 requires, the Chapters 2 and 3 contain articles related to the effects on GNSS positioning due to the 12 May 2021 geomagnetic storm and the 10 June 2021 solar eclipse, respectively. General conclusions of this thesis and future work are presented in Conclusions. Finally, Annex B presents the supplemental materials of the paper related to the solar eclipse.

Chapter 2

Effects of the 12 May 2021 Geomagnetic Storm on Georeferencing Precision

In this work, we present the positioning error analysis of the 12 May 2021 moderate geomagnetic storm. The storm happened during spring in the northern hemisphere (fall in the south). We selected 868 GNSS stations around the globe to study the ionospheric and the apparent position variations. We compared the day of the storm with the three previous days. The analysis shows the global impact of the storm. In the quiet days, 93% of the stations had 3D errors less than 10 cm, while during the storm, only 41% kept this level of accuracy. The higher impact was over the Up component. Although the stations have algorithms to correct ionospheric disturbances, the inaccuracies lasted for nine hours. The most severe effects on the positioning errors were noticed in the South American sector. More than 60% of the perturbed stations were located in this region. We also studied the effects produced by two other similar geomagnetic storms that occurred on 27 March 2017 and on 5 August 2019. The comparison of the storms shows that the effects on position inaccuracies are not directly deductible neither from the characteristics of geomagnetic storms nor from enhancement and/or variations of the ionospheric plasma.

Keywords: global navigation satellite system; geomagnetic storms; global positioning system; precise point positioning; total electron content; rate of change of the TEC index

2.1 Introduction

The tendency to incorporate autonomous or tele-operated systems in certain industries around the globe requires careful analysis over the performance of the technology that supports this activity. One of the key elements in those systems is the global navigation satellite system (GNSS), which allows the geolocation of a receiver almost anywhere in the world. However, GNSS as a radio-link-based system can be perturbed by variations in the ionosphere. In particular in Chile, mining, fishing, and agriculture activities are relevant economic sectors in Chile that are exploring the migration to a more tele-operated/autonomous operation. Due to this requirement, it is imperative to study the robustness of the GNSS systems along the country, in particular when geomagnetic storms are produced.

One of the most important drivers of ionospheric variations at a global scale is solar activity. During a geomagnetic storm, the ionosphere can be greatly perturbed through the Sun–solar wind–magnetosphere–ionosphere–atmosphere coupling process. Perturbations in the ionosphere, in particular electrons, can produce disturbances in space-based technology and their products such as communication disruptions and imprecision in the positioning estimation of global navigation satellite system (GNSS). The enhancement or oscillations in the ionospheric electron content influence the signal between a satellite (GNSS/communication) and a receiver. In particular, the signal delay is affected differently depending on the signal frequency, resulting in a reduction in the accuracy of multifrequency GNSS receivers.

A geomagnetic storm is a major temporary disturbance in the Earth's magnetic activity and is associated with solar activity, e.g., coronal mass ejection (CME) and high-speed solar wind stream (HSS) [56]. When there is greater solar activity, geomagnetic storms are mainly generated by CME, while during moments of less solar activity, it is the coronal holes that have a dominant effect [57]. Geomagnetic storms occur when there is a large sudden change in the solar wind dynamic pressure at the magnetopause [58]. The distinctive characteristic of a geomagnetic storm is a clear decrease in the horizontal intensity of the magnetic field [58]. Geomagnetic storms can be usually divided into three main phases: initial, main, and recovery [59, 60, 61]. The geomagnetic storms are detected prior to the ionospheric disturbances and to the decrease in positioning estimation.

Different geomagnetic indices are used to characterize geomagnetic storms such as the disturbance storm time (Dst) index, geomagnetic disturbance (Kp), averaged geomagnetic activity (Ap) (based on data from a set of specific Kp stations), and the auroral electrojet (AE) index, where the Dst-index is associated with the effects on the equatorial region, the Kp-index to the midlatitudes, and the AE-index at high latitudes since it characterizes the intensity of ionospheric currents during magnetic storms and substorms activity [62, 63]. The Dst-index has been used historically to characterize the severity of a geomagnetic storm. Depending on the Dst value, the storms are usually classified in ranges such as weak (-30 nT and -50 nT), moderate (-50 nT and -100 nT), intense (-100 nT and -200 nT), very intense (-200 nT and -350 nT), and great (Dst below -350 nT) [58, 59, 64, 65]. Furthermore, the Kp-index is based on 3 hour measurements from ground-based magnetometers around the world (`https://www.spaceweatherlive.com/`, accessed on 6 December 2021). The storms are usually classified as minor (G1) with a Kp = 5; moderate (G2) with a Kp = 6; strong (G3) with a Kp = 7; severe (G4) with Kp = 8, and extreme (G5) with Kp = 9 (`https://www.swpc.noaa.gov/noaa-scales-explanation`, accessed on 6 December 2021) [65, 66]. The Ap-index provides a daily average level for geomagnetic activity. The Kp-value converts a linear scale called the a-index. The average from eight daily a-values gives us the Ap-index of a certain day. Thus, high levels of geomagnetic activity have a higher daily Ap-value (`https://www.swpc.noaa.gov/noaa-scales-explanation`, accessed on 6 December 2021) [66].

The AE-index was originally introduced by Davis and Sugiura [62] as a measure of global electrojet activity in the auroral zone. The AE-index is derived from measurements of the horizontal components (H-components) of the Earth's magnetic field obtained from a series of observatories along the auroral zone in the northern hemisphere [62, 63, 67]. The AE-index is estimated as AE=AU-AL, where AU and AL indexes are obtained from the upper and

lower envelope of the superposed H-components [62, 67]

The geomagnetic storms can also be identified by various other parameters such as the symmetric disturbance of the magnetic field H (SYM-H); the interplanetary electric field (IEF); and the interplanetary magnetic field (IMF), where IMF-Bz is the most important parameter for the study of geomagnetic storms, as the energy input into the magnetosphere, depends on Bz orientation and its magnitude [68]. Although these indexes provide extra information regarding the space conditions, some of them are related to the Dst-index. For instance, a relationship has been shown between Dst and Bz [69].

The response of the ionosphere to geomagnetic induced disturbances is known as ionospheric storm [30, 70]. Ionosphere plasma density is mainly determined by the chemistry/composition, transport due to electric field, transport due to neutral wind, and transport due to ambipolar diffusion. During geomagnetic storms, the variations of chemistry or the thermospheric composition, and the interaction with the neutrals (neutral wind) [71, 72], and/or variations of electric field and ambipolar diffusion [73] are the final cause that alters the ionosphere plasma density. Nevertheless, the response of the ionosphere during a geomagnetic storm is complex and difficult to predict accurately, and the physical nature of many underlying mechanisms needs a better understanding to obtain precise forecasting of its behavior based on geomagnetic storms parameters [74]. In addition, the effects of these physical processes on the ionosphere have also been reported to vary with solar activity, storm intensity, storm duration, season, location, local time, and altitude of the observing station, which increases the forecast uncertainties [61, 75, 76, 77, 78, 79, 80, 81]. For instance, Tsurutani et al. [82] and Mannucci et al. [83] have found that the response of the ionosphere to geomagnetic activity depends on the season of the year in which that portion of the ionosphere is located [84, 85].

The ionospheric plasma density can be estimated by estimating the ionospheric electron density. Thus, it is the determining variable for investigation of the spatial and temporal variations in the ionosphere. The total electron content (TEC), which can be estimated from double-frequency GNSS receiver data, is used to study the ionospheric response during ionospheric storms [56, 58, 64, 86, 87, 74]. The TEC is defined as the integral of the electron density from the ground height up to the ceiling height, i.e., the height of the transmitting satellite or infinity. Since the contribution to the TEC usually comes from low orbital altitudes (below 1000 km), then, vertical TEC (VTEC) is obtained from Slant TEC (STEC) at the ionospheric pierce point (IPP) at an altitude of 350 km. Another relevant ionospheric index used to study ionospheric variations is the rate of change of the TEC index (ROT). ROT is calculated in a temporal window. ROTI is defined as the standard deviation of ROT. It describes the small-scale variability of the line-of-sight electron content resulting from the ionosphere and plasmasphere. The total electron content (TEC) maps, together with other indexes derived from TEC, are used to estimate the locations and time where larger signal delays in GNSS receivers might produce higher positioning errors.

Several TEC disturbances studies have been conducted in recent years [32, 34, 68, 86, 87, 88, 89, 90, 91]. However, they have mainly focused on TEC and in the northern hemisphere. Nevertheless, some studies of TEC have been conducted with a special focus on the South Atlantic Magnetic Anomaly area [92, 93, 94, 95, 96, 97, 98, 99, 100]. Besides

these works and some other exceptions (e.g., [101]), there is a lack of studies in the southern hemisphere. In addition, all the above-mentioned works did not study the effect of TEC on positioning error.

Although the position estimation of a GNSS receiver depends on TEC, for several reasons (location, correction algorithms, etc.), perturbations on TEC are not reflected in a simple manner over the position accuracy. Therefore, it is relevant to study the actual performance of the positioning estimation of GNSS receivers during geomagnetic storms. To evaluate the position error during geomagnetic storms, the precise point positioning (PPP) method is used. PPP is a method that performs efficient computation to determine high-quality coordinates. It uses a single receiver processing strategy for GNSS [24, 102]. PPP does not require any additional data from a reference station and can provide a solution from a centimeter to a decimeter level of positional accuracy both in static and kinematic modes [24, 103]. For these reasons, PPP has become the predominant positioning technique [24]. Many free PPP online services are available, such as the Automatic Precise Positioning Service (APPS) of the Global Differential GPS (GDGPS) System (`https://apps.gdgps.net/`, accessed on 6 December 2021), the GNSS Analysis and Positioning Software (GAPS-PPP) (`http://gaps.gge.unb.ca/`, accessed on 6 December 2021), the magicGNSS solution (magicGNSS) (`https://magicgnss.gmv.com/`, accessed on 6 December 2021), and the Precise Point Positioning of Canadian Spatial Reference System (CSRS-PPP) (`https://webapp.geod.nrcan.gc.ca/geod/tools-outils/ppp.php`, accessed on 6 December 2021) [104, 105, 106]. The CSRS-PPP service is one of the most used PPP online services in the field, and we use this service in this work to obtain the PPP estimation.

More recent studies have presented TEC disturbances produced by geomagnetic storms including GNSS position errors (PPP). These latest studies of geomagnetic storms and errors in GNSS positioning have focused on storms of the Solar Cycle 24. A summary of these studies can be found in Table 2.1.

Table 2.1: Example studies related to the impact of geomagnetic storms of Solar Cycle 24 (SC-24) on kinematic GNSS positioning.

Geomagnetic Storm	**Dst [nT]**	**Kp**	**AE [nT]**	**Stations N°**	**Kinematic PPP**	**Method**
7 January 2015 [107]	−99	6^+	2031	3	GIPSY-OASIS	ROTI
17 March 2015 [108]	−223	8^-	2298	∼ 500	GPS PPP Model	ROTI
17 March 2015 [109]	−223	8^-	2298	15	gLAB software	DVTEC, TIDs
22, 23 June 2015 [110]	−204	8^+	2698	5172	GAMP software	Spread-F, S4
20 December 2015 [108]	−155	7^-	1946	∼ 500	GPS PPP Model	ROTI
27 March 2017 [108]	−74	6^+	1505	∼ 500	GPS PPP Model	ROTI
8 September 2017 [111]	−124	8^+	2677	∼ 700	RTKLIB package	ROTI

Table 2.1 shows that there are not many studies related to the impact over the GNSS positioning accuracy of moderate geomagnetic storms. In a recent study, it was shown that the storm of 5 August 2019, which can be categorized as moderate (Dst peak = −53 nT, Kp = 5^+, AE∼1000 nT), had strong effects on TEC [112]. However, this work did not study the positioning accuracy of GNSS stations. The only study of the positioning error that considers a moderate geomagnetic storm was presented by Luo et al. [108] (see Table 2.1). Luo et al.

analyzed three geomagnetic storms in Solar Cycle 24. For the analysis, they used March 17th 2017 as a reference day for all the analyzed storms, which is a quiet day (Kp = 1^+). This work neither analyzes the conditions on the previous/posterior days for each storm nor removes the noise sources, such as other geophysical events (earthquakes) or interference from other radio emissions. In addition, in this work, the root means square (RMS) statistics per component (North, East, and Up) were obtained per latitude (high-, mid-, and low-). Thus, the reported 3D RMS was calculated with the components that combine different stations located at a similar latitude range.

In this work, we present the positioning error analysis of the 12 May 2021 geomagnetic storm (Dst peak = −61 nT, Kp = 7, AE∼1500 nT), which can be classified as moderate in terms of Dst but strong in terms of Kp. Although the study is at a global scale, unlike previous studies, we focus on the southern sector of America due to the large number of GNSS stations now available in this part of Latin America. We studied the spatial and temporal dependence of the higher errors estimated in the GNSS receivers for this storm. We also studied the time needed for some geodesic-quality GNSS stations to reduce the positioning error thanks to the algorithms that detect and correct the effects of TEC disturbances. By using three stations, one close to Madrid (Spain) and the other two in Chile (one close to Santiago and a second one 400 km south of it), we studied the effects on the positioning accuracy for two other moderate storms (27 March 2017 and 5 August 2019) to verify the methodology used in the 12 May 2021 study.

2.2 Materials and Methods

In this section, we describe the used data and processing procedure. The proposed procedure also includes analyzing the geophysical and geomagnetic conditions close to 12 May 2021.

2.2.1 Estimation of the Ionospheric Total Electron Content

The slant TEC (STEC) and vertical TEC (VTEC) data were obtained from GNSS measurements based on dual-frequency signals f_1 and f_2. Then, STEC and VTEC were calculated using the program GPS-TEC from receiver independent exchange format (RINEX) files [113] (`http://seemala.blogspot.com/`, accessed on 6 December 2021). In this work, VTEC values corresponding to satellite cut-off elevation angle 30^o at 350 km altitude were selected to minimize possible errors. The temporal VTEC estimates were released every 30 s. The TEC values were corrected from the satellite and receiver bias using the data obtained from AIUB Data Center of Bern University in Switzerland (`ftp://ftp.aiub.unibe.ch/CODE/`, accessed on 6 December 2021).

The RINEX files were obtained from 868 GNSS stations (Figure 2.1), taked from: the International GNSS service (IGS) stations; the Chilean network of GNSS receivers operated by the National Seismological Center at University of Chile (CSN in Spanish); the Argentine Continuous Satellite Monitoring Network (RAMSAC in Spanish) [114]; the Brazilian Network for Continuous Monitoring of the Institute of Brazilian Geography and Statistics (IGBE in Portuguese); and the Crustal Dynamics Data Information System (CDDIS) of the National Aeronautics and Space Administration (NASA); University NAVSTAR Consortium (UNAVCO); the Geoscience Australia; and the African Geodetic Reference Frame (AFREF).

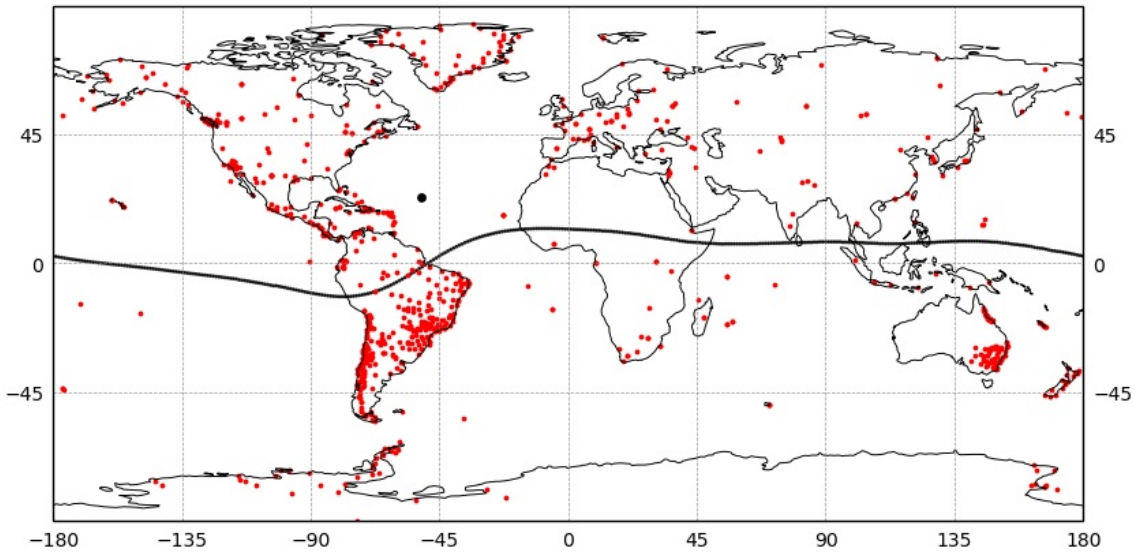

Figure 2.1: 868 GNSS receivers (red dots) used in present work. The Sun at 14.50 UT (black dot) on 12 May 2021, and the magnetic equator (black line).

In addition, the differential of VTEC (DVTE) in TECu and the percentage changes in VTEC (%DVTEC) were studied. These parameters are used in the analysis of ionospheric disturbances, defined as the relative variation of VTEC, epoch by epoch, with respect to the mean value (in time) of $\overline{VTEC}$ as shown in Equations (2.1) and (2.2) [58].

$$DVTEC_t = VTEC_t - \overline{VTEC_t} \tag{2.1}$$

$$\%DVTEC_t = \frac{DVTEC_t}{\overline{VTEC_t}} \cdot 100 \tag{2.2}$$

where t represents the epoch and $\overline{VTEC}$ is calculated by averaging the values of VTEC for the reference DoYs 129, 130, and 131.

Ionospheric TEC Maps

We used the ordinary Kriging interpolation technique [115] to map the estimation of the VTEC at each ionospheric pierce point (IPP). We selected this interpolation technique to fill in the data gap of the global ionosphere TEC map and the inhomogeneous sparsity of GNSS receivers [116, 117, 118]. We performed the ordinary Kriging interpolation in Python with the package Kriging. The documentation for the package can be found in `https://github.com/ERSSLE/ordinary_kriging` (accessed on 6 December 2021).

2.2.2 ROT and ROTI

Rate of change of the TEC Index (ROTI) is defined as the standard deviation of the rate of TEC (ROT). It is used in the detection and investigation of occurrences of ionospheric irregularities. ROTI was estimated by dual-frequency GNSS data with the time interval of 5 min by using Equation (2.3) [119, 120, 121, 122, 123]:

$$ROTI = \sqrt{\langle ROT^2 \rangle - \langle ROT \rangle^2} \tag{2.3}$$

where $\langle \cdot \rangle$ represents the temporal average. The ROT and ROTI values are typically expressed in units of TECu/min. ROT is defined as the TEC variation rate of two successive epochs as stated in Equation (2.4) [119, 120, 121, 122]:

$$ROT = \frac{STEC_t^{\mathrm{i}} - STEC_{t-1}^{\mathrm{i}}}{k_t - k_{t-1}} \tag{2.4}$$

where k, t, and i represent the GPS time, the epoch, and the number of observation satellites, respectively.

According to Liu et al. [124], the ROTI value can be divided into three groups: weak, if $0.25 \leqslant \mathrm{ROTI} < 0.5$; moderate, if $0.5 \leqslant \mathrm{ROTI} < 1$; and strong, if $\mathrm{ROTI} \geqslant 1$.

2.2.3 Apparent Position Variation Using Precise Point Positioning

The RINEX files of 868 GNSS stations were processed in the postprocessing kinematic precise point positioning with ambiguity resolution (PPP-AR) mode in the Precise Point Positioning of Canadian Spatial Reference System (CSRS-PPP) online service (`https://webapp.geod.nrcan.gc.ca/geod/tools-outils/ppp.php`, accessed on 6 December 2021) [104]. The CSRS-PPP provides centimeter-level estimations with converged float solutions [104, 105, 106, 164]. The CSRS-PPP returns to the user a processing report via email.

Usually, the report provides a different reference value for different days. We process the data to have an equal reference for all the used data to facilitate the evaluation of the position-variation time series. At each of the 868 stations, we also apply the common noise filter to correct the time series of the North, East, and Up components (Equation (2.5)). Then, we estimate the 3D resultant.

$$CAPdoy_t = APdoy_t - RP_t \tag{2.5}$$

where t is the epoch, CAPdoy_t is the corrected apparent position, APdoy_t is the apparent uncorrected position, and RP_t is the reference position. We use $\overline{AP}$ from reference DoYs 129, 130, and 131 to calculate RP_t.

At each of the 868 stations, the maximum error was calculated for eight days and with time windows of 15 min. Subsequently, the percentage of stations in East, North, Up, and 3D position errors intervals was calculated.

2.2.4 Geophysical and Geomagnetic Conditions

The geomagnetic data were downloaded from the World Data Center (WDC) for Geomagnetism, Kyoto (`http://wdc.kugi.kyoto-u.ac.jp/wdc/Sec3.htm`, accessed on 6 December 2021) [125]; OMNIWeb Plus Data Documentation (`https://omniweb.gsfc.nasa.gov/form/dx1.html`, accessed on 6 December 2021); and GFZ Helmholtz Centre Potsdam (`https://www.gfz-potsdam.de/en/kp-index/`, accessed on 6 December 2021) [126].

On 12 May 2021 (DoY 132), a moderate geomagnetic storm (G3) took place with a Kp-index $\geqslant 4$ from 6 UT. The maximum Kp-index of 7 was sustained between 12 and 15 UT. The Kp-index went below 3 after the 18 UT.

The geomagnetic storm started on the DoY 132. Its initial phase started at ∼6 UT and lasted ∼6 h. During this period, the Dst-index slowly decreased. The main phase of the storm started at ∼12.4 UT and lasted for ∼one hour. In the storm main phase, the Dst-peak of −61 nT was reached at 14 UT. At that time, the geomagnetic storm recovery phase began. The Dst-index went over −30 nT at ∼23 UT on the DoY 132 (see Figure 2.2b). We were unable to obtain the raw data of the AE-index, but it is possible to observe the behavior of this index in the graphical display of the data on the website of the WDC for Geomagnetism, Kyoto (http://wdc.kugi.kyoto-u.ac.jp/ae_realtime/202105/index_20210512.html, accessed on 6 December 2021). In that image, it is possible to see an intensification of the AE-index with two peaks ∼1500 nT between 12 and 16 UT.

The IMF Bz was below −10 nT between 12 and 15 UT on the day of the storm (DoY 132). The minimum Bz of −18.3 nT was reached at 13 UT. According to the Gonzalez and Tsurutani criteria [57], this event can be classified as a geomagnetic storm since it was caused by an interplanetary magnetic field Bz ≤ −10 nT that lasted more than 3 h (see Figure 2.2c).

The geomagnetic conditions were generally quiet between 9 and 11 of May 2021 (DoYs 129 and 131), where the Dst-index was predominantly positive, and the maximum Kp-index was 2 (see Figure 2.2a).

2.2.5 Possible Earthquakes Perturbations

We reviewed the occurrence of earthquakes (EQs) around the world with moment magnitudes over 5 Mw and depth less than 70 km between the 9 and 17 of May 2021 (DoYs 129 to 137). The data were obtained from https://earthquake.usgs.gov/earthquakes/search/ (accessed on 6 December 2021). Five strong EQs (6–6.9 Mw) and twenty moderate EQs (5–5.9 Mw) occurred in this analyzed period. However, none of them produced noticeable effects on TEC during the geomagnetic storm period. The differential TEC was analyzed, taking care of the potential minor effects in the other days of the analyzed period.

2.3 Results

In this section, we present the main results obtained after applying the methodology described in the previous section to the 868 stations.

First, we isolated the period of time to analyze. We focused the study between 9 May and 17 May 2021 (DoY 129 to 137). Figure 2.2 presents an example of the signals analyzed for this work. We calculated VTEC, DVTEC, %DVTEC, and ROTI as described in the previous section. These variables can be seen in panels (g–j) of Figure 2.2, respectively, for a sample station, the Vegas de Itata station (known as VITA station) located in Chile (36.42°S, 72.86°W). Then, by using the VTEC and the PPP-AR method (see Section 2.2.3), we were able to obtain the apparent position variation. In panels (d) to (f) in Figure 2.2, we present the root mean square (RMS) time series of the apparent position, after correcting using the common noise filter (see Equation (2.5)), per each component (East, North, and Up) also for the VITA station. It is clear in the image that the period of the storm is the period with the larger uncertainties in the position estimation.

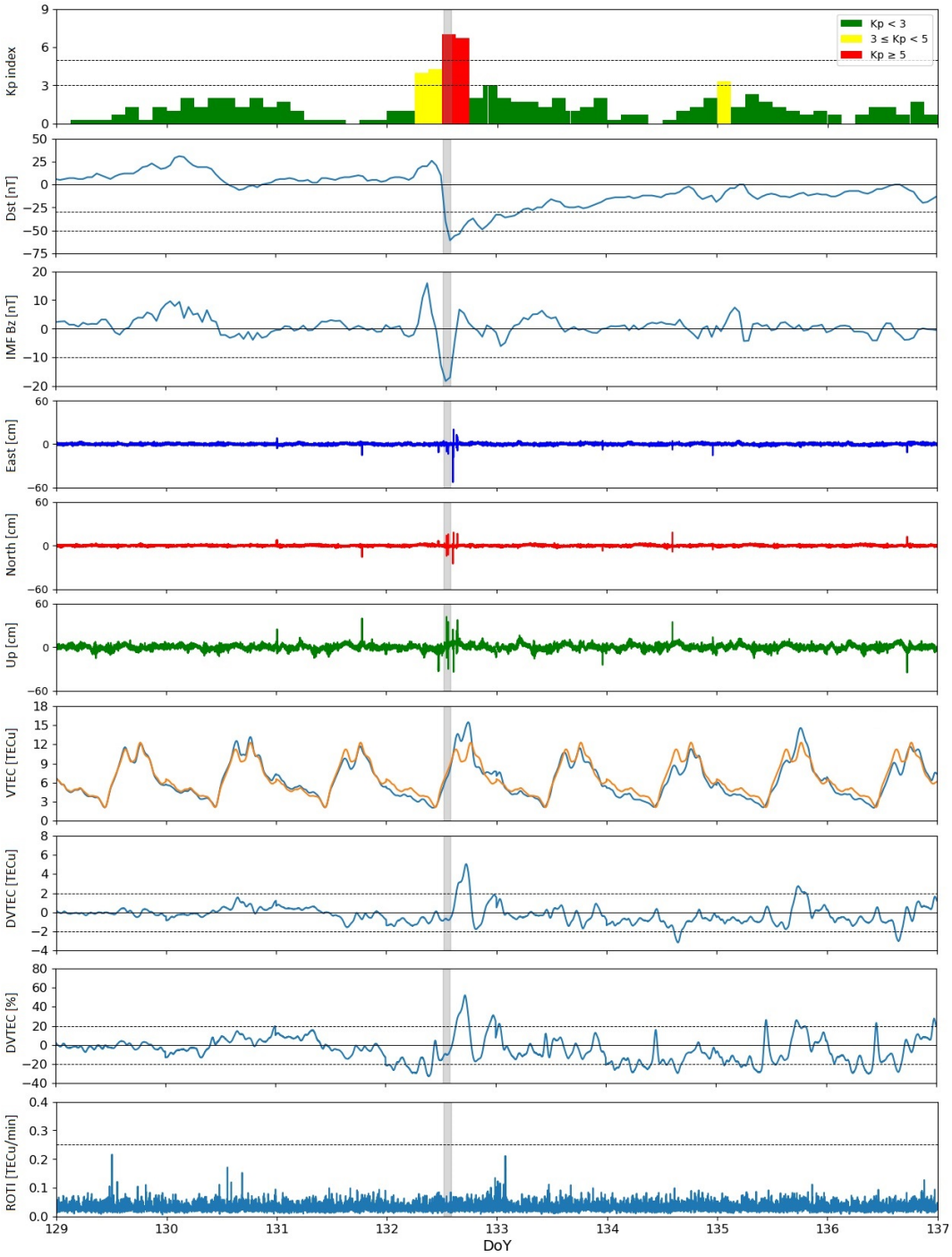

Figure 2.2: Panels (**a**) (Kp-index), (**b**) (Dst-index), and (**c**) (Z component of interplanetary magnetic field, IMF Bz) show the different indexes that characterize the geomagnetic conditions. Panels (**g**–**j**) present the different TEC variations related indexes (VTEC, DVTEC, %DVTEC, and ROTI). The panels (**d**–**f**) display the positioning error of each component in the VITA station, Vegas de Itata, Chile (36.42° S, 72.86° W). The orange line represents $\overline{VTEC}$ calculated with the reference days (DoYs 129, 130, and 131). (**g**) We represent the $\overline{VTEC}$ in all the studied DoYs to compare it with the VTEC of each of the days (blue line).

From each station data, we can estimate the VTEC over each station during the period of the geomagnetic storm (14.50–14.75 UT) on 12 May 2021 as shown in Figure 2.3a. By using the ordinary Kriging interpolation, as described in Section 2.2.1, it is possible to obtain filled-in VTEC maps for the geomagnetic storm day (Figure 2.3c) and for the averaged VTEC ($\overline{VTEC}$). $\overline{VTEC}$ is calculated with the VTEC of the previous days to the geomagnetic storm, DoYs 129, 130, and 131 (Figure 2.3b). Figures 2.3d,e show the differential VTEC (DVTEC) and perceptual DVTEC (%DVTEC) for the time of the geomagnetic storm, respectively, which are obtained by using Equations (2.1) and (2.2) with the data presented in (Figure 2.3b,c). From these figures, it is possible to notice that the South American sector is one of the most affected in terms of VTEC enhancement.

Since this study focuses on the positioning accuracy of the stations during a moderated storm, we estimate the PPP-AR as described in Section (2.2.3). Figure 2.4 (left panel) and Figure 2.5 (left panel) show different 3D positioning error maps for various times, obtained using the CSRS-PPP service. The reports provided by CSRS had different reference values for each of the eight days requested. This provoked that more than 5% of the stations had baselines with differences over 100 cm, such as: lovj (67.89° N, 34.62° E), novm (55.03° N, 82.91° E), ieng (45.02° N, 7.64° E), mdvj (56.02° N, 37.21° E), meco (−29.18° S, −58.08° W), csom (−52.78° S, −69.22° W) stations. Therefore, we processed the data to have an equal reference for all stations to facilitate the evaluation of the position variation time series.

After calculating the apparent position variation for each station in the time period of the geomagnetic storm (DoY 132, 14.50–14.75 UT), we quantified the number of stations around the world that had errors that fell in certain intervals (<5 cm, [5–10] cm, [10–20] cm, [20–40] cm, [40–60] cm, [60–100] cm and >100 cm). It is important to highlight that the PPP-AR procedure includes the use of a common noise filter (see Equation (2.5)). Without the filter, we had periods of time where certain GNSS stations consistently had very high errors even during quiet days. The results of the classification of the stations by their positioning errors is presented in Table 2.2. Each column on the table represents the percentage of stations with errors in a certain interval per each positioning component as well as the combination of these components in the 3D parameter. Each component uses two contiguous columns in Table 2.2, one with the percentages obtained for the average of the previous quiet days (e.g., North) and another with the percentage measured during the day and period of the geomagnetic storm (e.g., North gs). In this table, the percentage of the stations per interval for East, North, Up, and 3D position errors were obtained using the data from the total 868 GNSS stations around the globe we had available.

In Table 2.2, we present a snapshot of the errors focused on the geomagnetic storm time. Nevertheless, we also present a temporal evolution of the percentage of the stations with positioning errors over a certain threshold per component for the total of the available stations around the world in Figure 2.6. From this figure, it is possible to notice that the main errors are concentrated over the mid-day of the DoY 132, which is the geomagnetic storm period.

It is possible to notice from the TEC (e.g Figure 2.3) and the derived PPP-AR (Figures 2.4 (left panel) and 2.5 (left panel)) data that there is a region where the errors are more severe during the geomagnetic storm (DoY 132, 14.50–14.75 UT). This region is South America. In South America are located 325 stations of the 868 total available GNSS stations (∼37%). In Table 2.3, we present similar results compared to in Table 2.2 but with the 325 stations of this region. However, there is no other localized area in which we can detect strong variations. The other perturbed stations are distributed around the world. For this reason, we concentrated this study in the South American sector.

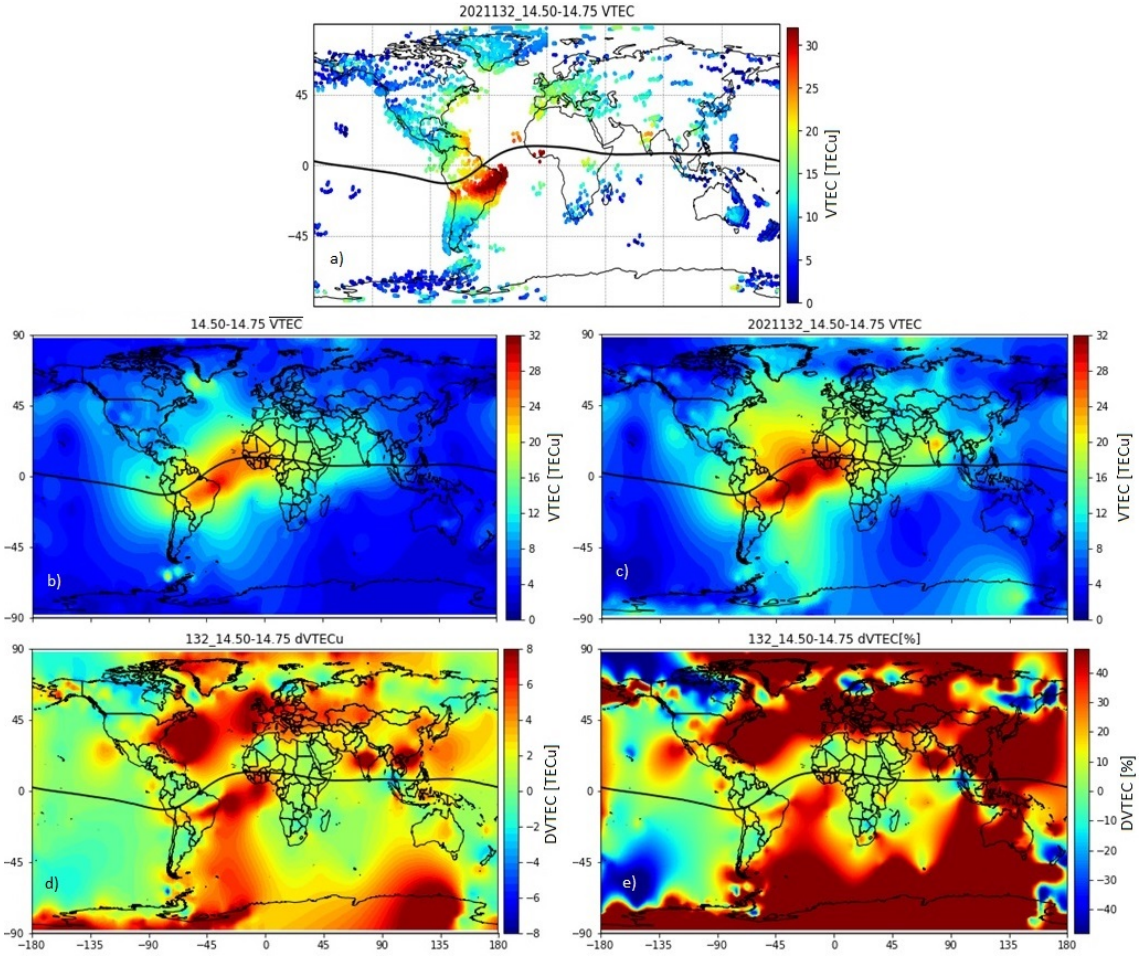

Figure 2.3: Ionospheric TEC maps using the Kriging interpolation method during the maximum apparent variation of position (between 14.50 and 14.75 UT). (**a**) VTEC at each IPP on the geomagnetic storm day. (**b**) $\overline{VTEC}$ is obtained by averaging the VTEC values of DoYs 129, 130, and 131, for 2021. (**c**) VTEC of geomagnetic storm day. (**d**) DVTEC is VTEC of geomagnetic storm day minus $\overline{VTEC}$. (**e**) The percentage changes in VTEC, %DVTEC.

The ROT index (ROTI) was calculated as described in Section 2.2.2 to study the relation of the variation of TEC in the positioning error for the 12 May 2021 geomagnetic storm. The images in the Figure 2.4 (right panel) show six maps of ROTI presenting the stations that had ROTI over 0.25 TECu/min. Each map represents a day at the same time of the geomagnetic storm, DoYs 129, 130, 131, 133, and 134 at 14.50–14.75 UT.

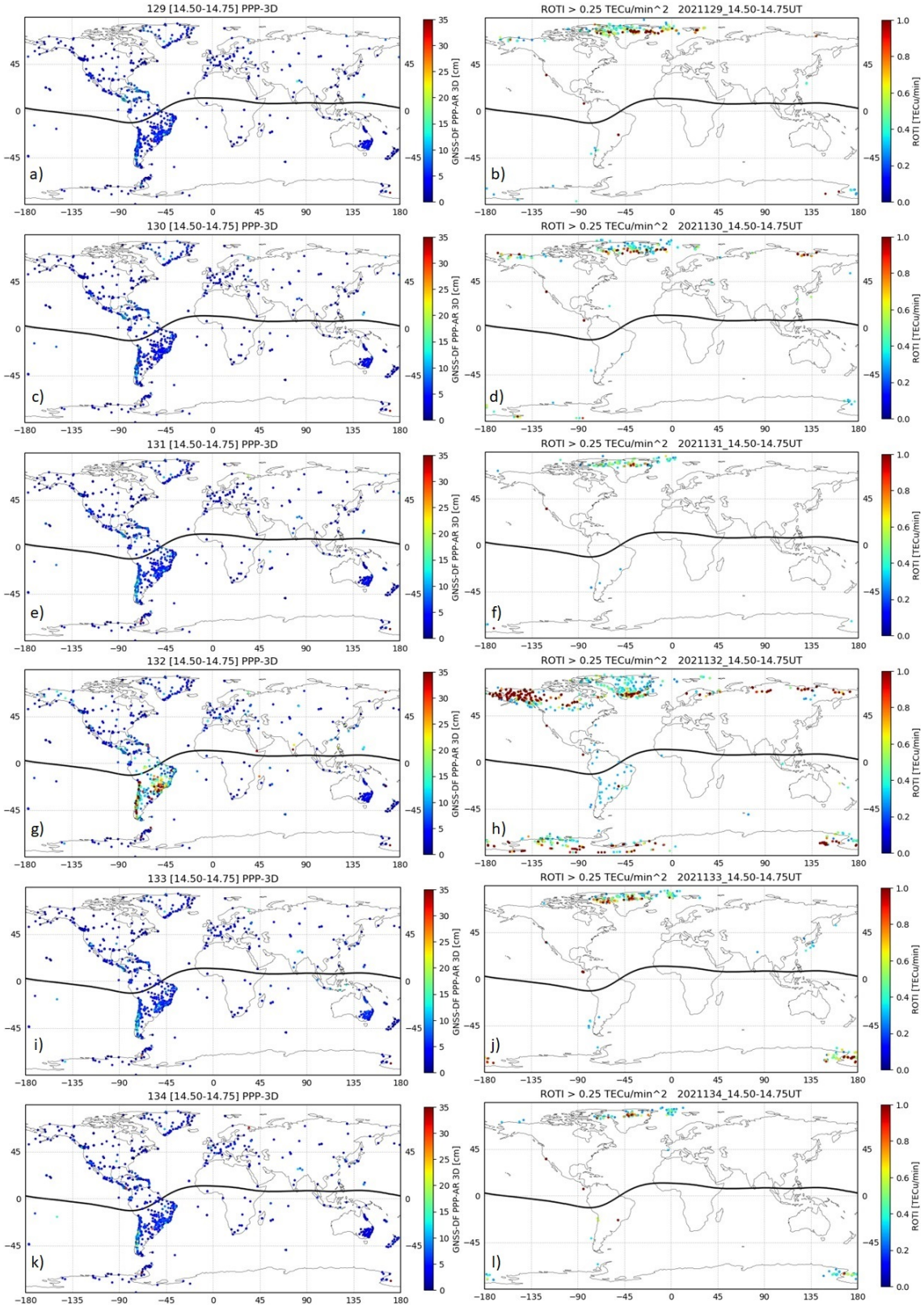

Figure 2.4: 3D position errors (**left panels**), and ROTI $\geqslant$0.25 TECu/min (**right panels**) on (**a**,**b**) DoY 129; (**c**,**d**) DoY 130; (**e**,**f**) DoY 131; (**g**,**h**) DoY 132; (**i**,**j**) DoY 133; and (**k**,**l**) DoY 134 (between 14.50 and 14.75 UT).

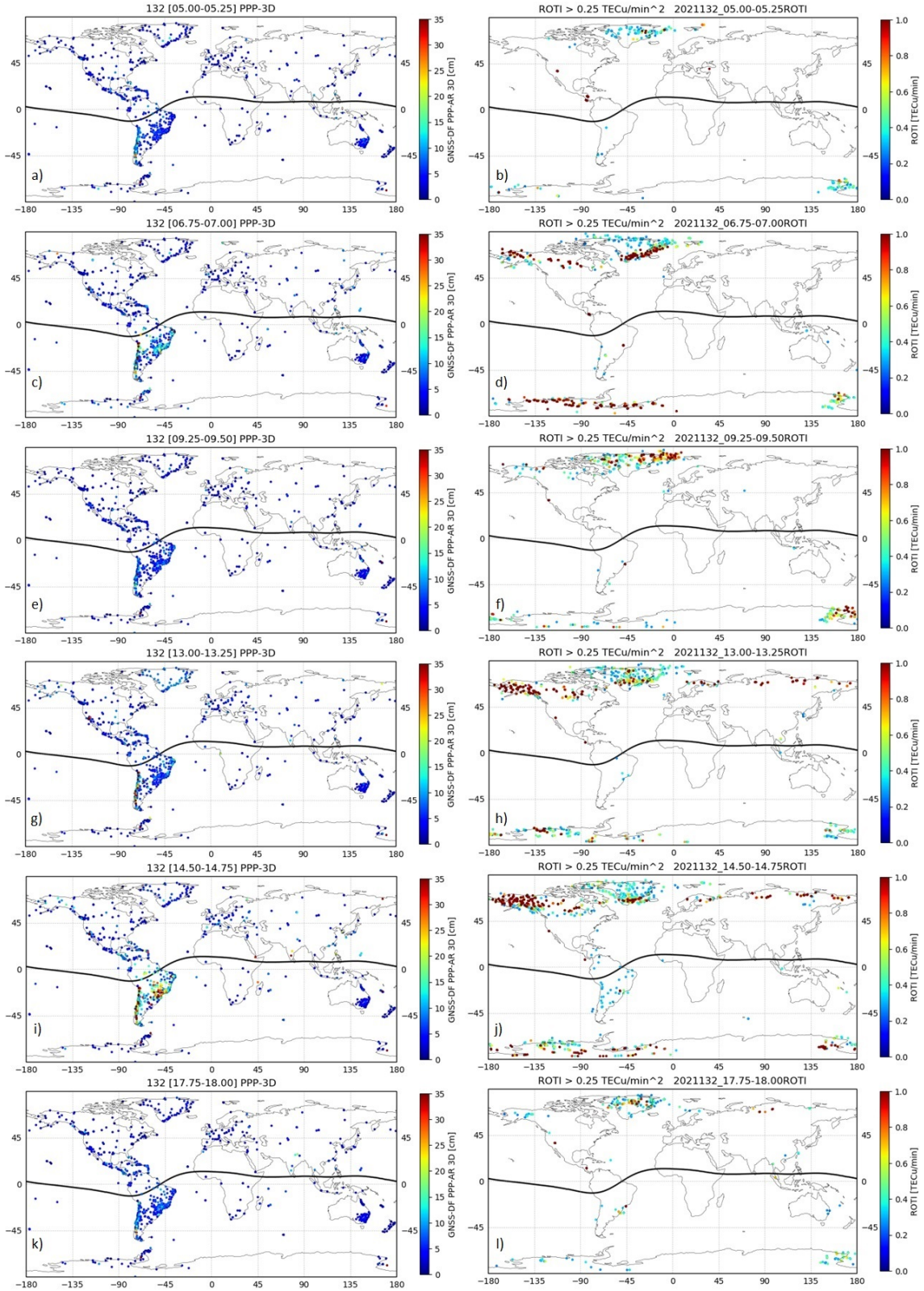

Figure 2.5: 3D position errors (**left panels**); and ROTI ⩾0.25 TECu/min on DoY 132 (**right panels**). (**a**,**b**) [5.00–5.25] UT; (**c**,**d**) [6.75–7.00] UT; (**e**,**f**) [9.25–9.50] UT; (**g**,**h**) [13.00–13.25] UT; (**i**,**j**) [14.50–14.75] UT; and (**k**,**l**) [17.75–18.00] UT.

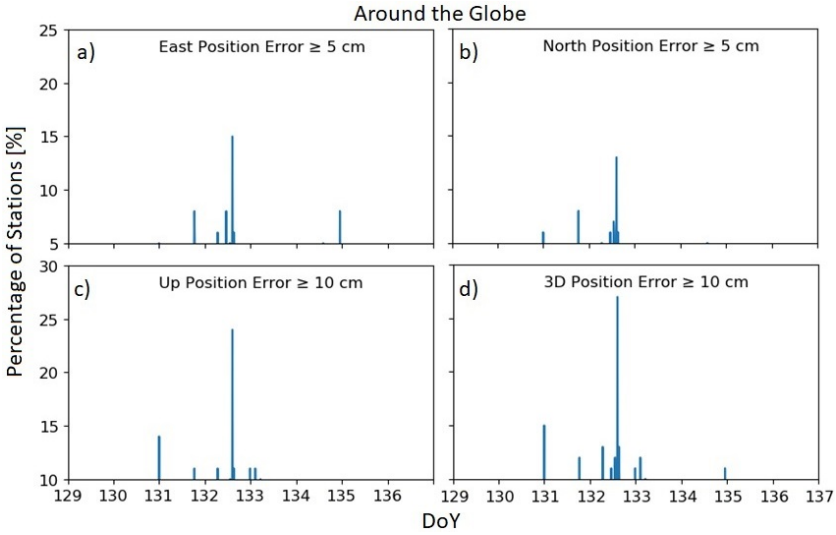

Figure 2.6: Time variations of percentage of stations around the globe (**a**) East Position Error $\geqslant$ 5 cm. (**b**) North Position Error $\geqslant$ 5 cm. (**c**) Up Position Error $\geqslant$ 10 cm. (**d**) 3D Position Error $\geqslant$ 10 cm.

Table 2.2: Percentage of 868 stations around the globe with East, North, Up, and 3D position errors using the common noise filter.

Error Intervals [cm]	**East [%]**	**East gs [%]**	**North [%]**	**North gs [%]**	**Up [%]**	**Up gs [%]**	**3D [%]**	**3D gs [%]**
<5	98	85	99	87	73	52	71	48
5–10	2	8	1	8	24	23	26	25
10–20	0	5	0	2	3	16	3	17
20–40	0	1	0	2	0	6	0	7
40–60	0	1	0	1	0	1	0	1
60–100	0	0	0	0	0	1	0	1
>100	0	0	0	0	0	1	0	1

Table 2.3: Percentage of 325 stations in South America with East, North, Up, and 3D position errors using the common noise filter.

Error Intervals [cm]	**East [%]**	**East gs [%]**	**North [%]**	**North gs [%]**	**Up [%]**	**Up gs [%]**	**3D [%]**	**3D gs [%]**
<5	98	70	98	72	55	13	50	9
5–10	2	16	2	19	39	33	43	32
10–20	0	11	0	6	5	35	6	38
20–40	0	2	0	2	1	15	1	15
40–60	0	1	0	1	0	1	0	2
60–100	0	0	0	0	0	2	0	2
>100	0	0	0	0	0	1	0	2

We also compared the results obtained for the 12 May 2021 geomagnetic storm with the effects on the positioning error obtained for other recent moderated geomagnetic storms, 27 March 2017 and 5 August 2019. The comparison was performed by using three particular stations: one station close to Madrid (MADR, 40.43° N, 4.25° W) and two located in Chile (South America). One of the Chilean stations is located in Las Vizcachas (VZCH, 33.6° S, 70.51° W) nearby to Santiago, and the second one is located in Vegas de Itata (36.42° S, 72.86° W), 400 km south of Santiago. The selection of the stations is based on the results of previous studies of the storms of March 2017 and August 2019 [108, 112]. The August 2019 geomagnetic storm [112] was a moderate one that produced a extreme positive ionospheric storm with strong TEC disturbances over Europe. However, this work did not study positioning errors. Thus, we selected a station in Europe to be compared with the two Chilean stations, which are located in South America and in the area of interest for this work. In addition, the stations in Chile are both required since each of them was operative for different storms (see Table 2.4). Luo et al. [108] studied the position error produced by the moderated geomagnetic storm of March 2017 but in broad latitudinal ranges, calculating the maximum positioning errors per component for each of these ranges but not per station. Figure 2.7 presents the time series of TEC related indexes and the position per component for the Madrid and Vizcachas stations. The left series of images show the data for the 5 August 2019 storm. The right series of images show the data for 12 May 2021. Table 2.4 summarized the positioning variations at each of the three stations produced by three different geomagnetic storms.

2.4 Discussion and Main Conclusions

In this section, we discuss the main findings regarding the geomagnetic storm of 12 May 2021. The main goal is to study the positioning errors of GNSS receivers caused by this storm, which can be classified as a moderate one. In addition, in order to verify our methodology and our findings we used previous equivalent geomagnetic storms as comparison. The comparison storms were the 27 March 2017 [112] and the 5 August 2019 [108].

2.4.1 12 May 2021 Geomagnetic Storm

The geomagnetic storm under study occurred in 12 May 2021. It can be classified as moderated in terms of Dst and strong in terms of Kp (Dst = −61 nT, Kp = 7, and AE =∼1500 nT). This storm is the first strong storm, in terms of Kp, of the solar cycle 25. The main phase of this storm lasted one hour from 13 UT to 14 UT, with the Dst peak at 14 UT (see Figure 2.2). Since the storm occurred in May the southern and northern hemispheres were in fall and spring seasons, respectively. During the main phase of the storm the Sun moved from the (18.27° N, 15.91° W) to the (18.28° N, 30.91° W) coordinates. This storm caused important effects on the GNSS stations in South America (see Figures 2.3 and 2.4g plot), which are rare for this type of storm.

Table 2.4: The root mean square (RMS), the maximum values (MAX), DVTEC, %DVTEC, and ROTI of the Madrid (MADR, 40.43° N, 4.25° W), Las Vizcachas (VZCH, 33.6° S, 70.51° W), Vegas de Itata (36.42° S, 72.86° W) stations, during the geomagnetic storms of 27 March 2017 (DoY 86), 5 August 2019 (DoY 217) and 12 May 2021 (DoY 132). DoYs 83, 84, 85 are the quiet DoYs of reference for the 27 March 2017 storm (QD-2017), DoYs 214, 215, and 216 are the quiet DoYs of reference for the August 2019 storm (QD-2019), and DoYs 129, 130, and 131 are the quiet DoYs of reference for the storm of May 2021 (QD-2021).

Station	**DoYs**	**RMS [cm]**				**MAX [cm]**				**DVTEC**	**%DVTEC**	**ROTI**
	[Season]	**E**	**N**	**U**	**3D**	**E**	**N**	**U**	**3D**	**[TECu]**	**[%]**	**[$\frac{TECu}{min}$]**
MADR	QD2017	0.4	0.5	1.0	1.1	1.6	2.0	5.5	5.7			
	DoY 86	0.6	0.5	1.2	1.4	2.2	1.5	4.4	4.5	9.9	110	0.1
	[Spring]											
	QD2019	0.6	0.5	1.5	1.7	2.7	2.2	6.2	6.3			
	DoY 217	1.0	0.9	2.8	2.8	3.1	2.6	11.6	11.7	12.0	153	0.52
	[Summer]											
	QD2021	0.7	0.6	1.7	1.9	2.4	2.7	8.7	8.8			
	DoY 132	1.2	1.1	3.5	3.7	3.9	4.1	15.4	17.0	11.9	120	0.3
	[Spring]											
VZCH	QD2017											
	DoY 86											
	[Fall]											
	QD2019	0.6	0.5	1.5	1.7	5.2	3.7	15.4	15.4			
	DoY 217	0.9	0.7	2.2	2.5	6.0	3.5	15.0	15.1	4.1	62	0.11
	[Winter]											
	QD2021	0.6	0.5	1.6	1.8	7.0	6.8	18.7	18.9			
	DoY 132	1.5	1.4	3.8	4.4	52.4	52.9	58.8	82.5	5.3	56	0.08
	[Fall]											
VITA	QD2017	0.6	0.6	1.8	2.0	2.9	3.1	8.4	8.4			
	DoY 86	1.0	1.1	2.8	3.2	3.5	3.0	10.0	10.0	23.5	150	0.09
	[Fall]											
	QD2019											
	DoY 217											
	[Winter]											
	QD2021	0.6	0.6	1.7	1.9	11.1	11.6	26.8	30.3			
	DoY 132	1.7	1.2	4.3	4.8	52.5	25.0	41.9	61.2	5.1	51	0.13
	[Fall]											

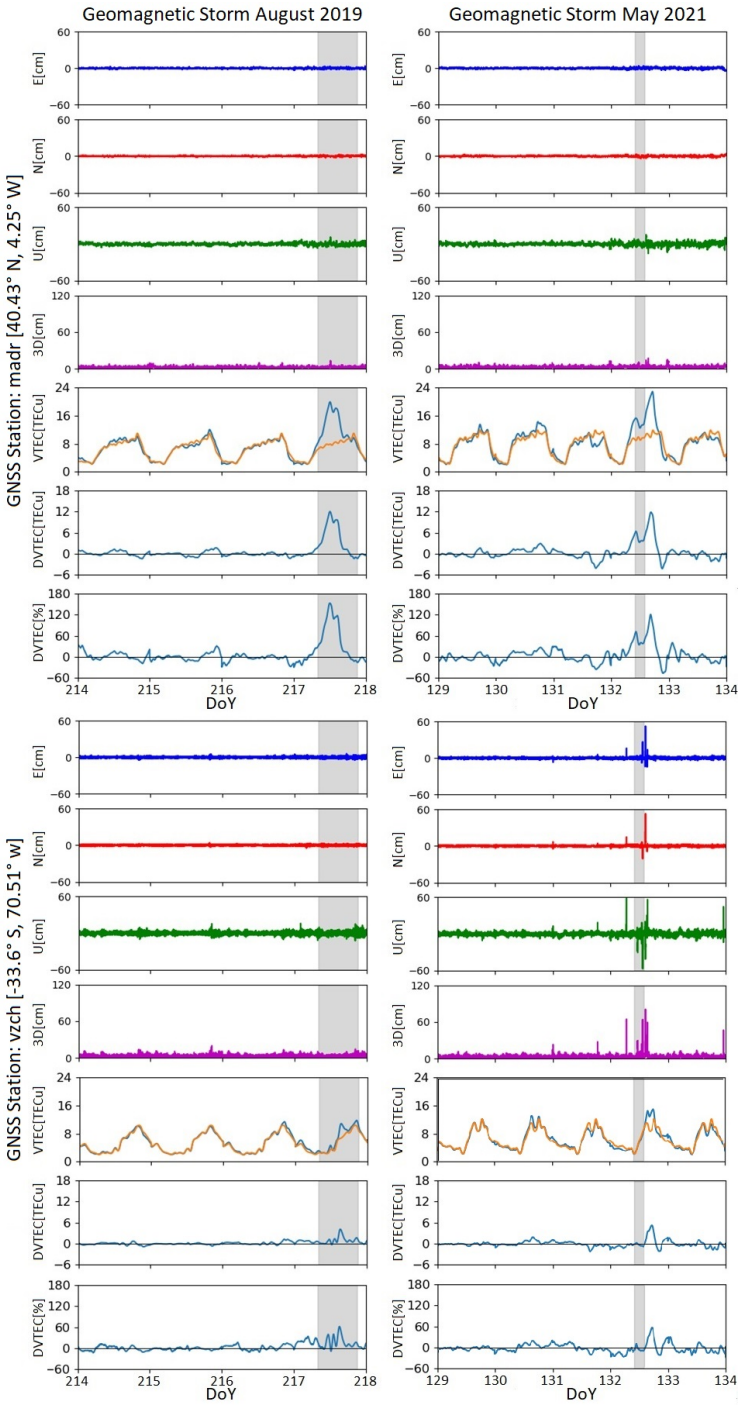

Figure 2.7: The positioning errors of each component and the different TEC variations-related indexes (VTEC, DVTEC, and %DVTEC). The (**left panels**) show the effects of the 5 August 2019 storm. The (**right panels**) show the effects of the 12 May 2021 storm. The (**top panels**) and (**bottom panels**) present the Madrid (MADR, 40.43° N, 4.25° W) and Las Vizcachas (VZCH, 33.6° S, 70.51° W) stations, respectively. On displays representing VTEC, the orange line represents VTEC mean calculated with the reference days. We plotted the VTEC mean in all the studied days to compare it with the VTEC of each of the days (blue line).

2.4.2 The 27 March 2017 and 5 August 2019 Geomagnetic Storms

In Table 2.1, we present previous works where the positioning errors were studied. In this table, we can see two moderate geomagnetic storms in terms of the Dst and Kp classifications, the 7 January 2015 (Dst = −99 nT, Kp = 6) and 27 March (Dst = −74 nT, Kp = 6). The 2015 geomagnetic storm, unlike the 12 May 2021 storm, took place during the solar maximum period of the solar cycle 24. In addition, the January 2015 storm occurred during the summer season in the southern hemisphere. The 27 March storm occurred during the descent period of the solar cycle 24. Then, it had similar solar activity compared to the May 2021 storm. Moreover, the March 2017 storm, like the May 2021 storm, was on the fall season in the southern hemisphere, with the Sun moving from the (2.69°N, 91.35°W) to the (2.83°N,43.68°W) coordinates. For these reasons. we discarded the 7 January 2015 storm as a good comparison storm and selected 27 March 2017 as a good one. The main phase of the March 2017 geomagnetic storm was much longer than that of the May 2021 storm (6–15 UT).

On the other hand, a recent study presented the case of a moderated geomagnetic storm occurring on 5 August 2019 (Dst peak = −53 nT, Kp = 5^+, AE ∼1000 nT) which produced a strong positive (decrease in electrons) ionospheric storm [112]. Although this geomagnetic storm was less intense than the May 2021 storm, its main phase was much longer (8-21 UT). During this storm, the southern hemisphere was in winter, then, like in May 2021, the Sun was over the northern hemisphere (from (17.01° N, 61.52° E) to (16.86°N,133.50° W)). Thus, we used this storm as a comparison to the May 2021 storm. Unfortunately, the study of this storm did not analyze the positioning error caused by it. The study showed that the European sector was one of the most affected in terms of TEC variations. For this reason, the comparison was performed including a GNSS located in Europe (close to Madrid, Spain). The other two stations located in Chile were used, since that region was one of the most perturbed areas in terms of position during the May 2021 storm (see Figure 2.4g plot).

2.4.3 Ionospheric Effects

From Figure 2.3, we can see that the VTEC is perturbed around the globe, including the southern part of America during the main phase of the May 2021 geomagnetic storm. On the other hand, in Figure 2.4h, we can see an increment in ROTI, that starts at the polar regions, propagating later the increment toward the equator, agreeing with previous studies [127, 128] (see Figure 2.5). In Figure 2.7, it is possible to see the VTEC and DVTEC disturbances of the GNSS stations over Madrid, Spain and Santiago, Chile (Vizcacha station) for the May 2021 storm. In comparison, we also present the VTEC and DVTEC disturbances on the same stations produced by the August 2019 storm. It is noticeable that TEC variations are similar between storms for the same station. In addition, the difference in the variations between the stations in southern and northern hemispheres is evident. The TEC variation seems stronger in the northern station. In Table 2.4, we can see that the VTEC is in percentage much higher over Madrid (Spain) than over Santiago (Chile) and Vega de Itata (Chile) for most of the storms, except for the March 2017 storm. We also calculated the ROT index for the May 2021 storm period. Five stations localized in high latitudes had values of maximum ROTI peak between 3.4 and 3.9 TECu/min, and average ROTI peak ∼1.1 TECu/min, and these values are similar to those presented by Kotulak et al. [127] for moderate geomagnetic storms.

2.4.4 Positioning Errors

The manner in which we quantified the positioning errors in this work was through the statistics of perturbed stations around the world and in particular in the South American sector. Our RMS position values for the quiet days are in accordance with the results presented by Katsigianni et al. [129]. They gathered that the performances of the kinematic postprocessed PPP-AR method are $\leqslant 0.8$ and $\leqslant 2$ cm for the horizontal components and the vertical component, respectively. Table 2.2 shows that for the quiet days, 71% of the stations had an error less than 5 cm in the 3D estimation. Table 2.2 also shows that for the May 2021 geomagnetic storm the main increment suffered by the Up component, passing from 27% of the total stations (868) with perturbations over 5 cm to 48%. Although the impact over the North and East components was less affected, they jumped from 1% to 13% and from 2% to 15%, respectively, for the stations with errors over 5 cm. Figure 2.6 graphically shows this increment in the number of stations over certain level of positioning error for a period of time that include the main phase of the May 2021 storm, also showing that the Up component is the most affected. The TEC (Figure 2.3) and ROTI (Figure 2.5h) plots show that for the May 2021 storm the main geophysical activity concentrated on the poles and on the South America sector. However, Figure 2.5g shows that the positioning errors were perceived mainly in stations in the South American sector. Table 2.3 shows that in the Up component, we went from 45% of the total station over South America (325) with an error over 5 cm to 87%. The similar increment can be perceived for the other components. In the North component, we passed from 2% to 28% of stations over an error of 5 cm. Similarly in the East component, the variation went from 2% to 30% for the same error range. Only 1% of the stations had errors over 40 cm in the North and East components during the May 2021 storm, while for the Up component with errors over 40 cm, the stations percentage reached 4%. Furthermore, the persistence of the position errors caused by the 12 May 2021 geomagnetic storm lasted for 9.25 h [6.50–15.75 UT] (Figure 2.2d–f; Figure 2.6; and Figure 2.7 right panels).

We compared the effects obtained over the positioning error due to the May 2021 storm, with the effects of the moderate geomagnetic storms that occurred on 27 March 2017 and 5 August 2019. Figure 2.7 compares the effects on the position in two different GNSS stations, one in Chile (South America sector) and one in Europe, where a previous storm produced strong ionospheric effects during the 5 August 2019 geomagnetic storm [70]. From the comparison, it is possible to notice that the perturbations in the position are much higher in the Vizcacha (Santiago, Chile) station and for the May 2021 storm. This is an intriguing result. Both storms, May 2021 and August 2019, are very similar, except for the duration of the main phases, but still, they produced very different effects on the position estimation (see Figure 2.7). Even more puzzling is the fact that the August 2019 storm has been reported to produce a strong ionospheric storm that affected the European sector [112]. For instance, the %DVTEC is almost double that in the Madrid station compared to the Santiago station (Vizcachas station), but we have found with our analysis on one station in the European sector that it did not impact the position estimation.

Table 2.4 presents the positioning error and %DVTEC data for the three selected for comparison stations (one in Europe and two in South America) during three moderate geomagnetic storms. It is possible to notice the same pattern as that obtained between the May

2021 and August 2019 storms which was obtained between the March 2017 and the May 2021 storms. Thus, the effects over the position estimation were very severe during the May 2021 storm over the South America sector (Vega de Itata, VITA station), even though the %DVTEC was much higher for the March 2017 storm both for Spain (Madrid) and Chile (VITA) stations.

ROTI also has an intriguing behavior. We observe an increase in the number of stations with ROTI $\geqslant$0.25 TECu/min (Figure 2.5) especially in the poles and the South American region. In North America and northern Europe region, the number of stations with activity increased from 50% to 94%. In the Antarctic region, there was an increase from 12% to 62% of stations with activity. In South America, the percentage passed from 1.5% to 10.5% of the stations with activity. Nevertheless, we do not find a significant increase in the number of stations with higher positioning errors over the poles. Therefore, it is conclusive that the fast variations of TEC might be responsible for the variations over the South American sector.

Our results did not confirm that positioning errors increased rapidly with increasing ROTI (Figure 2.2d–f,j; Figure 2.4g,h; Figure 2.5; Figure 2.7; and Table 2.4) as several studies suggest [107, 108, 109, 111]. Therefore, our results suggested that position errors also occur, regardless of whether the ROTI has rapid variations, if it is ROTI $<$ 0.25 TECu/min or no ROTI variations are appreciated.

In summary, the analyzed data show that the moderate 12 May 2021 geomagnetic storm strongly affected the GNSS precision for about an hour in several GNSS receivers, mainly on stations located in the South American sector. Comparison with previous moderate storms (27 March 2017 and 5 August 2019) showed that the effects in the position estimation are not directly deducible from the geomagnetic storms characteristics. The three analyzed storms were moderated, although the 12 May 2021 storm had a higher Kp, which tends to be a good indicator of midlatitude activity. By using three stations we compare the effects of the three storms, showing that the effects are stronger on the South American sector even though the ionospheric effects (DVTEC) are not severe.

The positioning error data show that the horizontal coordinates are more robust to TEC disturbances, although the error in the vertical component is still high. In the literature, the vertical coordinate tends to be neglected, but for current and future GNSS applications, it might be relevant. It could be important for autonomous aerial applications or for high-precision activities. The mining, agriculture, fishing, and disaster-control sectors in Chile are starting to adopt autonomous or tele-operated systems that might be sensitive to ionospheric disturbances. The relevant height of the vehicles in these industries might impose a serious risk for infrastructure or people if the vertical error in the GNSS receiver skyrockets. For instance, for open-pit mines, a high vertical error may cause a failure in the estimation of the terrace in which a vehicle is with the consequent risk of falling. Potential risks could be reduced by stopping autonomous operations during these events. However, our results show that it is hard to predict when a storm will have serious effects over the position accuracy. False positives in the forecasting can be complex for these industries, since stopping operation even for a short time, such as an hour, could be prohibitively expensive. The new solar cycle is critical to unravel the relation between solar activity and positioning errors in the GNSS receivers thanks to the large number of GNSS stations available around the world,

gathering relevant data. However, we need to process the data in a standardized manner that facilitates comparison between different cycles, paying attention to the storms that produce unexpected behaviors such as those in the 12 May 2021 geomagnetic storm.

Chapter 3

Ionospheric Behavior During the 10 June 2021 Annular Solar Eclipse and Its Impact on GNSS Precise Point Positioning

The main effects of the 10 June 2021 annular solar eclipse on GNSS position estimation accuracy are presented. The analysis is based on TEC measurements made by 2337 GNSS stations around the world. TEC perturbations were obtained by comparing results 2 days prior to and after the day of the event. For the analysis, global TEC maps were created using ordinary Kriging interpolation. From TEC changes, the apparent position variation was obtained using the post-processing kinematic precise point positioning with ambiguity resolution (PPP-AR) mode. We validated the TEC measurements by contrasting them with data from the Swarm-A satellite and four digiosondes in Central/South America. The TEC maps show a noticeable TEC depletion ($<-60\%$) under the Moon's shadow. Important variations of TEC were also observed in both crests of the Equatorial Ionization Anomaly (EIA) region over the Caribbean and South America. The effects on GNSS precision were perceived not only close to the area of the eclipse but also as far as the west coast of South America (Chile) and North America (California). The number of stations with positioning errors of over 10 cm almost doubled during the event in these regions. The effects were sustained longer ($\sim$10 h) than usually assumed.

Keywords: solar eclipse; ionosphere; precise point positioning; GNSS; total electron content; rate of total electron content index; Swarm satellite measurements; ionosonde; electron density

3.1 Introduction

A solar eclipse is a natural phenomenon that occurs when the Moon moves in the way between the Sun and Earth, totally or partially blocking the Sun, casting a shadow over the Earth. Since the Sun is one of the major drivers of atmospheric effects, such as its ionization at

high altitudes, its blocking produces several disturbances. The atmospheric effects of a solar eclipse have been the subject of extensive research, mainly in meteorological parameters, total column ozone, photochemistry, gravity waves, and ionospheric parameters [130]. Despite the large number of studies concerning eclipses, the event of a solar eclipse is still unique since it happens at different seasons, different times of the day, different locations, and under different synoptic and geomagnetic conditions [130, 131, 132]. In addition, with every new eclipse, the scientific community gains larger numbers and a variety of instruments, which allow us to revisit the proposed conclusions from previous eclipses.

The ionosphere is directly affected since this atmospheric layer is produced by solar radiation. The total electron content (TEC) is a measure of the electron density in the ionosphere integrated along the line of sight, thus, an indication of its ionization. TEC can be obtained using a radio link between a satellite and the ground. Nowadays, the most common system delivering TEC measurements is the Global Navigation Satellite Systems (GNSS), which requires TEC measurements to improve the precision of position estimation. TEC is expressed in TEC units (TECu), where 1 TECu = 10^{16} e/m^2. The perturbation of the ionosphere can be analyzed through the variations of TEC. The main parameters of the TEC variations during the eclipses are the delay value (τ) relative to the maximum phase of the eclipse; its amplitude (A), which generally is a decrease; and the duration (ΔT) of the perturbation [29]. Since the Moon's shadow moves rapidly from west to east across the Earth at supersonic speed, the total eclipse lasts just a few minutes anywhere [133, 134, 135]. Previous works have reported the depletion of TEC after the onset of the partial solar eclipse and have presented values of A in percent (A[%]) that can reach up to -64% with τ from -30 to 180 min [136, 137, 138, 139]. This delay has been interpreted as an indicator of the combined effect of the photochemical processes and plasma dynamics [130, 140]. Some works have reported ΔT from 50 to 240 min [29, 141]. However, some studies have reported even longer effects [142, 143]. A historical summary of ionospheric responses to solar eclipses since 1920 can be found in the Appendix in Bravo et al. [144].

Recent studies have shown that the effects of a solar eclipse on the ionosphere are not only local but can affect other geographic regions outside the umbra/penumbra of the eclipse [143, 145, 146, 147, 148]. These effects may be due to transport between hemispheric magnetic conjugates, alteration of the equatorial fountain effect, generation of a disturbed dynamo, and/or Atmospheric Gravity Waves (AGWs) that generate Traveling Atmospheric Disturbances (TADs) and/or Traveling Ionospheric Disturbances (TIDs).

An annular solar eclipse took place on 10 June 2021. The first external contact (P1 time) and the last external contact (P4 time) of the solar eclipse were at 08:12:22 UT and 13:11:22 UT, respectively. The partial solar eclipse was seen from the following geographic regions: in parts of the eastern United States and northern Alaska, Canada and parts of the Caribbean, Europe, Asia, and northern Africa. The annular eclipse was visible from parts of northeastern Canada, Greenland, and the Arctic Ocean, passing through the North Pole, and ending in Russian territory. It maximum magnitude was 0.944: this is the fraction of the angular diameter of a celestial body being eclipsed. This magnitude value was reached at geographic coordinates 80.815°N, and 66.78°W, at 10:41:57 UT (Greatest Eclipse time, GE time, `http://xjubier.free.fr/en/site_pages/solar_eclipses/ASE_2021_GoogleMapFull.html`, last accessed on 15 June 2022). The paths at ground level and at 350 km of altitude of the

annular eclipse are shown in Figure 3.1 (see Supplementary Materials, Video S1). Due to the specific geometry of each eclipse, the paths differ both geographically and temporally according to the height considered, which could be significant when analyzing them [149].

Solar eclipses are rare events and, particularly, the 10 June 2021 event is an excellent opportunity to study the eclipse-induced effects on the polar ionosphere. Since the ionospheric variations can perturb GNSS, the eclipse can be used to study the positioning errors in these regions. There are some studies on the effects of the ionosphere during solar eclipses over the northern polar region. One of the first reported ones was the total solar eclipse that occurred on 9 March 1997 over Kazakhstan, Mongolia, eastern Siberia, and the Arctic Ocean ($\tau = -26$ to 180 min and A $= -5$ TECu) [29, 150]. Another reported one is the total solar eclipse that occurred on 1 August 2008 over Canada, northern Greenland, the Arctic Ocean, central Russia, Mongolia, and China ($\tau = -27$ to 44 min, and A[%] $= -40$ to -11%) [138]. The most recent one is the eclipse that occurred on 20 March 2015 that covered the North Atlantic, Faroe Islands, and Svalbard (A[%] $= -50$ to -10%) [133, 151]. This last one happened during the recovery phase of the most intense geomagnetic storm during Solar Cycle 24, the so-called St. Patrick's Day Storm. Due to the limited availability of GNSS stations around the globe at the time of these previous studies, they were focused on a regional scale. The increasing number of accessible GNSS stations around the world allows a study on a global scale, facilitating the search of potential interactions between regions. This can show how spreadable GNSS disturbances are. In particular, the poles are of interest since several ionospheric disturbances can start from there during geomagnetic storms.

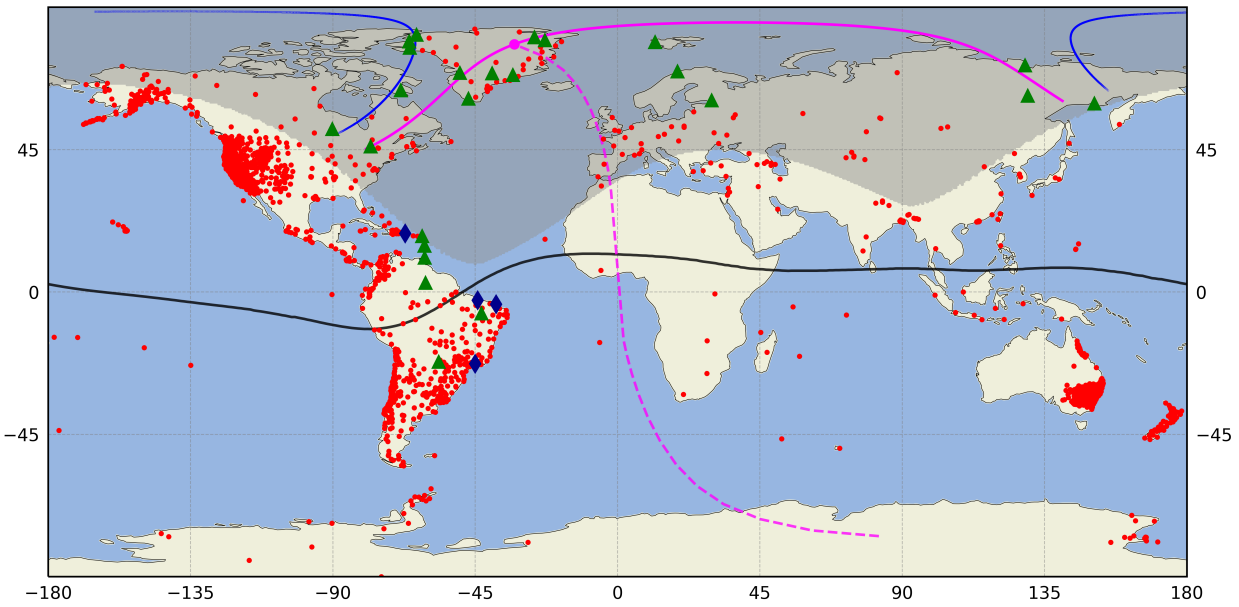

Figure 3.1: Instruments used in present work: 2337 GNSS stations (red dots), 4 digisondes (blue rhombuses), and 24 selected GNSS stations (green triangles). The magnetic equator (black line) and the annular eclipse path at ground level (blue line) are shown. Eclipse obscuration mask from P1–P4 time (shaded region), the annular solar eclipse path (magenta line), the maximum obscuration (magenta dot) at 350 km altitude are presented. The magenta dashed line starts from the maximum obscuration of the solar eclipse to its conjugate location in the Southern Hemisphere.

In GNSS receivers, TEC is estimated simultaneously from several satellites of the network, which serves to study the ionosphere. (e.g., [29, 113, 136], among many others). During the eclipses, the ionization decreases, producing a depletion in TEC. Although a decrease in electron concentration during a solar eclipse could produce an improvement in the positioning precision, it actually generates positional errors [152, 153]. Few authors have analyzed the GNSS positioning errors caused by the influence of solar eclipses. The eclipses that occurred over Croatia on 11 August 1999 [154], over China on 22 July 2009 [155], and over the United States on 21 August 2017 [153] are some of the studies that analyzed GNSS positioning errors.

For the 1999 solar eclipse, Filjar, et al. [154] used a single frequency receiver located in the north of Croatia with ∼95% of maximum percentage of obscuration (MPO). In this work the authors did not relate ionospheric disturbances with positioning variations. The authors collected the horizontal positioning at the eclipse's maximum obscuration time (MOT). They calculated an average positioning error of ∼34 m on horizontal Global Positioning System (GPS) accuracy for that time. These horizontal values could be due to the use of a single-frequency, the number of receiver channels, and the possible influence of Selective Availability (until May 2000).

Jia-Chun et al. [155] used eight GPS stations to study the TEC changes and their effect on the positioning during the 22 July 2009 solar eclipse. They possessed a real-time point positioning and real-time precision of single baselines. The measurements were affected by a geomagnetic storm (Dst peak = −80 nT and Kp-index = 5^+), which made it difficult to separate the influence of the eclipse from the storm one.

In the case of the 2017 eclipse, Park et al. [153] computed and compared the rate of change of the TEC (ROT) with respect to the day before and the day after the eclipse; and with a time window of 3 h, from 16 UT. They determined the means of positioning errors at four GNSS stations (localized in Oregon, United States) within the path of the total solar eclipse which reached ∼32 cm. However, on reference days, the means of positioning errors were between 7–14 cm. The authors used the average length of the eight baselines, which was ∼270 km. On the eclipse day, the means of positioning results were −4 to 324% over the day before and the day after the eclipse. Yuan et al. [152] established the ionospheric eclipse factor method (IEFM) to model the ionospheric delay searching for the improvement of the GNSS positioning estimation. In this contest, the paper introduces the concept of the ionospheric eclipse factor method for the IPP for relatively precise separation of daytime from nighttime for the ionosphere. Although the ionospheric eclipse factor is not related to a solar eclipse as an astronomical phenomenon that occurs when the Moon obscures the Sun from Earth, this method could be used in future studies related to the impact of solar eclipses on GNSS positioning.

In our case, we obtain the apparent position variation using the post-processing kinematic precise point positioning (PPP) with ambiguity resolution (PPP-AR) mode. We chose this method because PPP demonstrates a high ability to improve position estimation. PPP is used for calculating the coordinates of a single receiver without the need for a reference station nearby as a control station. In addition, we can find some free PPP services available online [33]. PPP-AR is an enhanced version of the PPP technique that resolves the carrier phase ambiguities, improving the PPP accuracy [33, 129, 156]. Katsigianni et al. [129]

recently presented a comparison between PPP and PPP-AR. In order to offer the community the possibility of evaluating our analysis, we used an online service. Thus, we selected the CSRS-PPP service for this work because it is one of the most commonly used PPP online services in the field. We also applied the common noise filter to more than 2300 GNSS stations, to correct the time series of the North, East, and Up components of the GNSS receivers, as described in [33].

The regular ionospheric effects of solar eclipses are not yet fully understood. Studies of the eclipse-induced effects on the ionosphere are important because they provide a better understanding of the processes that control the ionosphere and that can cause GNSS positioning errors. In the present paper, we present the impact of the 10 June 2021 annular solar eclipse on ionospheric variations that also cause errors in GNSS positioning. Therefore, we first analyze the ionospheric behavior at a global scale based on 2337 dual-frequency (DF) GNSS stations, Swarm-A satellite, and four ionospheric stations. We used GNSS stations distributed around the world since they will allow us to evaluate the effects beyond the northern polar region with a higher spatial resolution than ever before. Unlike previous studies about the GNSS positioning errors caused by the influence of solar eclipses, our study is focused on a global scale. This allowed us to find other locations in the world that could be affected by a perturbation in the north pole and how that perturbation propagates to those potential locations.

3.2 Materials and Methods

The methodology used in the 10 June 2021 annular eclipse is mainly based on the one described in Valdés-Abreu et al. [33]. However, in this work we incorporate the processing of ionospheric data from a Low Earth Orbit (LEO) satellite. The procedure of this work also includes the analysis of geophysical and geomagnetic conditions close to the date of the eclipse (10 June 2021). How we use this new set of data is detailed below.

3.2.1 Estimation of the Ionospheric Total Electron Content

The inherent space-time variability of the ionosphere can be observed through TEC that can be obtained using GNSS stations [157]. Then, GNSS measurements based on dual-frequency signals f_1 and f_2, were used to obtain the vertical TEC (VTEC) data. The ground-based dual-frequency GNSS (DF-GNSS) receiver continually records two types of delay: the pseudoranges and the carrier phases of the two signals. The obtained data was used to estimate the slant TEC (STEC) and to calculate the VTEC. STEC and VTEC were calculated from Receiver Independent Exchange Format (RINEX) files by using the GPS-TEC analysis software (GPS-TEC program Ver 2.9.5, developed by Dr. Gopi Seemala, `https://seemala.blogspot.com/2017/09/gps-tec-program-ver-295.html`, last accessed on 17 April 2022) [113]. VTEC values were estimated with a satellite cut-off elevation angle of 30° at an altitude of 350 km to reduce possible errors. The TEC values were released every 30 s and were corrected for the satellite and receiver bias using the data obtained from the AIUB Data Center of Bern University in Switzerland (`ftp://ftp.aiub.unibe.ch/CODE/`, last accessed on 17 January 2022).

For the final selection of the RINEX files of each GNSS station, we took into account several aspects. First, we considered the quality of the files during the selected period of days (DoYs 159–163). Second, we verified that there were no errors or data-gap after TEC estimation and post-processing PPP-AR. This aspect is critical to relating TEC and/or ROTI with positioning variations. We used data from all available stations in the polar regions. We also tried to cover regions such as Africa, Australia, and Asia. The International GNSS Service (IGS) stations (`http://www.igs.org`, last accessed on 17 January 2022) [158]; the Chilean network of GNSS receivers operated by the National Seismological Center at University of Chile (CSN in Spanish); University NAVSTAR Consortium (UNAVCO); the Argentine Continuous Satellite Monitoring Network (RAMSAC in Spanish) [159]; the Brazilian Network for Continuous Monitoring of the Institute of Brazilian Geography and Statistics (IBGE in Portuguese); the Geoscience Australia; the Low-Latitude Ionospheric Sensor Network (LISN, `http://lisn.igp.gob.pe/`, accessed on 26 July 2021); and the African Geodetic Reference Frame (AFREF) provided RINEX files of 2337 GNSS stations that met the requirements we imposed (see Figure 3.1).

Additionally, the differential VTEC (DVTEC) in TECu and the percentage changes of DVTEC (DVTEC[%]) were used. These parameters are studied in the analysis of ionospheric irregularities, defined as the relative variation of VTEC, epoch by epoch, with respect to the mean value (in time) of $\overline{VTEC}$ as shown in Equations (3.1) and (3.2) [58].

$$DVTEC_t = VTEC_t - \overline{VTEC_t} \tag{3.1}$$

$$DVTEC[\%]_t = \frac{DVTEC_t}{\overline{VTEC_t}} \cdot 100 \tag{3.2}$$

where t represents the epoch, and $\overline{VTEC_t}$ is calculated by averaging the values of VTEC at the same time of the day, t, for the reference DoYs 159, 160, 162 and 163 which correspond to 2 days before and 2 days after the day of the eclipse (DoY 161).

According to the methodology [33], we used the ordinary Kriging interpolation method to produce the TEC maps at each ionospheric pierce point (IPP). With this method, we filled in the spatial gaps of the global ionosphere TEC maps, minimizing the effects of the inhomogeneous distribution of GNSS receivers. Before interpolating, we selected a spatial resolution of $2.5° \times 2.5°$. Then, we employed the Kriging package implemented in Python (`https://github.com/ERSSLE/ordinary_kriging`, last accessed on 17 January 2022).

3.2.2 ROT and ROTI

In order to detect, investigate and characterize the occurrence of ionospheric irregularities, we have used the Rate of change of the TEC Index (ROTI). The ROT and ROTI values are usually expressed in TECu/min. ROTI is defined as the standard deviation of the rate of TEC (ROT), and it is estimated by dual-frequency GNSS data with the time interval of 5 min by using Equation (3.3) [33]:

$$ROTI = \sqrt{\langle ROT^2 \rangle - \langle ROT \rangle^2} \tag{3.3}$$

where $\langle\cdot\rangle$ represents the temporal average. ROT is defined as the TEC variation rate of two successive epochs as stated in Equation (3.4) [33]:

$$ROT = \frac{STEC_t^{\mathrm{i}} - STEC_{t-1}^{\mathrm{i}}}{k_t - k_{t-1}} \tag{3.4}$$

where i indicates the observed satellite and t denotes the time of epoch. Hence, $k_t - k_{t-1}$ is the time interval between the subsequent epochs.

Depending on the ROTI value, the activity level can be classified in ranges such as: weak (if $0.25 \leqslant \mathrm{ROTI} < 0.5$); moderate (if $0.5 \leqslant \mathrm{ROTI} < 1$); and strong (if $\mathrm{ROTI} \geqslant 1$), according to Liu et al. [124].

3.2.3 Low Earth Orbit Satellite Measurements and Ionospheric Data

Additionally, we analyze ionospheric measurements provided by a LEO satellite, the European Space Agency's Swarm mission. This mission is a constellation of three LEO satellites that were successfully launched on 22 November 2013, and are still operating. This constellation is designed to provide measurements of the Earth's magnetosphere and ionosphere, studying the impact of the solar wind on the dynamics of the upper atmosphere [160, 161]. The Swarm-Alpha (A), Bravo (B), and Charlie (C) are three identical satellites that share the same design and payloads.

All three satellites were put into a circular near-polar orbit with a low eccentricity. Swarm-A/C pair have the same orbit configuration (inclination of 87.35°, altitude of ∼450 km, east–west separation of about 1–1.5° in longitude), while Swarm-B has a different one (inclination of 87.75°, altitude of ∼510 km). These satellites fly above the F-layer peak (the peak altitude of the ionospheric electron density). In addition, Swarm-A/C fly in tandem, while Swarm-B moves away from the couple Swarm-A/C by covering different local times [160, 161].

The Swarm spacecraft were equipped with different payloads, including GPS receivers and Langmuir Probes (LP), among others. We considered the ionospheric VTEC values associated with the point where the link path between GPS and Swarm-A satellite pierces the spherical thin shell located 400 km above the Swarm-A orbit. We also used in-situ electron density (N_{e}) measurements by LP at ∼450 km [161, 162] for each of the five selected DoYs in June 2021 (`https://Earth.esa.int/web/guest/swarm/data-access`, last accessed on 17 January 2022).

We used the Swarm Level 2 (L2) TEC (TECxTMS_2F) data product, which contains time series of slant and vertical (absolute and relative) TEC for each GPS satellite in view (at most eight due to instrumentation design). The cadence of the ionospheric TEC data is 1 Hz since it was changed from 10 s (0.1 Hz) to 1 s (1 Hz) on 14 July 2014 [161, 163].

We also used the Swarm LP data, which is part of the EFI package (EFIX_LP_1B plasma data). LP provides measurements of in situ N_{e} and electron temperature with a 2 Hz sampling rate [161, 162].

3.2.4 Apparent Position Variation Using Kinematic Precise Point Positioning

The RINEX files of 2337 GNSS stations were processed using the Canadian Spatial Reference System (CSRS-PPP) online service of Natural Resources Canada's Canadian Geodetic Survey (https://webapp.geod.nrcan.gc.ca/geod/tools-outils/ppp.php, last accessed on 6 January 2022) [104] with ambiguity resolution (PPP-AR) mode. The CSRS-PPP provides centimeter-level estimations with converged float solutions [104, 105, 106, 164].

Usually, the CSRS-PPP report can provide a different reference start value for different days. To facilitate the evaluation of the apparent position variation time series, we process the data to have an equal reference for all the data used. At each of the 2337 stations, we applied the common noise filter to correct the time series of the North, East, and Up components, using the equation [33]:

$$CAPdoy_t = APdoy_t - RP_t \tag{3.5}$$

where t is the epoch, $CAPdoy_t$ is the corrected apparent position, $APdoy_t$ is the apparent uncorrected position, and RP_t is the reference position. We use the average of AP, $\overline{AP}$, from the same reference days mentioned in Equation (3.1) to calculate RP_t.

At each of the 2337 stations, the maximum error was obtained within the selected five days. Subsequently, the error of each station per component was classified by intervals, counting the percentage of the total number of stations that fell into each interval. In addition, a 3D position error was calculated as:

$$3D_t = \sqrt{East_t^2 + North_t^2 + Up_t^2} \tag{3.6}$$

We use two threshold values. First, we selected threshold values for maximum 3D positioning error greater than or equal to 10 cm (3D $\geqslant$ 10 cm) since according to data on quiet days, over 90% of the GNSS stations had 3D errors of less than 10 cm, while during ionospheric disturbances, only ∼40% kept this level of accuracy [33]. Second, we applied the Equation (3.6) to the horizontal and the vertical components presented in [33, 129], obtaining the threshold of the 3D positioning error root mean square (3D-RMS) greater than or equal to 3 cm (3D-RMS $\geqslant$ 3 cm).

3.2.5 Geomagnetic and Geophysical Conditions

The geomagnetic data downloaded from OMNIWeb Plus Data (https://omniweb.gsfc.nasa.gov, last accessed on 11 May 2022) for the 10 June 2021 annular solar eclipse indicates a period of low activity. Except in DoY 163, where it was 4^- between 3 and 6 UT, the estimated 3-hour planetary index (Kp) was $\leqslant 3^-$. The disturbance storm time index (Dst) peak was >-17 nT, except after DoY 162 where a minimum of -37 nT was reached at 11 UT. The interplanetary magnetic field (IMF) Bz component in GSM coordinate peak was >-7.4 nT after DoY 162 and the solar wind speed (Vsw) was 330–520 km/s during 8–13 June 2021 (see Figure 3.2).

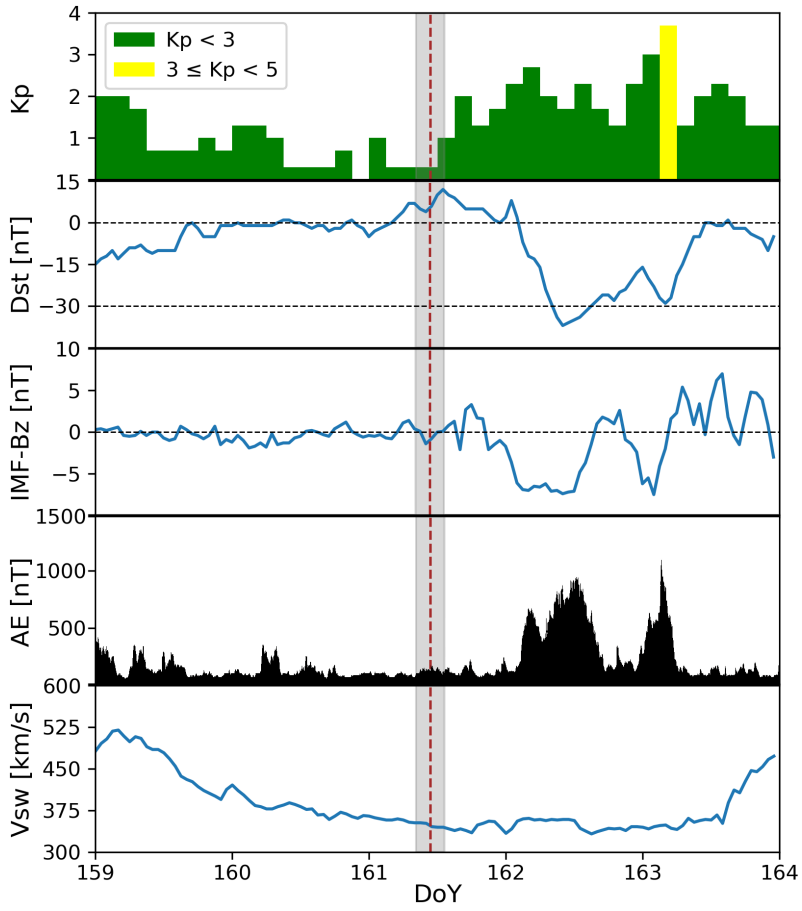

Figure 3.2: Variations of 3-hourly Kp, Dst, IMF-Bz, AE, and Vsw indices that characterize the geomagnetic conditions on 8–13 June 2021. P1–P4 time (light grey bar) and GE time (red dashed line) are also represented.

The Auroral Electrojet index (AE) is a good proxy of the geomagnetic activity level at mid/high latitudes [33, 62]. Following De Michelis et al. [165], we selected two distinct datasets corresponding, respectively, to geomagnetically quiet (AE $<$ 50 nT) and active (AE $>$ 300 nT) periods. Figure 3.2 also illustrates that the AE index was over 500 nT between 5 and 15 UT on DoY 162, and between 1 and 5 UT on DoY 163; so these time periods showed some activity in the auroral regions. Since these days are used by comparison with the day of the eclipse, these periods of time were treated with care to avoid interfering with the eclipse analysis.

Therefore, the geomagnetic conditions were generally quiet, except on DoY 162 where a weak geomagnetic storm took place between 8 and 16 UT. DoY 162 did not cause problems in the ionospheric TEC background to our results for the eclipse day. However, the geomagnetic activity the day after the eclipse had significant effects on GNSS positioning errors comparable to the positioning errors caused by the annular solar eclipse. These effects will be presented in more detail in the coming section.

Earthquake Occurrence

We also reviewed the occurrence of earthquakes (EQs) around the world, with a moment magnitude greater than 5 Mw and a depth of over 70 km on 8–13 June 2021. This review is important because EQs are sources of TEC disturbances and thus positioning errors. In the period analyzed, 15 moderate EQs of less than 5.7 Mw occurred (`https://earthquake.usgs.gov`, accessed on 17 January 2022). However, none of them produced noticeable effects on TEC or on the position estimation on the GNSS receivers during the analyzed period of days.

3.3 Results

In this section, we present the main results obtained after applying the methodology described in the previous section. The results obtained in this work can be divided into two main parts: (1) the analysis of the TEC maps that present the effects on the ionosphere at a global scale; and (2) the calculation of the positioning errors that these ionospheric effects generate.

3.3.1 Ionospheric Behavior and TEC Maps

From the data of each station, we can estimate the VTEC for each station during the selected period of days. By using the ordinary Kriging interpolation, as described in Section 3.2.1, it is possible to obtain VTEC maps. Figure 3.3 shows a summary of the TEC maps by contrasting the eclipse (VTECe) and control ($\overline{VTEC}$) days. We present some particular hours: 09.15 UT, 10.70 UT (GE time), 12.00 UT, 13.19 UT (P4 time), 13.72 UT (P4 time + ∼0.5 h), and 17.66 UT. Figure 3.3 also shows the eclipse masks from 20% obscuration and with intervals of 20%, at 350 km altitude (white line). From these figures, it is possible to notice that the Greenland and South American sectors are two of the most affected in terms of VTEC depletion. VTECe in IPP and DVTEC[TECu] in Figure 3.3 use the Kriging interpolation method and are shown in equidistant cylindrical projection and Northern Hemisphere polar plots (see Annex B, Figure B.1).

The 09.15 UT, 12.00 UT, and 13.72 UT maps were chosen in particular because they show the greatest apparent position variations during the eclipse time window. The 17.66 UT map was chosen because the ionosphere was roughly recovered by that time. For a better visualization of the eclipse effects, a third column has been incorporated where the VTEC differential in TEC units (DVTEC[TECu]) is shown.

DVTEC had values of around −20% (−2 TECu) over the oceanic sectors when the eclipse began (P1-time). However, at these locations, the GNSS receivers are scarce, which can cause less reliable interpolation. This value could be considered as part of the non-significant variations in DVTEC. A similar problem is identified over Central Africa, where there is a value of 50% (7 TECu), possibly also due to the few receivers in this area (see Figure 3.1). The anomalies in these areas were observed more than 5 h before the eclipse. We will focus mainly on changes generated over the continental areas of America and Europe, while the other areas will not be considered for this analysis.

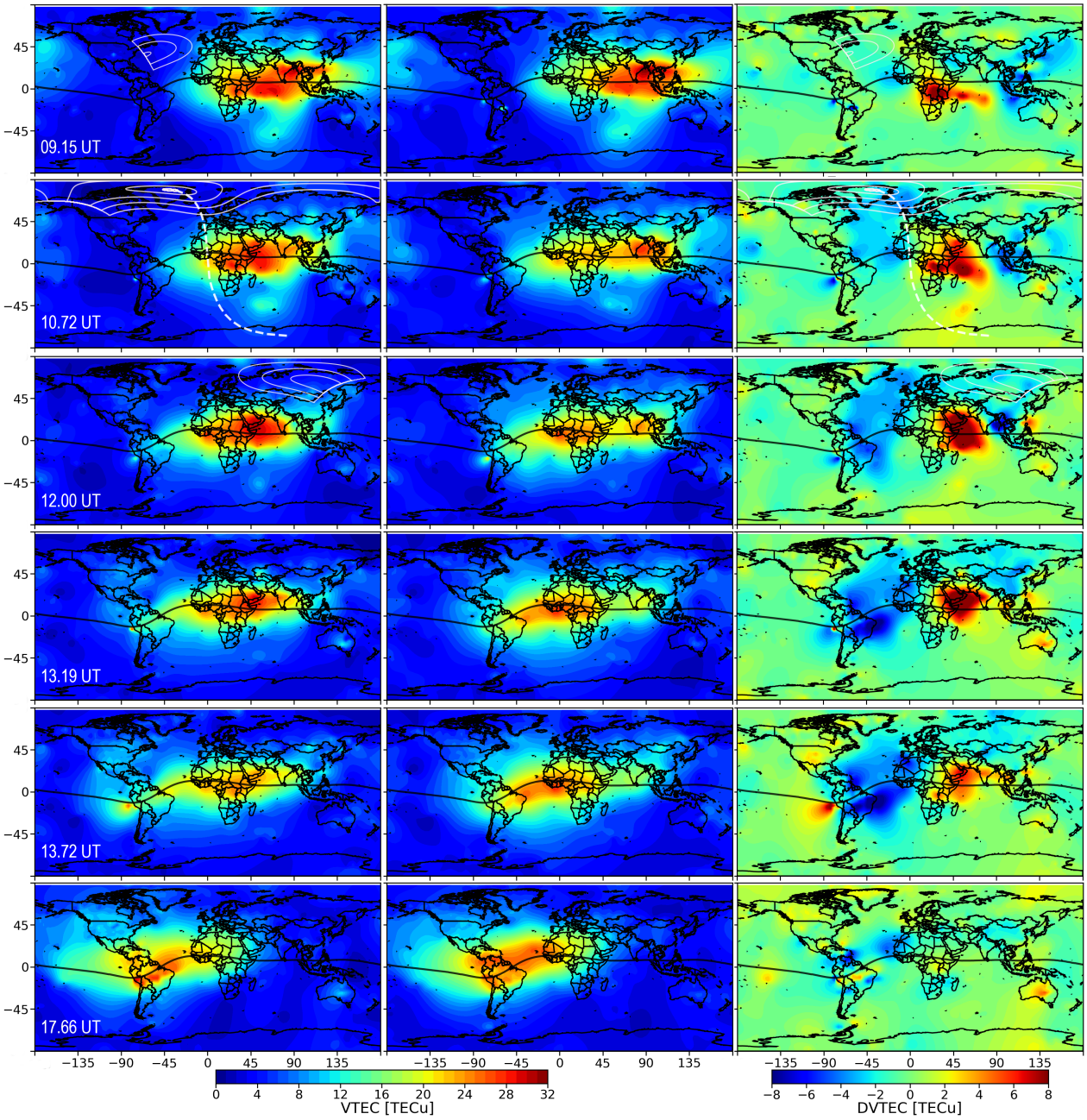

Figure 3.3: Ionospheric TEC maps during the 10 June 2021 Annular Solar eclipse using the Kriging interpolation method. From left to right panels: VTECe, $\overline{VTEC}$, and DVTEC[TECu]. From top to bottom panels: 09.15 UT, 10.70 UT (GE time), 12.00 UT, 13.19 UT (P4 time), 13.72 UT, and 17.66 UT. Eclipse obscuration masks from 20% obscuration and with intervals of 20%, at 350 km altitude (white line) are shown. The white dashed line starts from the maximum obscuration of the solar eclipse to its conjugate location in the Southern Hemisphere at 350 km altitude.

When the ionospheric TEC effects due to eclipse have already begun, the 09.15 UT maps show a slight depletion of −30% (−1 TECu) across eastern Canada under the shadow of the eclipse. At 10.70 UT (GE-time), these changes expand beyond the shadow area of the eclipse (see second row of Figure 3.3). The 10.70 UT maps show that ionospheric TEC depletion did

not only occur across the obscuration region over the Northern Hemisphere. DVTEC[%] had values of around −60% (−4 to −2.5 TECu) over the South and East coasts of Greenland, −50% (−3 TECu) eastern Canada, and around −50% (∼−3 TECu) over the Lesser Antilles.

The 12.00 UT, 13.19 UT, and 13.72 UT maps show DVTEC[%] had values of around −30% (−3 to −1.5 TECu) over Russia after GE time. Figure 3.3) also illustrates how the TEC disturbance moved from West to East over the Northern Hemisphere, following the path of the annular solar eclipse. At 12 UT, there is a recovery of the ionospheric TEC over Canada and Greenland regions, but DVTEC[%] had values of less than −50% in East coast of Greenland. Ionospheric TEC depletion had values of around −60% (∼−5 TECu) over the Lesser Antilles near the north crest of Equatorial Ionization Anomaly (EIA) and less than −30% (∼−5 TECu) appeared over South America near the south crest of EIA. The 13.19 UT and 13.72 UT maps show another slight recovery of the ionospheric TEC in the North Atlantic and Greenland, as well as a TEC depletion over Russia. Moreover, TEC depletion was accentuated in the EIA crests over South America, where DVTEC[%] had values of less than −60% (<−11 TECu). It is shown that the effects lasted beyond the end of the eclipse.

The 17.66 UT maps present the global recovery of the ionosphere a few hours after the end of the eclipse. These maps show a slight DTEC[%] enhancement in the center of the EIA form ∼−16% to ∼10%. But the TEC depletion was ∼−20% (−5 to −3 TECu) in the EIA crest over South America. The TEC behavior in the EIA crests was maintained until after 19.66 UT.

On the other hand, DoY 162 had geomagnetic activity (see Section 3.2.5). Therefore, we checked if the DVTEC changes that we observed for the day of the eclipse were due to using DoY 162 as one of the reference days. We compute a new $DVTEC_t$ ($DVTECnew_t$, Equation (3.1)), and a new $\overline{VTEC_t}$ by averaging the VTEC values at the same time of the day, t, for the reference days, DoYs 159, 160, and 163. For each map, we used the map algebra ($DVTEC_t - DVTECnew_t$). The mean value ranged between −0.5 and 0.1 TECu, with a standard deviation of less than 0.7 TECu (see Annex B, Figure B.2, Table B.1). Therefore, geomagnetic activity during the DoY 162 did not cause problems in the background to our ionospheric TEC results for the eclipse day.

Ionospheric Behavior Using Swarm Satellite Measurements

We also present ionospheric behavior using Swarm-A measurements (see Figure 3.4). We illustrate VTEC at 850 km altitude on DoY 161 compared to DoY 159 during three ascending passes of the Swarm-A satellite (⩾45°S, see Figure 3.4 (upper panels)). We selected the three Swarm-A satellite passes that best fit the eclipse region and eclipse time window. The first satellite pass (∼8.50–9.20 UT) occurred after P1 time. The greatest ionospheric TEC degradation was −30°S–30°N (∼−1.7 TECu, −35%). The second pass (∼10.10–10.80 UT) was close to the GE time. As latitude increases, TEC decrease. The third satellite pass (∼11.70–12.40 UT) was performed prior to P4 time (∼−1.9 TECu, −37%). It is possible to see that TEC decrement was concentrated between 10 and 30°N (VTEC was close to ∼−1 TECu, and ∼−30%). Ionospheric TEC depletion was greatest in the 15–75°N region (∼−2 TECu, −45%).

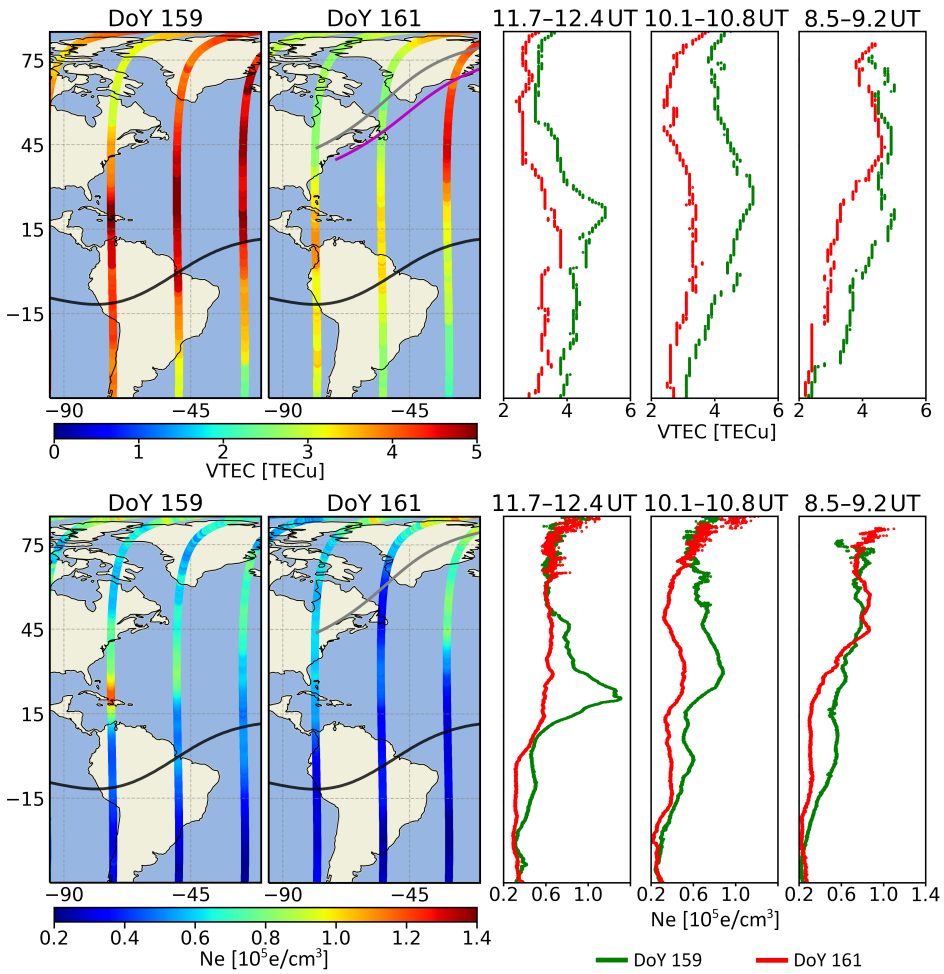

Figure 3.4: Ionospheric behavior using Swarm-A measurements. (**Upper panels**) present ionospheric TEC data were taken by Swarm-A satellite at 850 km (at 400 km above the Swarm-A). The TEC gathered through the satellite orbit is presented over an Earth map (left panel) and as a profile with data obtained in one of the comparison days (right panel). The three satellite passes are from 45°S to ∼90°N, from left to right, between ∼11.70–12.40, ∼10.10–10.80, and ∼8.50–9.20 UT during 2 days before eclipse day (DoY 159), and eclipse day (DoY 161). The annular eclipse path at 450 km (grey line) and 850 km altitude (magenta line) are also shown on DoY 161. VTEC on DoY 161 (red dots) compared to DoY 159 (green dots) between ∼11.70–12.40 UT, ∼10.10–10.80 UT, and ∼8.50–9.20 UT. (**Bottom panels**) depict Swarm-A in situ electron density (N_e) presented in the same way than the VTEC data.

Figure 3.4 (bottom panels) depict in situ N_e measurements made by Swarm-A Langmuir probe. Figure 3.4 (upper panels) show that VTEC behaves similarly to N_e. We observed that N_e decrease was −46% (-0.26×10^5 e/cm^3) at ∼8.86 UT in ∼1°N; −55% (-0.39×10^5 e/cm^3) at ∼10.62 UT in ∼50°N; and −55% (-0.72×10^5 e/cm^3) at ∼12.05 UT in ∼20°N.

3.3.2 ROTI and GNSS Precise Point Positioning Accuracy Maps

We estimated the ionospheric TEC, ROTI, and positioning for the full 5 days but only show 6 hours per day. On the eclipse day, we observe the largest positioning variations during this time window (around P1–P4 time, see Figure 3.5). This study focuses on the positioning accuracy of the stations during the 10 June 2021 annular solar eclipse, during the time between 8 and 14 UT. We estimated the PPP-AR using the CSRS-PPP service, as described in Section 3.2.4. Comparing the eclipse day with respect to the DoYs 159 and 160, we can see that the percentage of GNSS stations that exceeded maximum 3D positioning error $\geqslant$10 cm and 3D-RMS $\geqslant$3 cm (positioning thresholds) jumped from $\sim$180 ($\sim$8%) to 333 ($\sim$14%) and from $\sim$170 ($\sim$7%) to 210 ($\sim$9%), respectively. In addition, the ROTI threshold $\geqslant$0.25 TECu/min was taken according to Liu et al. [124], and used in the methodology [33]. Figure 3.6 shows maximum 3D positioning errors, 3D-RMS of the apparent position, and ROTI maps, for each of the five selected DoYs.

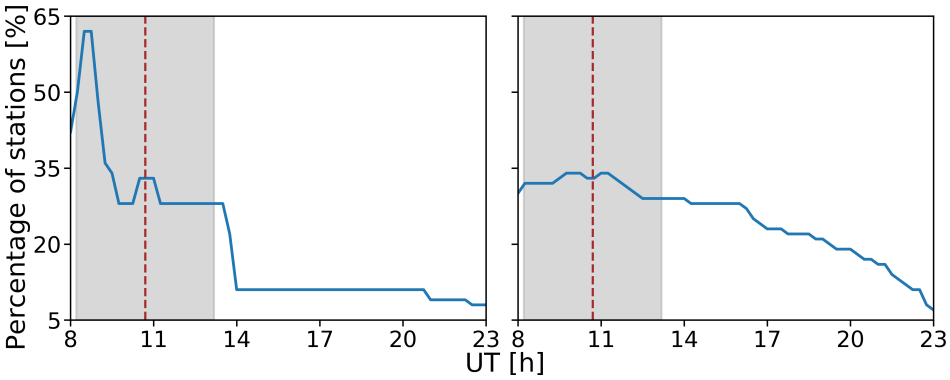

Figure 3.5: Time variations of the percentage of stations with 3D positioning error greater than 10 cm on DoY 161. The (**left panel**) shows the 36 GNSS stations localized in Greenland. The (**right panel**) presents the 335 GNSS stations that are situated in South America.

ROTI was calculated as described in Section 3.2.2 to study the relationship between the variation of TEC and the positioning error for the eclipse. The images in the Figure 3.6 (right panel) show five maps of ROTI, each representing the stations that had ROTI greater than 0.25 TECu/min. Each map represents a different day, but at the same time as that of the solar eclipse, DoYs 160–163 between 8 and 14 UT. We do not show the maps for DoY 159 because they are similar to those for DoY 160.

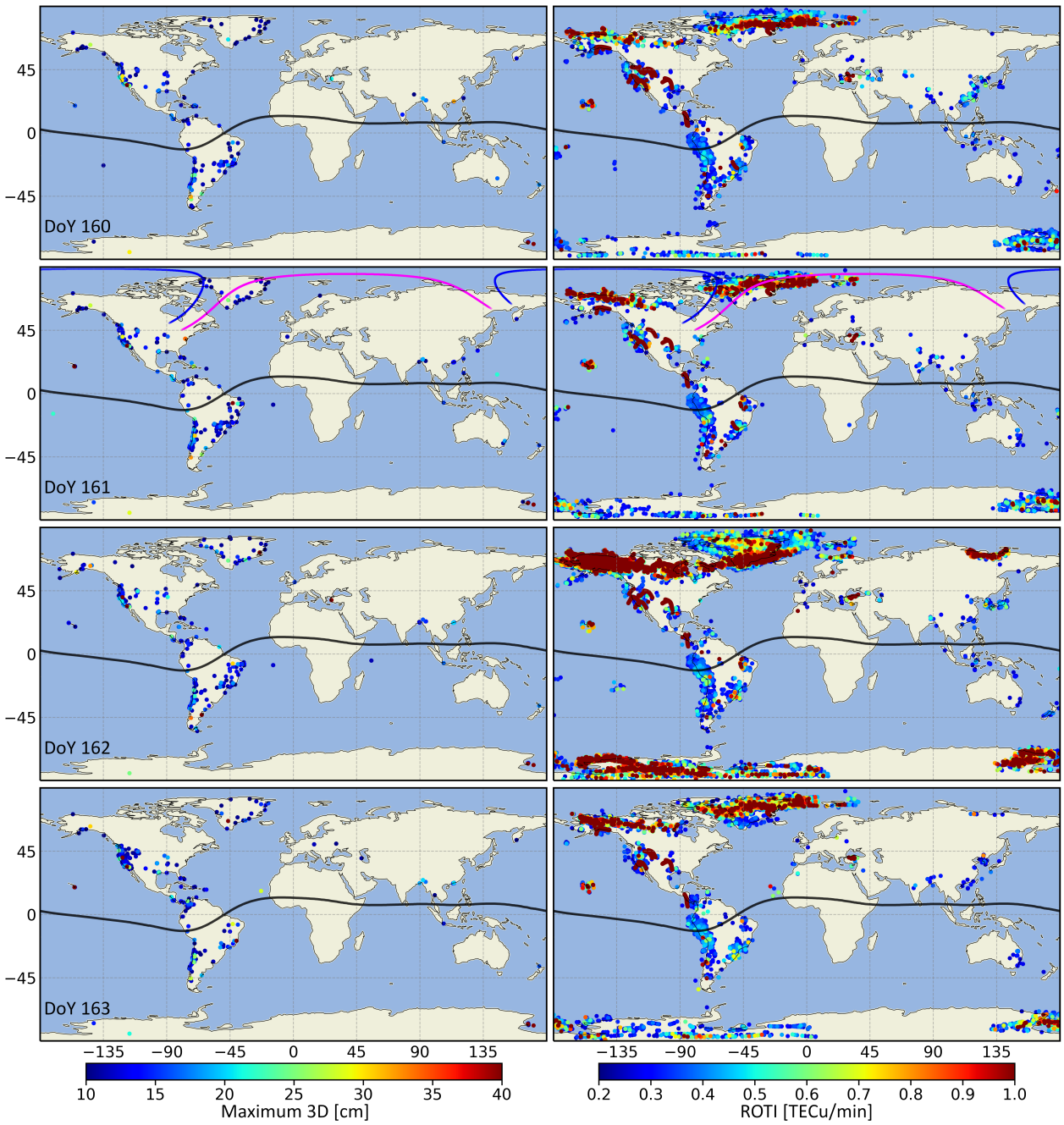

Figure 3.6: Maximum 3D positioning errors ⩾10 cm (**left panels**); and ROTI ⩾0.25 TECu/min (**right panels**) between 8 and 14 UT. From top to bottom shows DoYs 160–163. Annular eclipse path at ground level (blue line), and at 350 km of altitude (magenta line) are also shown.

The TEC data (e.g., Figure 3.3) and the derived PPP-AR (see Figure 3.6 (left panels)), and Figure 3.7) show that there are two regions where the errors are more severe during the solar eclipse (DoY 161, between 8 and 14 UT). These regions are Greenland and South America. For this reason, we focused this study on these sectors.

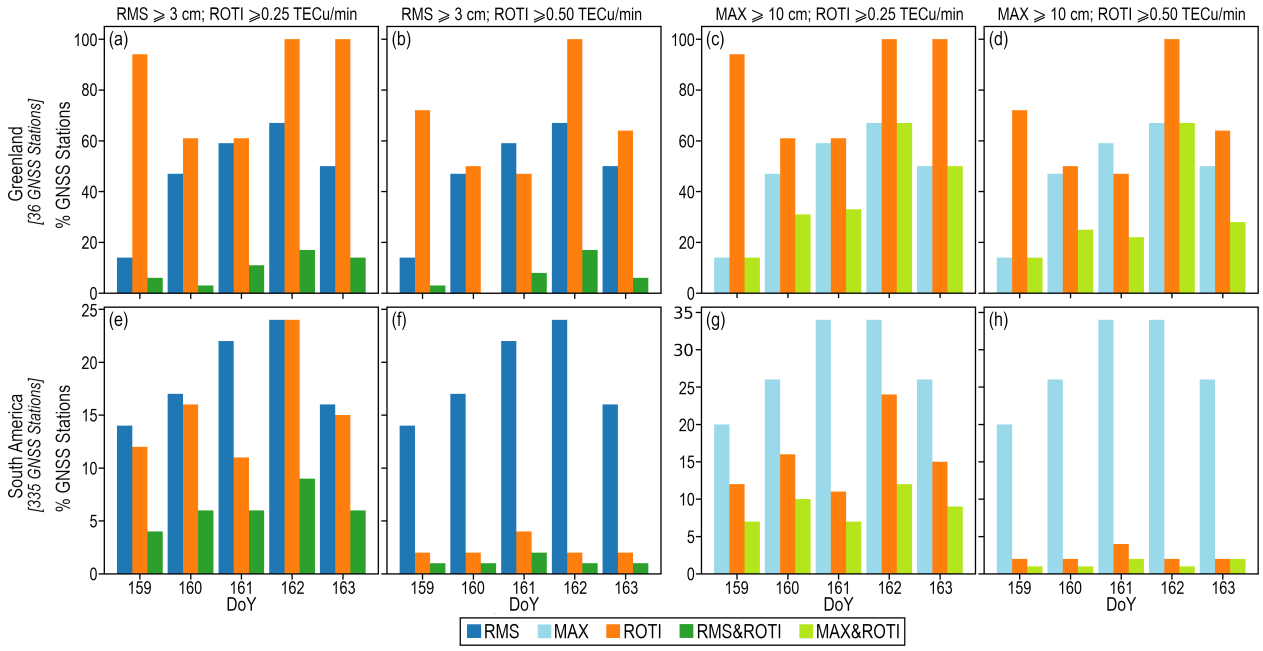

Figure 3.7: Behavior of the maximum 3D positioning error, 3D-RMS, and ROTI in Greenland and South America sectors, where 36 GNSS stations are localized in Greenland (**upper panels**) and 335 GNSS stations are situated in South America (**bottom panels**). Percentage of GNSS stations where (**a**,**b**,**e**,**f**) 3D-RMS $\geqslant$ 3 cm; (**c**,**d**,**g**,**h**) maximum 3D position $\geqslant$ 10 cm; (**a**,**c**,**e**,**g**) ROTI $\geqslant$ 0.25 TECu/min; and (**b**,**d**,**f**,**h**) ROTI $\geqslant$ 0.50 TECu/min. Percentage of GNSS stations meeting 3D-RMS (blue bars); maximum 3D positioning error (light blue bars); ROTI (orange bars); 3D-RMS and ROTI (green bars); and maximum 3D positioning error and ROTI (light green bars) values.

In the Greenland and South America regions, we can find 36 ($\sim$2%) and 335 ($\sim$14%) of the 2337 total available GNSS stations, respectively. We determined the percentage of stations localized in both regions that had errors that fell at certain intervals during the time period of the annular eclipse (between 8 and 14 UT). Figure 3.7 shows the percentages of stations that meet the thresholds of maximum 3D positioning error, 3D-RMS, and ROTI. We determined the number of GNSS stations based on ROTI activity and positioning values (see Annex B, Tables B.2,B.3,B.4, where each column in these tables represents the percentage of stations with maximum 3D position error, 3D-RMS, and ROTI at certain intervals in the selected period).

Figure 3.5 shows in more detail the percentage of stations with maximum 3D errors $\geqslant$10 cm on eclipse day. In Greenland, during the inicial period of the eclipse ($\sim$P1 time), the percentage of stations with maximum 3D positioning error rises to 60%. Subsequently, the value remains at $\sim$28% until it increases to $\sim$33% between 10.5 and 11.25 UT (around GE time). The value then returns to $\sim$28% until 14 UT (after P4 time), when it drops to $\sim$11% of stations. In South America, the percentage of stations with maximum 3D positioning error had a maximum of $\sim$34% between 9.75 and 11.5 UT (around GE time). We also were able to observe a decrease in stations that exceeded the threshold maximum 3D positioning error from $\sim$28% to $\sim$22% between 16 and 17 UT.

3.3.3 Ionospheric Behavior and GNSS Positioning Errors by Region

To study the effects of the eclipse, we selected 24 stations from among the 2337 GNSS stations (see Figure 3.1). We chose five GNSS stations close to the annular solar eclipse (KMOR, KAGZ, MARG, IQAL, PICL). There were six GNSS stations located in the partial eclipse region (CN00, TRO1, SVTL, TIXI, MAG0, YAKT). Furthermore, we used five stations located in the Caribbean and South America (LMMF, BOAV, PIFL, MSBL). The sunrise (in PICL and CN00 stations) and the sunset (in MAG0 and YAKT stations) happened during the eclipse time window at ground level but did not take place at the ionospheric height of 350 km. More details about the GNSS stations and eclipse conditions (with respect to the ionospheric height of 350 km) can be found in Table 3.1.

Figure 3.8 presents the results of ionospheric TEC of 12 stations from among the 24 selected GNSS stations for the eclipse day (VTECe), the reference days ($\overline{VTEC}$), and the final results of DVTEC [%]. The vertical blue shaded region between P1 time and P4 time, with GE time (brown dotted line). The vertical yellow shaded region between C1 time and C4 time, with MOT (black dotted line). Each plot is shown between 5 and 23 UT. The maximum reduction values of TEC for each station are indicated in Table 3.1 (τ = 1 to 288 min, and A[%]= −65 to −27%). This eclipse occurred during the morning at most of the selected stations but took place in the afternoon at five stations (NYA1, TRO1, SVTL, TIXI, MAG0, YAKT). The Sun's activity became stronger around noon and the clear TEC reduction during the eclipse can be observed. The stations that are near the path of the annular eclipse at 350 km altitude and the east coast of Greenland reached lower values of DVTEC [%] ∼−55% than the stations with the annular eclipse at the surface level DVTEC [%] ∼−40%.

Figure 3.8 shows the ionospheric TEC changes for 12 of the 24 GNSS stations presented in Table 3.1. The TEC disturbance lasted longer at the GNSS stations located in South America and the Lesser Antilles (CN00, LMMF, CN57, BOAV, PIFL, MSBL). In these GNSS stations, the ionospheric effect caused by the eclipse started at ∼8.5–9 UT and ended ∼18–21 UT ($\Delta T > 10$ h). The ionospheric response is similar in BOAV and MSBL stations where A[%] ∼−30%. In MAG0, TIXI, and YAKT stations, we observe a TEC depletion during the eclipse time window, but it is not as noticeable as in the other cases.

Additionally, the number of GNSS stations according to ROTI activity was: 5 strong (BLAS, PIFL, LEFN, NYA1, and MARG stations), 2 moderate (KMOR and KAGZ stations) and 17 without activity (see Table 3.1).

In the same way, we presented the results of PPP-AR of 24 DF-GNSS stations during eclipse day. The time series were corrected for the common noise filter of the East, North, and Up components. The stations had variations in position within the time window of the eclipse (between 8 and 14 UT). The station with the highest positioning errors in the East, North, and Up components was PIFL stations. KAGA, GLS2, SENU, and MSBL stations also showed position variations between 5 and 8 UT.

Equation (3.6) is used to obtain the 3D results. Then, the maximum 3D positioning error and 3D-RMS values (between 8 and 14 UT) for each station are indicated in Table 3.1. We note that the GNSS stations can be separated according to the percentage of maximum 3D positioning error and 3D-RMS, with respect to the maximum values of reference days.

Table 3.1: Detail about the GNSS stations analyzed, their location, eclipse condition, magnitude and change in VTEC at each station. Eclipse characteristics (time and maximum obscuration) for the 24 selected GNSS stations. Further, we have also estimated eclipse conditions at the ionospheric height of 350 km by the method suggested by Verhulst et al. [149]. Ionosphere, 3D eclipse, and 3D non-eclipse values are between 8 and 14 UT. In 3D non-eclipse: MAX refers to the maximum 3D positioning error of the reference days, and we calculate RMS by taking all the values of the reference days between 8 and 14 UT.

GNSS Station	**Geographic**		**Eclipse**					**Ionosphere**			**3D Non Eclipse**		**3D Eclipse**	
	Lat [°N]	**Lon [°E]**	**C1 [UT]**	**MOT [UT]**	**C4 [UT]**	**MPO [%]**	τ **[min]**	**A [%]**	**A [TECu]**	**ROTI** $[\frac{\textbf{TECu}}{\textbf{min}}]$	**MAX [cm]**	**RMS [cm]**	**MAX [cm]**	**RMS [cm]**
KMOR	81.25	−63.53	9.63	10.72	11.83	84	32	−44	−1.8	0.5	9.9	1.8	12.7	2.4
KAGZ	79.13	−65.85	9.57	10.63	11.75	84	23	−43	−1.6	0.5	10.1	2	11	2
MARG	77.19	−65.69	9.5	10.57	11.68	84	7	−30	−1.0	1.1	9.5	1.8	9.4	2.1
IQAL	63.75	−68.51	9.1	10.12	11.18	85	12	−56	−3.0	0.3	4.2	1.1	5.2	1.4
PICL	51.48	−90.16	9.03	9.92	10.87	81	1	−29	−1.3	0.1	3	0.9	4.2	1.8
ALGO	45.96	−78.07	8.75	9.68	10.63	89	17	−40	−1.6	0.1	3.5	1.1	3.4	1.6
LEFN	80.46	−26.29	9.62	10.8	10.08	90	15	−55	−2.8	1.8	7.5	1.9	9.8	2.2
BLAS	79.54	−22.97	9.6	10.77	11.95	90	22	−59	−3.1	2.2	9.5	1.8	11.4	2
KAGA	69.22	−49.81	9.18	10.32	11.47	90	18	−43	−1.8	0.2	7	1.6	8.9	1.8
GLS2	69.09	−39.65	9.18	10.32	11.53	88	29	−61	−3.3	0.2	9.9	2.2	16.7	2.6
KUAQ	68.59	−33.05	9.18	10.33	11.57	84	19	−61	−3.5	0.1	7.6	1.5	12.8	1.8
SENU	61.07	−47.14	8.92	10	11.18	86	17	−49	−3.3	0.1	6.6	1.4	10.6	2.5
CN00	17.67	−61.79	8.2	8.9	9.65	26	237	−45	−5.3	0.2	11.5	2.7	7.4	2.6
LMMF	14.59	−61	8.22	8.85	9.52	19	141	−61	−4.3	0.2	7.1	2.2	6.5	3
CN57	10.84	−60.94	8.25	8.78	9.37	11	161	−50	−4.4	0.1	6.1	1.8	8	2.7
BOAV	2.85	−60.7	8.58	8.7	8.82	0.1	288	−28	−5.1	0.1	6.7	1.7	8.1	3
PIFL	−6.79	−43.04	–	–	–	–	110 [1]	−65	−11.8	1.9	24.4	6.4	74.2	8.9
MSBL	−22.11	−56.53	–	–	–	–	126 [1]	−35	−4.2	0.1	8.5	2.9	11.6	4.2
NYA1	78.93	11.87	9.77	10.97	12.18	83	6	−42	−1.9	1.4	4	1.2	4.9	1.5
TRO1	69.66	18.94	9.72	11	12.28	59	37	−52	−2.5	0.1	4.7	1.3	12.3	2.7
SVTL	60.53	29.78	9.97	11.23	12.45	33	28	−52	−3.6	0.2	4.1	1.3	4.6	1.5
TIXI	71.63	128.87	10.55	11.57	12.57	89	100	−30	−1.4	0.2	6.5	1.8	8.3	2.1
MAG0	59.58	150.76	10.72	11.63	12.52	88	110	−27	−1.5	0.1	4.2	1.2	4.9	3.9
YAKT	62.03	129.68	10.82	11.8	12.73	87	62	−38	−2.8	0.1	4.1	1.2	4.9	1.5

[1] τ refers to GE time, not to MOT.

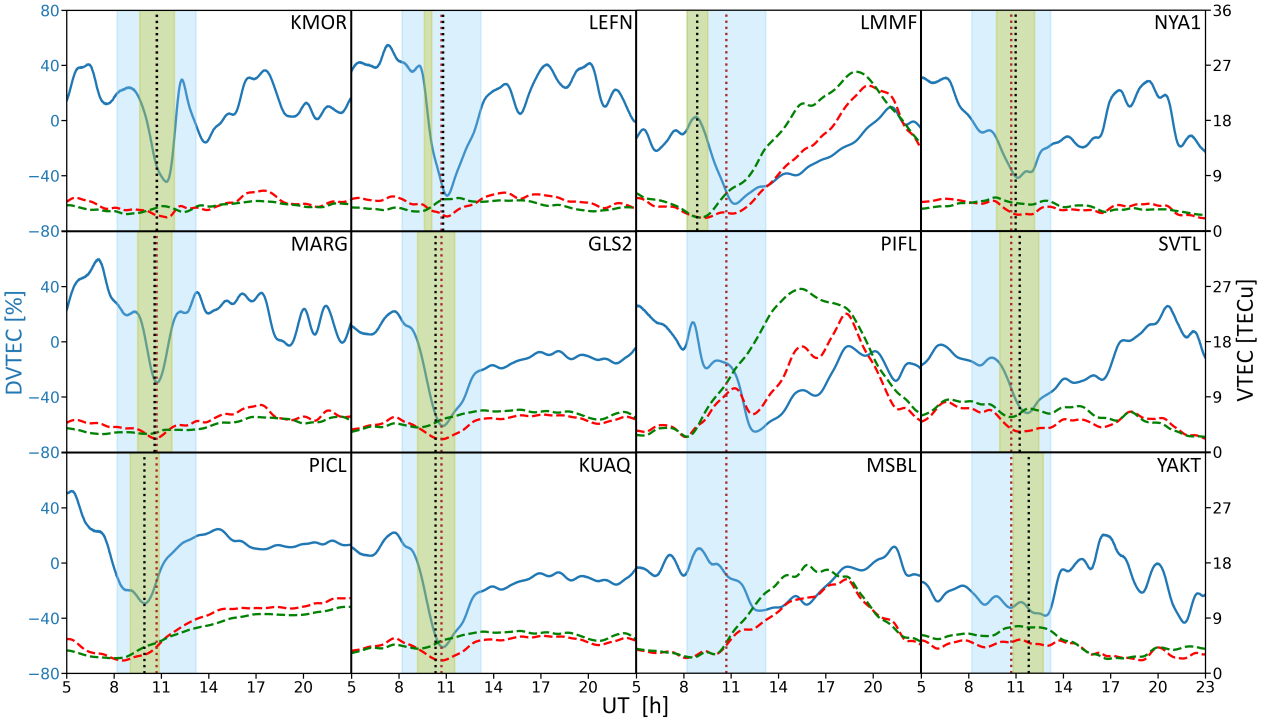

Figure 3.8: The behavior of the ionospheric TEC during the 10 June 2021 Annular Solar Eclipse in 12 of the 24 selected GNSS stations. DVTEC[%] (blue line), VTECe (red dashed line) and $\overline{VTEC}$ (green dashed line). The GNSS stations are ordered by latitude and then by longitude. P1–P4 time is represented by the light blue bar, C1–C4 time by the yellow bar, MOT by black dotted line, and GE time by the red dotted line.

In the case of maximum 3D positioning error, four stations presented values below 0% (MARG, ALGO, CN00, and LMMF); eight 0–25% (KAGZ, IQAL, BLAS, BOAV, NYA1, SVTL, MAG0, and YAKT); seven GNSS stations were between 25 and 50%; three stations were 60–70% (GLS2, KUAQ, and SENU); and two stations $>$ 100% (PIFL and TRO1).

On the other hand, for 3D-RMS in a percentage, 1 station was $<$ 0% (CN00); 11 stations were 0–25% (KAGZ, MARG, LEFN, BLAS, KAGA, GLS2, KUAQ, NYA1, SVTL, TIXI, and YAKT); 7 stations were 25–50% (KMOR, IQAL, ALGO, LMMF, CN57, PIFL, and MSBL); 3 stations were 75–100% (SENU, PICL, and BOAV); and 2 stations $>$ 100% (TRO1 and MAG0).

A Case Study

We will describe in more detail the results obtained with PIFL GNSS station (6.79°S, 43.04°W). PILF had the largest ionospheric disturbances and GNSS positioning errors (see Table 3.1). TEC depletion had values around −65% (−11.8 TECu) at 110 min after GE time (see Figure 3.8). Figure 3.9 presents the ionospheric behavior (ROT, ROTI) and kinematic DF-GNSS PPP-AR mode during DoYs 160–163 between 5 and 23 UT. We do not show DoY 159 because it does not differ significantly from DoY 160.

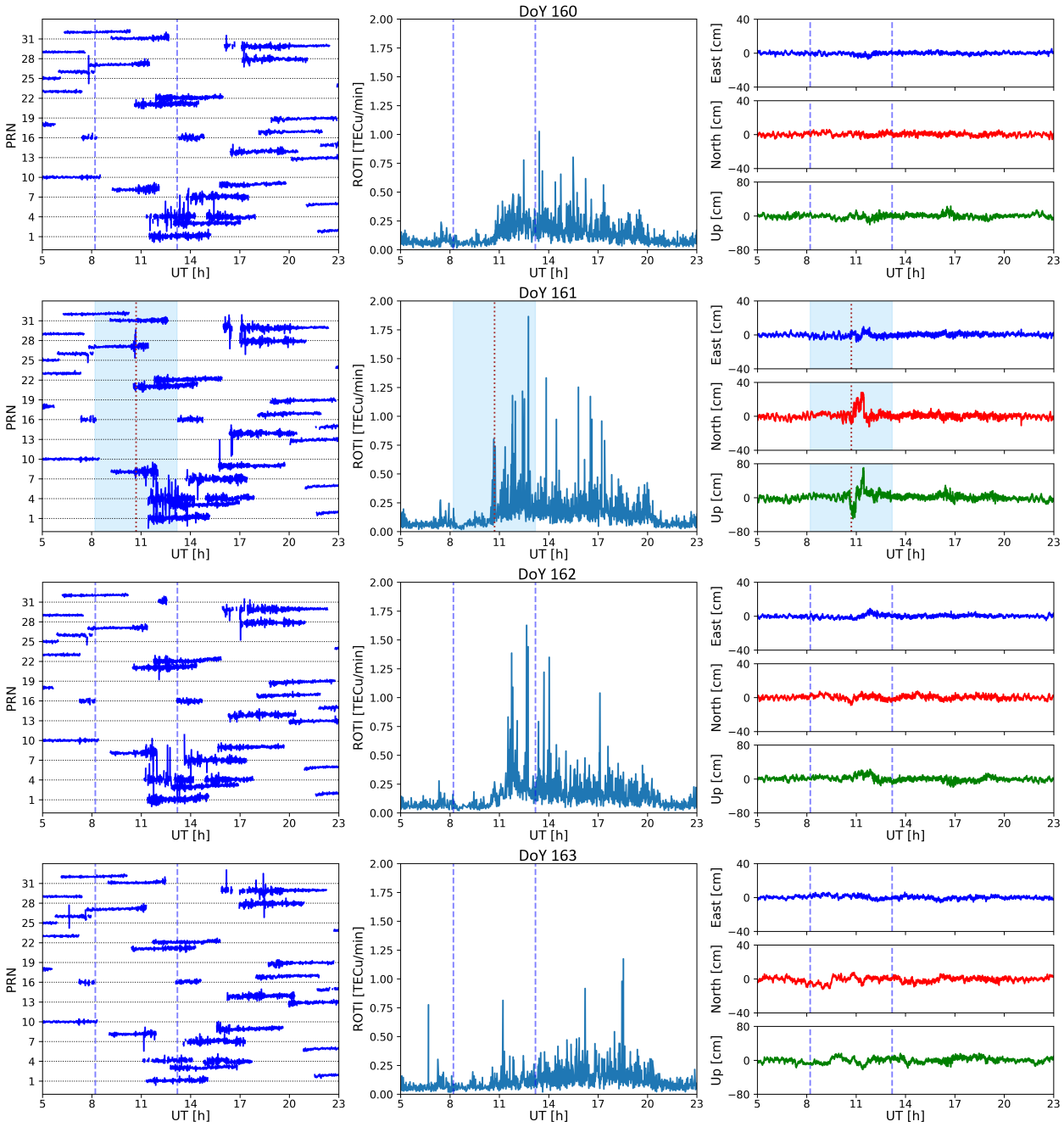

Figure 3.9: Ionospheric behavior and apparent position variation of the PIFL GNSS station. From top to bottom show DoYs 160–163. ROT (TECu/m) (**left panels**), ROTI (TECu/m) (**middle panels**), DF-GNSS PPP-AR (cm): East [cm] (blue line), North [cm] (red line), and Up [cm] (green line) (**right panels**). P1–P4 time on non-eclipse day (blue dashed lines), P1–P4 time on eclipse day (light blue bar), GE time (red dotted line).

Figure 3.9 (left, middle panels) illustrates examples of GPS ROT and GPS ROTI variations along with all visible GPS satellites. On eclipse day, we can observe a $|\mathrm{ROT}| > 1.5$ TEC/min in eight Pseudo Random Noises (PRN-4, 7, 8, 9, 14, 27, 28, 30). The $|\mathrm{ROT}|$ value was exceeded by 3–4 PRNs during the reference DoYs 159, 160, and 163. In contrast, the $|\mathrm{ROT}|$ was exceeded by seven PRNs on DoY 162 (see Figure 3.9 (left panels)).

On DoY 161 between 10.66 and 17.39 UT (6.73 h), we could note 22 and 8 ROTI values >0.5 and >1 TECu/min, respectively (see Figure 3.9 (middle panels)). The ROTI peak was 1.9 TECu/min at 12.75 UT, estimated from the PRN-4. On this day, nine PRNs (PRN-4, 7, 8, 9, 10, 14, 27, 28, 30) presented a moderate and/or strong ROTI activity. Regarding DoYs 159, 160, 162 and 163, we observed 12, 8, 20 and 6 values with moderate and/or strong ROTI activity. Then, this station showed strong TEC activity during each of the five DoYs. The ROTI value was higher on eclipse day 1.9 TECu/min at 12.76 UT (∼25 min after P4 time).

Figure 3.9 (right panels) show the apparent position variation of kinematic DF-GNSS PPP-AR mode in the East, North, and Up components for the PIFL GNSS station. These time series has been corrected for the common noise filter. On DoY 161, the apparent peak ground displacement in the East, North, and Up components were 18, 40, and 119.8 cm, respectively. Moreover, the maximum 3D positioning error ⩾10 cm ∼9.80 UT by ∼3.30 h. The Up, North, and East components are ordered from highest to lowest errors. Then, positioning errors in the three components and their results were clear during the eclipse time window (after GE time), relative to the reference days.

3.4 Discussion

In this section, we discuss the main findings regarding the 10 June 2021 annular solar eclipse. The main goal is to study the positioning errors of GNSS receivers caused by this solar eclipse. In order to verify our findings, we compare our ionospheric values with results presented for other solar eclipses over the northern polar region (9 March 1997 [29, 150]; 1 August 2008 [138]; and 20 March 2015 [133, 151]).

There are several free-to-use software available for single-station TEC estimation methods [166, 167]. We selected GPS-TEC software because it is a widely used method by the scientific community to study phenomena such as geomagnetic storms [33] and solar eclipses [168], among others. GPS-TEC software is fundamentally based on the assumption that ionospheric density depends on altitude to determine VTEC from STEC.

3.4.1 Ionospheric Behavior

The present analysis aims to show, as best as currently possible, the effects that the solar eclipse generates both in the ionosphere under the Moon's shadow as well as in the global ionosphere. The relevance of this event is that there are few of them that occur in polar regions, in this case, in the Arctic.

We have used interpolated global maps from TEC and we have calculated the difference between eclipse and reference days. The results of the TEC maps show a significant reduction under the moon's shadow, except at the CN00 station that has similar behavior to the LMMF, CN57, BOAV, and MSBL stations (see Figures 3.3 and 3.8, Table 3.1); the GNSS stations located in the region of the eclipse reaching a maximum of $\tau = 1$ to 288 min, A peak ∼−5 TECu, A[%] = −61 to −27%. Table 3.1 details these parameters for GNSS stations of some selected regions (see Figure 3.1). The values of these parameters agree with those obtained for the solar eclipses of 9 March 1997 solar eclipse [29, 150], 1 August 2008 [138],

and 20 March 2015 [133, 151].

TEC depletion was not as pronounced in the MAG0, TIXI, and YAKT stations (A[%] = −38 to −30%) compared to others GNSS stations (A[%] = −61 to −40%) with a similar percentage of obscuration (∼88%). This could be due to the fact that the sunset in MAG0, TIXI, and YAKT stations happened during the time-window of the eclipse at ground level. Moreover, the other stations were closer to the greatest eclipse (see Figures 3.1 and 3.8, Table 3.1).

In addition to the decrease of TEC in the ionosphere under the Moon's shadow, we have observed interesting and significant effects far from that region. This is the case of a significant decrease in TEC that seems to move southward from the shadow, passing through the North Atlantic, and remaining stationary for several hours over the Caribbean and the north of Brazil, at the stations CN00, LMMF, CN57, BOAV, PIFL, MSBL (see Figures 3.3 and 3.8, and Table 3.1). The delay value relative to GE time was between ∼30 and ∼168 min, A peak ∼−11 TECu, A[%] = −65 to −28%, $\Delta T > 10$ h. This area coincides with the location of the crests of EIA. The TEC variations were more intense north and south of the magnetic equator, where they were similar to those obtained at the GNSS stations located in the eclipse region.

On the other hand, applying $DVTEC_t - DVTECnew_t$, we observed that the mean was between −0.5 and 0.1 TECu; and standard deviation was less than 0.7 TECu. Therefore, TEC changes due to the weak geomagnetic activity during the DoY 162, did not cause problems in the ionospheric TEC background to our presented results for the eclipse day (see Annex B, Figure B.2, Table B.1).

In order to verify the negative disturbance in TEC on EIA crests, we have compared them with ionosonde observations of the sector involved (Figure 3.10). The Ramey (RA, 18.5°N, 67.1°W) station on the Caribbean side, and Sao Luis (SL, 2.6°S, 44.2°W), Fortaleza (FZ, 3.9°S, 38°W) and Cachoeira Paulista (CP, 22.7°S, 45.0°W) stations on the Brazil side were selected. The geographic locations of these stations are indicated with blue rhombuses in Figure 3.1. The data is obtained from the Digital Ionogram Data Base (`http://giro.uml.edu/didbase/scaled.php`, accessed on 4 August 2021) [169].

As a result, Figure 3.10 shows coherence between TEC and the critical frequency of the plasma (foF2) of each station. That is, the electron concentration after the eclipse maximum (∼11 UT) decreases (red circles) with respect to the reference curve (black line) calculated as indicated in Section 3.2.1. These same changes can be seen in the height of maximum electron concentration (hmF2). The decrease in foF2 and hmF2 is notorious at stations near the anomaly's crest (RA, FZ, CP); however, it is not very significant in the stations at the magnetic equator (SL). Moreover, similar ionospheric effects were seen in distant regions in the Moon's shadow [144, 145, 146, 147, 148, 170, 171, 172, 173, 174, 175]. Differences between foF2 and TEC may be due to the fact that foF2 was the result of the original autoscaled records, and also that TEC was calculated from a spatial average.

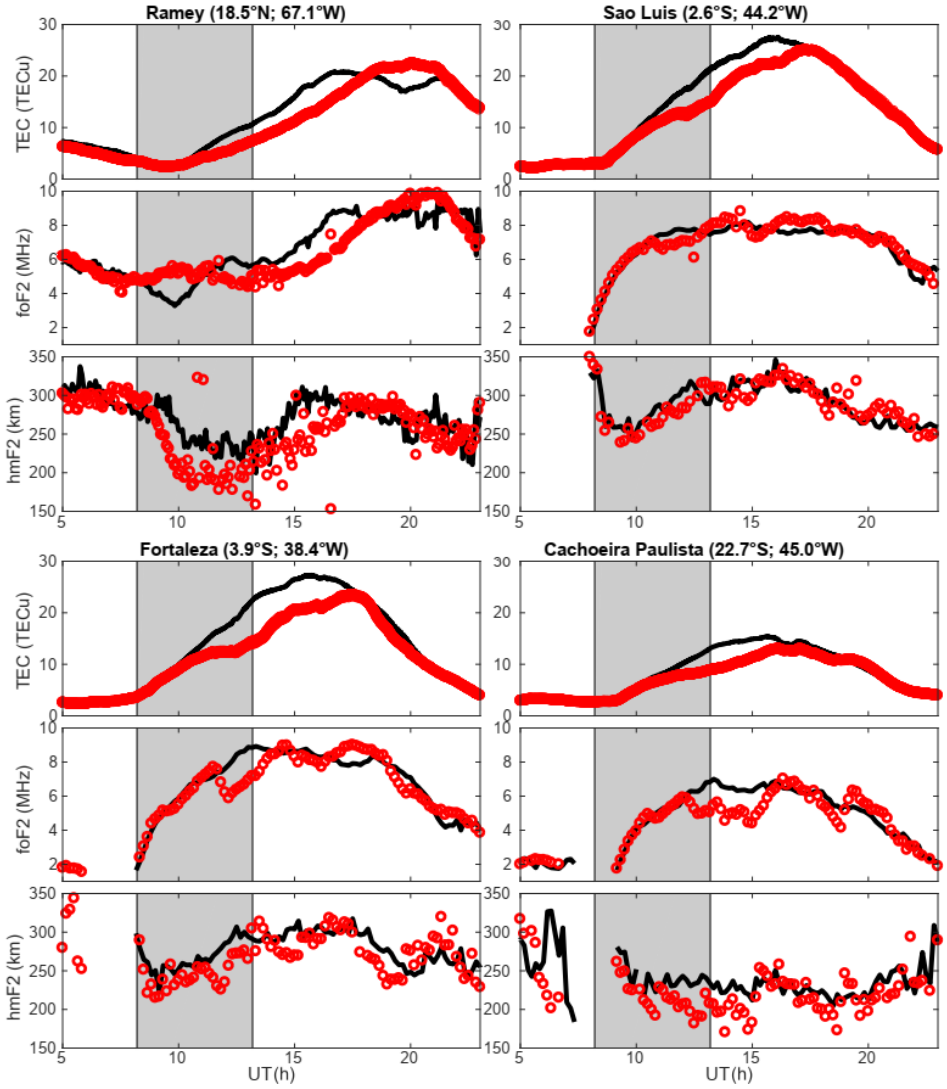

Figure 3.10: Comparison between TEC differences and differences in the critical frequency of the plasma (foF2) and its height (hmF2). Observations (red circles), reference variation (black line), and P1–P4 time (shaded interval) are shown.

A possible explanation for this phenomenon is that the eclipse could alter the thermospheric neutral wind regime and thus generate a ionospheric disturbance dynamo, which could be observed at the equator as a counter-electrojet. This counter-electrojet could be observed in the vertical drift of the plasma, for instance, the one measured by the Jicamarca incoherent radar. However, there are no measurements at Jicamarca for this period. Another way to observe is to calculate the difference in the horizontal component between an equatorial magnetometer and another in low latitude [176], or in the temporal variation of the same horizontal component of an equatorial magnetometer. In this case, neither the difference between Jicamarca (12.0°S, 76.8°W, I = 1°)—Piura (5.2°S, 80.6°W, I = 11°; available at `http://lisn.igp.gob.pe/`, last accessed on 22 May 2022), in the west coast of South America, nor the variation of the magnetometer of Kourou (5.2°N, 52.7°W; I = 13°; available at `https://intermagnet.github.io`, last accessed on 22 May 2022), in the east coast of South America shows significant variations during the eclipse day with respect to the other

days (figure not shown), which rejects this hypothesis. Another possible explanation could be that due to the fact that the partial eclipse begins at low latitudes (see Supplementary Materials, Video S1) the electron concentration never reaches normal values again. An eclipse also can cause effects on a global scale. Because the eclipse-induced abrupt cooling of the atmosphere can result in an instantaneous temperature shift and pressure differential, triggering AGWs, and associated TADs and/or TIDs. However, a detailed investigation of these causes is out of the scope of the current paper [145].

On the other hand, ionospheric effects in the magnetic conjugate of the eclipse (end of the white line in Figure 3.3, at 10.70 UT) are not possible to observe due to the lack of receivers in this region (see Figure 3.1).

On DoY 161, there was low ROTI activity in the western region of the United States of America, compared to the reference DoYs. The decrease in the percentage of GNSS stations in South America with weak ROTI activities caused the increase of stations without activity up to 89%. Then, the number of stations with strong ROTI activity only increased from 1% to 3% in this sector. However, the behavior of the ROTI activity in Greenland was less than the reference days (see Figures 3.6 and 3.7; Annex B, Table B.4).

The behavior of ionospheric TEC and ROTI shows that electrons were less active in the ionosphere during the solar eclipse (see Table 3.1, and Figures 3.3, 3.4, 3.6–3.8 and 3.10). The behavior of the ROTI in the eclipse region was consistent with that indicated by Park et al. [153]. They found a significant reduction in the ROT during the eclipse. Furthermore, eclipse day was the least ROTI active in Greenland because we were able to observe a clear reduction in ROTI values compared to the other four DoYs (see Figure 3.6 (left panels), Figure 3.7 (upper panels)).

On the other hand, as a consequence of the geomagnetic activity (AE-index $>$ 500 nT) in the polar regions from 5–15 UT on DoY 162; we can see an increase in ROTI activity (ROTI $\geqslant$ 0.25 TECu/min) that starts at the northern polar region, propagating later the increment toward the equator ($\sim$50°N), which agrees with previous studies [33, 127, 128] (see Figure 3.6 (left panels)). In South America, the percentage of stations with ROTI activity increased from $\sim$12% to 24% (see Figure 3.6 (left panels), Figure 3.7 (upper panels), and Annex B, Table B.4).

The results obtained with the GNSS stations at 350 km (see Figures 3.3 and 3.8) were consistent with the ionospheric TEC behavior at 400 km above the Swarm-A (see Figure 3.4). At P1 time, we observe a TEC depletion (~-1.7 TECu, -35%) in the central Atlantic region, where the eclipse started and its conjugate. The greatest TEC reduction (~-2 TECu, -45%) occurred at GE time (see Figure 3.4 (upper panels)). This TEC value was similar to that reported by Cherniak and Zakharenkova (-2 to -1.5 TECu) [177]. From Figure 3.4 (buttom panels), we were also able to show that the disturbance remained in the North and South American regions (TEC $\sim -30\%$) even though the eclipse was already over the northern European and Asian regions. Moreover, we can observe a close similarity in the behavior of in situ Ne and VTEC (see Figure 3.4). Furthermore, the results of ionospheric plasma depletion using Swarm-A LP were consistent with the findings presented in [177].

3.4.2 Ionospheric Impacts on GNSS Positioning Errors

The manner in which we present the positioning errors in this work was through the statistics of perturbed stations around the world and, in particular, in the Greenland and South American sectors.

On the eclipse day, we could see a slight increase in the percentage of GNSS stations around the world that exceeded both positioning thresholds compared to previous days. The main increment suffered by the maximum 3D positioning error goes from ∼8% to ∼14%. Then, Greenland and the southern sector of America were within the regions that presented GNSS stations with the highest positioning errors during the eclipse time window. This positioning behavior in both regions was consistent with the global ionospheric TEC changes.

Contrary to what happens with the activity of electrons, the percentage of stations that exceed both positioning-error thresholds was greater on DoY 161 compared to DoYs 159, 160, and 163 (see Figures 3.6 and 3.7 (upper panels)). We could see similar behavior in both cases of the 3D-RMS and ROTI activity relationships (RMS&ROTI). The eclipse day was the second DoY with the highest percentage of stations that exceeded the positioning-error thresholds. The effects of the eclipse day were only exceeded by DoY 162 due to weak geomagnetic activity (AE-index >500 nT) in the polar regions from 5 UT to 15 UT. In South America, the behavior of maximum 3D positioning error ⩾10 cm (34%) and 3D-RMS ⩾3 cm (22%) on day 161 was similar to day 162. In Greenland, these parameters were also similar on days 161 and 162, where maximum 3D positioning error ⩾10 cm was >55% and 3D-RMS ⩾ 3 cm was ∼17%. However, the effects on positioning on DoY 162 were slightly higher (see Figures 3.6 and 3.7 (bottom panels)).

Our RMS position values for the quiet days were in accordance with those from previous results [33, 129]. They showed that the precision of the post-processing kinematic PPP-AR method was ⩽0.8 and ⩽2 cm for the horizontal and vertical components, respectively. Moreover, our 3D-RMS results in percentage (⩽3 cm = −4 to 225%) are consistent with the −4 to 324% presented by Park et al. [153].

Unlike previous studies [107, 108, 109, 111], the results presented by Valdés-Abreu et al. [33], suggested that positioning errors also occur, regardless of whether the ROTI has rapid variations, with or without ROTI activity, in this type of DF-GNSS stations with the use of PPP-AR. Moreover, our results confirm that ionospheric disturbance sources can cause degradation of the GNSS accuracy (maximum 3D positioning error ⩾ 10 cm and 3D-RMS ⩾ 3 cm) when ROTI ⩾ 0.25 TECu/min, ROTI ⩾ 0.5 TECu/min, and without ROTI activity (see Table 3.1, and Figures 3.6–3.9). In addition, not all GNSS stations that had ROTI activity presented position errors.

Further, the ROTI activity–positioning variation relationship would have been met if two necessary conditions had been observed on each day in Figure 3.7. First, the positioning bars (RMS and MAX) had to be greater than or equal to the ROTI activity bar. This condition ensures that any ROTI activity causes variations in GNSS positioning. Second, the positioning ROTI bars (RMS&ROTI and MAX&ROTI) had to be the same or similar to the ROTI activity bar.

In most GNSS stations, we can observe the positioning errors were around the beginning of the TEC reduction (∼P1 time), the TEC peak (∼MOT and GE time), and/or in the final phase of the TEC recovery (see Figure 3.8). Then, we can see from one to more than three time slots with positioning errors. In general, after P1 time, the behavior of the stations with maximum 3D positioning error ⩾10 cm is similar to the DVTEC [%] of the stations located in Greenland (see Figure 3.8 (left, center left panels), Figure 3.5 (left panels)) and South America (see Figure 3.8 (center right panels), Figure 3.5 (right panel)). For example, in the Greenland region, the ionospheric TEC depletion was significant until ∼14 UT, and the recovery also could be observed in the rapid decrease from 28% to 11% of stations that exceeded the threshold of maximum 3D positioning error ∼14 UT, where the persistence of the positioning errors provoked by the 10 June 2021 annular eclipse lasted ∼6 h. Although the TEC depletion in sectors of South America could be observed until ∼19–21 UT, a ionospheric TEC enhancement was observed around 16–17 UT, similar to the behavior of the GNSS stations with a maximum 3D positioning error greater than the threshold of 10 cm (from 28% to 22% between 16 and 17 UT). Therefore, the persistence of the positioning errors provoked by the 10 June 2021 annular eclipse lasted ∼10 h.

The annular eclipse in Greenland caused significant TEC changes (∼−60%), although with low ROTI activity. However, the GNSS positioning errors are similar to those caused during a weak geomagnetic storm with high auroral activity.

From Table 3.1, Figures 3.8 and 3.9, we see that the stations (PIFL, TRO1, GLS2, KUAQ, SENU) presented maximum 3D position errors >60%, also had A[%] ⩽ −49%, but without ROTI activity (<0.25 TECu/min). PIFL station was the only one with ROTI activity over the 5-day period under consideration. Additionally, not all the stations that had A[%] ⩽ −49% got maximum 3D erros >60% (BLAS, LEFN, IQAL, SVTL, LMMF, and CN57 stations). The LMMF station presented A[%] = −61%, but maximum 3D position errors = −8%, and ROTI = 0.2 TECu/min. Although the BLAS and LEFN stations had strong ROTI activity and the IQAL station had weak ROTI activity, the percentage of maximum 3D positioning error in these stations was between 24% and 31%.

Thus, the results suggest that when maximum 3D errors >60%, with respect to the maximum of the reference days, we can find A[%] ⩽ −49%, but not the opposite. The results also reinforce the idea that ROTI activity is not a necessary condition to affect GNSS accuracy. We were not able to estimate the ionospheric effects on GNSS positioning in the magnetic conjugate region of MPO of the solar eclipse, due to the lack of GNSS stations in this region.

Our study showed that the ionospheric TEC disturbances due to the solar eclipse in the polar regions can produce disturbances in low and medium latitudes. Ionospheric changes can cause GNSS positioning errors. The estimation of these errors is critical in teleoperated and autonomous (ground, maritime, and aerial) applications and other high-precision activities. For example, mining, agriculture, and fishing are all key economic activities in Chile that are considering the use of more teleoperated or autonomous systems. If the positioning error in the GNSS receivers spikes in vehicles in these industries, it could impose a serious risk to people and infrastructure. For open-pit mines, a high error can generate a failure in the estimation of the terrace on which a vehicle is located, with the consequent risk of falling. Halting autonomous operations during some events such as eclipses can reduce potential

risks, but they can be complex for these industries. Stopping the operation for even a short period of time, such as an hour, could be prohibitively expensive. Therefore, forecasting the impact should be precise in location and duration.

3.5 Conclusions

In this work, we analyzed the ionospheric behavior during the 10 June 2021 annular solar eclipse and its impact on DF-GNSS PPP-AR accuracy. We use a large global GNSS network located around the planet to estimate the effects on positioning. This solar eclipse had a trajectory over the northern polar region. We used global ionospheric TEC maps with data gathered by ground-based GNSS stations.

The TEC maps show a noticeable depletion under the Moon's shadow, reaching A[%] $< -60\%$. Furthermore, a significant TEC decrease (A[%] $< -60\%$) can also be observed far from the ionosphere under the Moon's shadow in regions close to the crests of the EIA over the Caribbean and South America, with a duration of ΔT over 10 h. Then, percentages of the ionospheric TEC over the Caribbean and South America were similar to those obtained for GNSS stations located in the region of the eclipse. Our study also confirms that there are cases and places where the disturbance can last much longer than previously expected.

We show that TEC enhancement caused by geomagnetic activity on the day after the eclipse did not cause problems in the ionospheric TEC background to our presented results for the eclipse day. We also validated the ionospheric variations estimated with GNSS receivers through measurements from other instruments such as the Swarm-A satellite (VTEC and in situ Ne), and four ionosondes (TEC, foF2, and hmF2). The ionospheric behavior clearly demonstrates that electrons are less active in that layer during the solar eclipse. Furthermore, our results are consistent with ionospheric effects reported in similar previous solar eclipses.

This study not only analyzes the eclipse's day but also compares the effects of the ionosphere and its impact on the positioning precision with those over 2 days previous and 2 days after the day of the eclipse. The day of the eclipse was the day with the second highest percentage of stations that exceeded the selected positioning thresholds (maximum 3D positioning error $\geqslant$ 10 cm, 3D-RMS $\geqslant$ 3 cm), only surpassed by the day after, which had geomagnetic activity. The data analysis shows that the eclipse had a significant effect on GNSS precision for a long time ($\sim$10 h). The Greenland and South America sectors are within the regions that presented GNSS stations with the highest positioning errors during the eclipse time window. Moreover, both regions had the greatest ionospheric TEC decrease ($\sim -60\%$).

The ROTI variations were not relevant. Thus, the results reinforce the idea that ROTI activity is not a necessary condition to affect DF-GNSS PPP-AR accuracy. Additionally, the results suggest that when maximum 3D errors are larger than 60%, the A[%] is much less than -49%. However, the opposite is not necessarily true.

3.6 Supplementary Materials

The following are available online at https://www.mdpi.com/article/10.3390/rs14133119/s1, Video S1: Eclipse obscuration mask from P1 to P4 time at 350 km altitude. Figure S1: Ionospheric TEC maps during the 10 June 2021 Annular Solar Eclipse: the world and Northern Hemisphere polar plots. Figure S2: DVTEC[TECu] maps using the Kriging interpolation method to the eclipse day. Table S1: Mean and standard deviation for each map of Figure S2. Table S2: 3D-RMS in Greenland and South America. Table S3: Maximum 3D positioning error in Greenland and South America. Table S4: ROTI in Greenland and South America.

Conclusions

General Conclusions

This doctoral thesis provided a methodology to evaluate the degradation of the GNSS positioning accuracy caused by ionospheric disturbance sources. The new methodology allows for standardization of the data to facilitate the comparison of ionospheric behavior and GNSS positioning between different cycles and kinds of ionospheric disturbance sources. The methodology was applied to ionospheric disturbance sources. The first geomagnetic storm of Solar Cycle 25 with a Kp$\geqslant$7 and the first solar eclipse of 2021 were depicted in this thesis.

The methodology proposed is based on ionospheric TEC and ROTI using GNSS stations around the world. For the analysis, global TEC maps at each IPP were created using ordinary Kriging interpolation method. The spatial gaps of the ionosphere TEC maps were filled with this interpolation method. From TEC changes, the apparent position variation was obtained using the post-processing kinematic PPP-AR mode. To facilitate the evaluation of the apparent position variation time series, the data was processed to have an equal reference for all used data. The common noise filter was applied to each of the GNSS stations to correct the time series of the North, East, and Up components because the positioning report can provide a different reference start value for different days. The review of the occurrence of the other ionospheric disturbance sources was also proposed in the methodology. This review is important because it helps to know if the ionospheric changes and degradation of the GNSS positioning accuracy of the analyzed phenomenon are influenced by other ionospheric disturbance sources, for example, earthquakes, volcanic eruptions, tsunamis, etc.

The methodology presented was used to evaluate the main effects of the 12 May 2021 moderated geomagnetic storm on georeferencing precision. The geomagnetic storm under study can be classified as moderated in terms of Dst and strong in terms of Kp (Dst = -61 nT, Kp = 7, AE $\sim$1500 nT, and IMF-Bz <-10 nT that lasted more than 3 h). This storm was the first strong storm, in terms of Kp, of the Solar Cycle 25. More than 800 GPS stations around the globe were selected to study the ionospheric changes and positioning errors. The global impact of the storm was shown in the analysis presented. The 12 May 2021 geomagnetic storm increased the percentage of the GNSS stations with 3D positioning errors greater than or equal to 10 cm from 3% to 27% and from 7% to 59% worldwide and in South America, respectively. The GNSS inaccuracies lasted for at least 9 h. The most severe effects of GNSS positioning errors were noticed in the South American sector because more than 60% of the perturbed stations were located in this region. Previous equivalent storms that occurred on 27 March 2017 and on 5 August 2019 were used as a comparison and

to verify the methodology and findings. The comparison of the storms shows that the effects on position inaccuracies are not directly deductible from the characteristics of geomagnetic storms nor from enhancement and/or variations of the ionospheric plasma.

The methodology proposed was also used to analyze the ionospheric behavior during the first solar eclipse in 2021 and its main impact on GNSS positioning accuracy. Solar eclipses are rare events. There are few studies on the effects of the ionosphere during solar eclipses that occur over the northern polar region using GNSS technology. Moreover, few authors have analyzed the GNSS positioning errors due to the influence of solar eclipses. Therefore, the 10 June 2021 annular solar eclipse was an excellent opportunity to study the eclipse-induced effects on the ionosphere and their impact on GNSS positioning. Then, first was analyzed of the ionospheric behavior at a global scale based on 2337 GNSS stations distributed around the world, a Swarm satellite, and four digisondes since they allowed the evaluation of the effects below and far from the Moon's shadow region with a higher spatial resolution. Then, the processing of ionospheric data from LEO satellite measurements was also incorporated into the methodology proposed. Unlike previous studies about the GNSS positioning errors caused by the influence of solar eclipses, this study was focused on a global scale. A noticeable TEC depletion under the Moon's shadow, reaching ($<-60\%$) was showed in the TEC maps using GNSS. Furthermore, noticeable TEC variations were also observed in both crests of the EIA region over the Caribbean and South America, with a duration or over 10 h. The ionospheric changes estimated with GNSS stations were validated through measurements from other instruments such as the Swarm-A satellite (VTEC and in situ Ne), and digisondes (TEC, foF2, and hmF2). The ionospheric behavior clearly demonstrated that electrons were less active in that layer during the solar eclipse. Furthermore, the results were consistent with ionospheric effects reported in similar previous solar eclipses. The effects on GNSS precision were perceived not only close to the area of the eclipse but also as far as the west coast of South America (Chile) and North America (California). The number of stations with positioning errors of over 10 cm almost doubled during the event in these regions. This study also confirmed that there are cases and places where the ionospheric disturbance can last much longer than previously expected. The TEC changes and positioning errors were sustained longer ($\sim$10 h) than usually assumed.

This thesis was based on two published WoS/ISI journal papers that provided a quantitative analysis of the degradation of the GNSS positioning accuracy in magnitude and duration as a function of ionospheric disturbances caused by geomagnetic activities and a solar eclipse. RMS position values for the quiet days using the post-processing kinematic PPP-AR method were in accordance with those from previous studies ($\leqslant$0.8 and $\leqslant$2 cm for the horizontal and vertical components, respectively). During the moderate storms, the largest errors were observed between the initial and main phases and persisted for more than 1 h during the recovery phase. But, during the eclipse, the positioning errors began around the beginning of the ionospheric depletion near to the first external contact (P1 time) and lasted for more than 4 h after the and last external contact (P4 time). Moreover, although the geomagnetic activities caused magnitude errors like or greater than those caused by the solar eclipse, the convergence times of the GNSS stations were much lower. The errors were more severe during ionospheric changes in both crests of the EIA region over the Caribbean and South America, in the South Atlantic Magnetic Anomaly (SAMA), which is known in the Brazilian/Argentinian sector. However, it is also notorious that the positioning errors

were high in the Chilean sector, on the west coast of South America at the west of the Andes Mountains. Furthermore, the effects on georeferencing precision were perceived on the west coast of North America, close to the Rocky Mountains. The positioning error data showed that the horizontal coordinates are more robust to ionospheric TEC changes, although the error in the vertical component is still high. In the literature, the vertical coordinate tends to be neglected, but it might be relevant for current and future GNSS applications, such as emergency services, disaster-control sectors, defense tasks, open-pit mines, fishing, agriculture tasks, autonomous vehicles, UAVs operating autonomously, among many others. The ROTI changes were not relevant. Thus, the results reinforce the idea that ROTI activity is not a necessary condition to affect DF-GNSS PPP-AR accuracy. Additionally, the results suggest that when maximum 3D positioning errors are larger than 60%, the ionospheric TEC changes are greater than $\sim|50|\%$. However, the opposite is not necessarily true.

Future Work

Since the proposed methodology allows the standardization of the data, it will be used to analyze and quantify the errors caused by other solar eclipses and geomagnetic activities, from weak to the most intense. In addition, other types of sources of ionospheric disturbances, such as earthquakes, volcanic eruptions, solar flares, solar terminators, tsunamis, tropical cyclones, thunderstorms/lightning, and rocket launches, among others, will be added to the study. But, the methodology could be upgraded with the inclusion of analyzes such as the effects of radio signal scintillation and/or gravity wave propagation on precise positioning.

On the other hand, sudden TEC variations can cause cycle slips, which can lead to loss of lock in GNSS receivers. Then, the ambiguity success rates are reduced, as well as the positioning performance of GNSS kinematic positioning. Therefore, the occurrence of cycle slips, loss of lock, and positioning accuracy degradation in different latitudes and regions will be carefully correlated according to the magnitude and duration of the phenomenon, the seasons, and the activity of the solar cycle.

Therefore, this doctoral research will create a new research niche in various areas, such as the study and modeling of ionospheric disturbances in radio communication channels and the identification of the type of ionospheric disturbance source according to the magnitude of the positioning errors. These studies will contribute to improving GNSS positioning error correction techniques in real-time.

Bibliography

[1] Teunissen, P.; Montenbruck, O. *Springer Handbook of Global Navigation Satellite Systems*; Springer International Publishing: Cham, Switzerland, 2017, doi:10.1007/978-3-319-42928-1.

[2] Atiq, M. Historical Review of Ionosphere in Perspective of Sources of Ionization and Radio Waves Propagation. *Research & Reviews: Journal of Space Science & Technology* **2018**, *7*, pp. 28—39. Available online: https://www.researchgate.net/publication/338710842_Historical_Review_of_Ionosphere_in_Perspective_of_Sources_of_Ionization_and_Radio_Waves_Propagation.

[3] Okoh, D. GPS Modeling of the Ionosphere Using Computer Neural Networks. In *Multifunctional Operation and Application of GPS*; Rustamov, R.B., Hashimov, A. M., Eds.; IntechOpen: London, United Kingdom, 2018, doi:10.5772/intechopen.75087. Available online: https://www.intechopen.com/chapters/60259.

[4] Lue, G.; Miller, E.J. Estimating a Toronto pedestrian route choice model using smartphone GPS data. *Travel behaviour and society* **2019**, *14*, pp. 34—42.

[5] Johansson, R. E.; Adolph, S. T.; Swart, J.; Lambert, M. I. Accuracy of GPS sport watches in measuring distance in an ultramarathon running race. *International Journal of Sports Science & Coaching* **2020**, *15*, pp. 212–219, doi:10.1177/1747954119899880.

[6] Pini, M.; Marucco, G.; Falco, G.; Nicola, M.; De Wilde, W. Experimental Testbed and Methodology for the Assessment of RTK GNSS Receivers Used in Precision Agriculture. *IEEE Access* **2020**, *8*, pp. 14690–14703, doi:10.1109/ACCESS.2020.2965741.

[7] dos Santos, A.F; da Silva, R.P.; Zerbato, C.; de Menezes, P.C.; Kazama, E.H.; Paixão, C.S.S.; Voltarelli, M.A. Use of real-time extend GNSS for planting and inverting peanuts. *Precision Agriculture* **2019**, *20*, pp. 840–856, doi:10.1007/s11119-018-9616-z.

[8] Catania, P.; Comparetti, A.; Febo, P.; Morello, G.; Orlando, S.; Roma, E.; Vallone, M. Positioning Accuracy Comparison of GNSS Receivers Used for Mapping and Guidance of Agricultural Machines. *Agronomy* **2020**, *10*, 924, doi:10.3390/agronomy10070924.

[9] Pinto, R. Drones: La tecnología, ventajas y sus posibles aplicaciones. *Sonami* **2016**, pp. 1–19. Available online: https://www.sonami.cl/v2/wp-content/uploads/2016/03/09.-Drones-La-tecnologia-ventajas-y-sus-posibles-aplicaciones.pdf.

[10] Terra Drone Chile 2020. Available online: https://www.terra-drone.net/chile/ (accessed on 21 July 2020).

[11] Soloviev, A. Tight coupling of GPS, laser scanner, and inertial measurements for navigation in urban environments. In *2008 IEEE/ION Position, Location and Navigation Symposium*, **2008**, pp. 511-525, doi: 10.1109/PLANS.2008.4570059.

[12] Soloviev, A.; Van Graas, F. Use of deeply integrated GPS/INS architecture and laser scanners for the identification of multipath reflections in urban environments. In *IEEE Journal of Selected Topics in Signal Processing* **2009**, *3*, pp. 786–797, doi:10.1109/JSTSP.2009.2027796.

[13] Soloviev, A. Tight coupling of GPS and INS for urban navigation. *IEEE Transactions on Aerospace and Electronic Systems* **2010**, *46*, pp. 1731–1746, doi:10.1109/TAES.2010.5595591.

[14] Hussain, R.; Rezaeifar, Z.; Oh, H.A. Paradigm Shift from Vehicular Ad Hoc Networks to VANET-Based Clouds. *Wireless Personal Communications* **2015**, *83*, pp. 1131–1158, doi:10.1007/s11277-015-2442-y.

[15] Jamil, F.; Javaid, A.; Umer, T.; Rehmani, M.H. A comprehensive survey of network coding in vehicular ad-hoc networks. *Wireless Networks* **2017**, *23*, pp. 2395–2414, doi:10.1007/s11276-016-1294-z.

[16] Zeadally, S.; Hunt, R.; Chen, YS.; Irwin, A.; Hassan, A. Vehicular ad hoc networks (VANETS): status, results, and challenges *Telecommunication Systems* **2012**, *50*, pp. 217–241, doi:10.1007/s11235-010-9400-5.

[17] Dharaskar, B.; Dharaskar, R.; Thakare, V.M. Global positioning system forensics in vehicular Ad-hoc networks *International Journal of Advances in Electronics and Computer Science* **2015**, *2*, pp. 104–109, doi:10.13140/RG.2.2.26157.38888.

[18] Xu, C.; Gong, Z.; Niu, J. Recent developments in seismological geodesy. *Geodesy and Geodynamics* **2016**, *7*, pp. 157–164, doi:/10.1016/j.geog.2016.04.009.

[19] Codelco. Sistema GPS optimiza monitoreo en proceso de lixiviación de Codelco Gabriela Mistral. Available online: https://www.codelco.com/sistema-gps-optimiza-monitoreo-en-proceso-de-lixiviacion-de-codelco/prontus_codelco/2019-12-26/155751.html (last accessed on 19 August 2022).

[20] SONAMI. Chile Pais Minero. Available online: https://www.sonami.cl/v2/?s=gps (accessed on 21 July 2020).

[21] Holding, D. Multi-GNSS vertical total electron content estimates: Data analysis and machine learning with python to evaluate ionospheric perturbations from earthquakes. *Hold. Eng. Consult.* **2017**, *1*, pp. 5–8.

[22] Bilbao, I.R.; Monge, B.M.; Rodríguez-Caderot, G.; Sarachaga, M.H.; Radicella, S.M. Degradación del posicionamiento de precisión originada por irregularidades de plasma ecuatorial / Precise positioning accuracy degradation caused by equatorial plasma irregularities. *Física de la Tierra*, **2014**, *26*. doi:10.5209/rev_FITE.2014.v26.46974.

[23] Singh, A.K.; Siingh, D.; Singh, R.P.; Mishra, S. Electrodynamical coupling of Earth's atmosphere and ionosphere: An overview. *International Journal of Geophysics* **2011**, *2011*, doi:10.1155/2011/971302.

[24] Gao, Y. Precise Point Positioning (PPP). In *Encyclopedia of Geodesy*; Springer International Publishing: Cham, Switzerland, 2016; pp. 1–5, doi:10.1007/978-3-319-02370-0_13-1.

[25] Hamzah, S.Z.M.; Homam, M.J. The correlation between total electron content variations and solar activity. *ARPN Journal of Engineering and Applied Sciences* **2015**, *10*, pp. 9870–9875. Available online: http://www.arpnjournals.org/jeas/research_papers/rp_2015/jeas_1115_2952.pdf.

[26] Otsuka, Y.; Ogawa, T.; Saito, A.; Tsugawa, T.; Fukao, S.; Miyazaki, S. A new technique for mapping of total electron content using GPS network in Japan. *Earth, Planets and Space* **2002**, *54*, pp. 63–70, doi:10.1186/BF03352422.

[27] Blagoveshchensky, D.V.; Sergeeva, M.A.; Shmelev, Y.A. TEC Dynamics During the Intense Magnetic Storm. In *2019 Radiation and Scattering of Electromagnetic Waves (RSEMW)* **2019**, pp. 64–67, doi:10.1109/RSEMW.2019.8792746.

[28] Adekoya, B.J.; Chukwuma, V.U. Ionospheric F2 layer responses to total solar eclipses at low and mid-latitude. *Journal of Atmospheric and Solar-Terrestrial Physics* **2016**, *138–139*, pp. 136–160, doi:10.1016/j.jastp.2016.01.006.

[29] Afraimovich, E.L.; Astafyeva, E.I.; Demyanov, V.V.; Edemskiy, I.K.; Gavrilyuk, N.S.; Ishin, A.B.; Kosogorov, E.A.; Leonovich, L.A.; Lesyuta, O.S.; Palamartchouk, K.S.; et al. A review of GPS/GLONASS studies of the ionospheric response to natural and anthropogenic processes and phenomena. *J. Space Weather Space Clim.* **2013**, *3*, A27.

[30] Mendillo, M. Storms in the ionosphere: Patterns and processes for total electron content. *Rev. Geophys.* **2006**, *44*, doi:10.1029/2005RG000193.

[31] Berdermann, J.; Kriegel, M.; Banyś, D.; Heymann, F.; Hoque, MM.; Wilken, V.; Borries, C.; Heßelbarth, A.; Jakowski, N. Ionospheric response to the X9.3 Flare on 6 September 2017 and its implication for navigation services over Europe. *Space Weather*, **2018**, *16*, pp. 1604–1615, doi:10.1029/2018SW001933.

[32] SAĞIR, S.; ATICI, R.; DÖLEK, İ. Investigation of the Severe Geomagnetic Storm Effects on Ionosphere at Nighttime through ROTI. *Muş Alparslan Üniversitesi Fen Bilim. Derg.* **2018**, *6*, 603–609.

[33] Valdés-Abreu, J.C.; Díaz, M.A.; Báez, J.C.; Stable-Sánchez, Y. Effects of the 12 May 2021 Geomagnetic Storm on Georeferencing Precision. *Remote Sens.* **2022**, *14*, 38, doi:10.3390/rs14010038.

[34] Redmon, R.; Seaton, D.; Steenburgh, R.; He, J.; Rodriguez, J. September 2017's geoeffective space weather and impacts to Caribbean radio communications during hurricane response. *Space Weather.* **2018**, *16*, pp. 1190–1201, doi:10.1029/2018SW001897.

[35] Valdés-Abreu, J.C.; Díaz, M.A.; Bravo, M.; Báez, J.C.; Stable-Sánchez, Y. Ionospheric Behavior during the 10 June 2021 Annular Solar Eclipse and Its Impact on GNSS Precise Point Positioning. *Remote Sens.* **2022**, *14*, 3119, doi:10.3390/rs14133119.

[36] Evaluating Total Electron Content (TEC) Detrending Techniques in Determining Ionospheric Disturbances during Lightning Events in A Low Latitude Region. *Remote Sens.* **2021**, *13*, 4753, doi:10.3390/rs13234753.

[37] Liu, T.; Yu, Z; Ding, Z; Nie, W; Xu, G. Observation of Ionospheric Gravity Waves Introduced by Thunderstorms in Low Latitudes China by GNSS *Remote Sens.* **2021**, *13*, 4131, doi:10.3390/rs13204131.

[38] Kumar, S.; Chen, W.; Chen, M.; Liu, Z.; Singh, R.P. Thunderstorm-/lightning-induced ionospheric perturbation: An observation from equatorial and low-latitude stations around Hong Kong. *J. Geophys. Res. Space Phys.* **2017**, *122*, pp. 9032—9044, doi:10.1002/2017JA023914.

[39] Freeshah, M.; Zhang, X.; Şentürk, E.; Adil, M.A.; Mousa, B.G.; Tariq, A.; Ren, X.; Refaat, M. Analysis of Atmospheric and Ionospheric Variations Due to Impacts of Super Typhoon Mangkhut (1822) in the Northwest Pacific Ocean *Remote Sens.* **2021**, *13*, 661, doi:10.3390/rs13040661.

[40] Cahyadi, M.N.; Muslim, B.; Pratomo, D.G.; Anjasmara, I.M.; Arisa, D.; Rahayu, R.W.; Hariyanto, I.H.; Jin, S.; Muafiry, I.N. Co-Seismic Ionospheric Disturbances Following the 2016 West Sumatra and 2018 Palu Earthquakes from GPS and GLONASS Measurements. *Remote Sens.* **2022**, *14*, 401, doi:10.3390/rs14020401.

[41] Dong, Y.; Gao, C.; Long, F.; Yan, Y. Suspected Seismo-Ionospheric Anomalies before Three Major Earthquakes Detected by GIMs and GPS TEC of Permanent Stations *Remote Sens.* **2021**, *14*, 20, doi:10.3390/rs14010020.

[42] Themens, D.R.; Watson, C.; Žagar, N.; Vasylkevych, S.; Elvidge, S.; McCaffrey, A.; Prikryl, P.; Reid, B.; Wood, A.; Jayachandran, P.T. Global propagation of ionospheric disturbances associated with the 2022 Tonga volcanic eruption. *Geophys. Res. Lett.* **2022**, *49*, e2022GL098158, doi:10.1029/2022GL098158.

[43] Toman, I.; Brčić, D.; Kos, S. Contribution to the Research of the Effects of Etna Volcano Activity on the Features of the Ionospheric Total Electron Content Behaviour. *Remote Sens.* **2021**, *13*, 1006, doi:10.3390/rs13051006.

[44] Li, J.; Chen, K.; Chai, H.; Wei, G. Rapid tsunami potential assessment using GNSS ionospheric disturbance: Implications from three megathrusts. *Remote Sens.* **2022**, *14*, 2018, doi:10.3390/rs14092018.

[45] Foroodi, Z.; Alizadeh, M.; Schuh, H.; Tsai, L.C. Alternative Approach for Tsunami Early Warning Indicated by Gravity Wave Effects on Ionosphere. *Remote Sens.* **2021**, *13*, 2150, doi:10.3390/rs13112150.

[46] ITU. Rec. ITU-R P.531-14: Ionospheric propagation data and prediction methods required for the design of satellite services and systems. Technical Report, ITU Recommendations; International Telecommunications Union: Geneva, Switzerland, 2019. Available online: https://www.itu.int/rec/R-REC-P.531-14-201908-I/en (last accessed on 19 August 2022).

[47] Appleton, E. V. Two anomalies in the ionosphere. *Nature* **1946**, *157*, 3995, pp. 691–691, doi:10.1038/157691a0.

[48] Balan, N.; Liu, L. B.; Le, H. J. A brief review of equatorial ionization anomaly and ionospheric irregularities. *Earth and Planetary Physics* **2018**, *2*, 4, pp. 257–275, doi:10.26464/epp2018025.

[49] Villalobos, J.; Valladares, C. E. Statistical Analysis of TEC Distributions Observed Over South and Central America. *Radio Science* **2020**, *55*, 1, pp. e2018RS006725, doi:10.1029/2018RS006725.

[50] Nishino, M.; Makita, K.; Yumoto, K.; Rodrigues, F. S.; Schuch, N. J.; Abdu, Mangalathayil A. Unusual ionospheric absorption characterizing energetic electron precipitation into the South Atlantic Magnetic Anomaly. *Earth, Planets and Space* **2002**, *54*, 9, pp. 907–916, doi:10.1186/BF03352438.

[51] Jones, A. D.; Kanekal, S. G.; Baker, D. N.; Klecker, B.; Looper, M. D.; Mazur, J. E.; Schiller, Q. SAMPEX observations of the South Atlantic anomaly secular drift during solar cycles 22–24. *Space Weather* **2017**, *15*, 1, pp. 44–52, doi:10.1002/2016SW001525.

[52] Kovář, P.; Sommer, M. CubeSat Observation of the Radiation Field of the South Atlantic Anomaly. *Remote Sens.* **2021**, *13*, 7, 1274, doi:10.3390/rs13071274.

[53] Zakharenkova, I.; Cherniak, I.; Shagimuratov, I. Observations of the Weddell Sea Anomaly in the ground-based and space-borne TEC measurements. *Atmos. Sol. Terr. Phys.* **2017**, *161*, pp. 105–117, doi:10.1016/j.jastp.2017.06.014.

[54] Alexander, P.; Luna, D.; Llamedo, P.; de la Torre, A. A gravity waves study close to the Andes mountains in Patagonia and Antarctica with GPS radio occultation observations. *Annales Geophysicae* **2010**, *28*, 2, pp. 587–595, doi:10.5194/angeo-28-587-2010.

[55] Hierro, R.; Steiner, A. K.; de la Torre, A.; Alexander, P.; Llamedo, P.; Cremades, P. Orographic and convective gravity waves above the Alps and Andes Mountains during GPS radio occultation events – a case study. *Atmospheric Measurement Techniques* **2018**, *11*, 6, pp. 3523–3539, doi:10.5194/amt-11-3523-2018.

[56] Adebiyi, S.; Ikubanni, S.; Adebesin, B.; Joshua, B.; Adekoya, B. Variations of GPS-TEC at an African Low Latitude Station during Geomagnetic Disturbances. *Phys. Mem.-J. Theor. Appl. Phys.* **2019**, *1*, pp. 113–125.

[57] Gonzalez, W.D.; Tsurutani, B.T.; De Gonzalez, A.L.C. Interplanetary origin of geomagnetic storms. *Space Sci. Rev.* **1999**, *88*, pp. 529–562, doi:10.1023/A:1005160129098.

[58] Tsidu, G.M.; Abraha, G. Moderate geomagnetic storms of 22–25 January 2012 and their influences on the wave components in ionosphere and upper stratosphere-mesosphere regions. *Adv. Space Res.* **2014**, *54*, pp. 1793–1812, doi:10.1016/j.asr.2014.07.029.

[59] Gonzalez, W.; Joselyn, J.A.; Kamide, Y.; Kroehl, H.W.; Rostoker, G.; Tsurutani, B.; Vasyliunas, V. What is a geomagnetic storm? *J. Geophys. Res. Space Phys.* **1994**, *99*, pp. 5771–5792, doi:10.1029/93JA02867.

[60] Joshua, B.; Adeniyi, J.; Adimula, I.; Oladipo, O.; Olawepo, O.; Adebiyi, S. Ionospheric response to the storm-time disturbance of 29 May, 2010. *Adv. Space Res.* **2014**, *53*, pp. 219–225, doi:10.1016/j.asr.2013.11.003.

[61] Joshua, B.; Adeniyi, J.; Reinisch, B.; Adimula, I.; Olawepo, A.; Oladipo, O.; Adebiyi, S. The response of the ionosphere over Ilorin to some geomagnetic storms. *Adv. Space Res.* **2014**, *54*, 2224–2235, doi:10.1016/j.asr.2014.08.027.

[62] Davis, T.N.; Sugiura, M. Auroral electrojet activity index AE and its universal time variations. *J. Geophys. Res.* **1966**, *71*, pp. 785–801.

[63] Boroyev, R.; Vasiliev, M. Relationship of the ASY-H index with interplanetary medium parameters and auroral activity in magnetic storm main phases during CIR and ICME events. *Sol.-Terr. Phys.* **2020**, *6*, pp. 35–40, doi:10.12737/stp-61202004.

[64] Adebesin, B.; Ikubanni, S.; Kayode, J.; Adekoya, B. Variability of solar wind dynamic pressure with solar wind parameters during intense and severe storms. *Afr. Rev. Phys.* **2013**, *8*.

[65] Borovsky, J.E.; Shprits, Y.Y. Is the Dst index sufficient to define all geospace storms? *J. Geophys. Res. Space Phys.* **2017**, *122*, pp. 11–543, doi:10.1002/2017JA024679.

[66] Matzka, J.; Stolle, C.; Yamazaki, Y.; Bronkalla, O.; Morschhauser, A. The Geomagnetic Kp Index and Derived Indices of Geomagnetic Activity. *Space Weather.* **2021**, *19*, e2020SW002641, doi:10.1029/2020SW002641.

[67] Ferreira, A.A.; Borges, R.A. Performance Analysis of Distinct Feed-forward Neural Networks Structures on the AE Index Prediction. In Proceedings of the 2021 IEEE Aerospace Conference (50100), IEEE, Big Sky, MT, USA, 6–13 June 2021; pp. 1–7.

[68] Desai, M.V.; Shah, S.N. Impacts of intense geomagnetic storms on NavIC/IRNSS system. *Ann. Geophys.* **2018**, *61*, 557, doi:10.4401/ag-7856.

[69] Gonzalez, W.; Echer, E. A study on the peak Dst and peak negative Bz relationship during intense geomagnetic storms. *Geophys. Res. Lett.* **2005**, *32*, doi:10.1029/2005GL023486.

[70] Joshua, B.; Adeniyi, J.; Oladipo, O.; Doherty, P.; Adimula, I.; Olawepo, A.; Adebiyi, S. Simultaneous response of NmF2 and GPS-TEC to storm events at Ilorin. *Adv. Space Res.* **2018**, *61*, pp. 2904–2913, doi:10.1016/j.asr.2018.03.031.

[71] Cai, X.; Burns, A.G.; Wang, W.; Qian, L.; Solomon, S.C.; Eastes, R.W.; McClintock, W.E.; Laskar, F. Investigation of a neutral "tongue" observed by GOLD during the geomagnetic storm on May 11, 2019. *J. Geophys. Res. Space Phys.* **2021**, *126*, e2020JA028817.

[72] Yu, T.; Wang, W.; Ren, Z.; Yue, J.; Yue, X.; He, M. Middle-Low Latitude Neutral Composition and Temperature Responses to the 20 and 21 November 2003 Superstorm From GUVI Dayside Limb Measurements. *J. Geophys. Res. Space Phys.* **2021**, *126*, e2020JA028427.

[73] Verkhoglyadova, O.P.; Tsurutani, B.T.; Mannucci, A.J.; Saito, A.; Araki, T.; Anderson, D.; Abdu, M.; Sobral, J. Simulation of PPEF effects in dayside low-latitude ionosphere for the 30 October 2003, superstorm. *Wash. DC Am. Geophys. Union Geophys. Monogr. Ser.* **2008**, *181*, pp. 169–177.

[74] Inyurt, S. Investigation of Ionospheric Variations During Magnetic Storm Over Turkey. *Geomagn. Aeron.* **2020**, *60*, pp. 131–135, doi:10.1134/S0016793220010120.

[75] Liu, L.; Wan, W.; Zhang, M.L.; Zhao, B.; Ning, B. Prestorm enhancements in NmF2 and total electron content at low latitudes. *J. Geophys. Res. Space Phys.* **2008**, *113*, doi:10.1029/2007JA012832.

[76] Gao, Q.; Liu, L.B.; Zhao, B.Q.; Wan, W.X.; Zhang, M.L.; Ning, B.Q. Statistical Study of the Storm Effects in Middle and Low Latitude Ionosphere in the East-Asian Sector. *Chin. J. Geophys.* **2008**, *51*, pp. 435–443, doi:10.1002/cjg2.1234.

[77] Stankov, S.; Stegen, K.; Warnant, R. Seasonal variations of storm-time TEC at European middle latitudes. *Adv. Space Res.* **2010**, *46*, pp. 1318–1325, doi:10.1016/j.asr.2010.07.017.

[78] Sharma, S.; Galav, P.; Dashora, N.; Dabas, R.; Pandey, R. Study of ionospheric TEC during space weather event of 24 August 2005 at two different longitudes. *J. Atmos. Sol.-Terr. Phys.* **2012**, *75*, pp. 133–140, doi:10.1016/j.jastp.2011.05.006.

[79] Blagoveshchenskii, D. Effect of geomagnetic storms (substorms) on the ionosphere: 1. A review. *Geomagn. Aeron.* **2013**, *53*, pp. 275–290, doi:10.1134/S0016793213030031.

[80] Cherniak, I.; Zakharenkova, I.; Redmon, R.J. Dynamics of the high-latitude ionospheric irregularities during the 17 March 2015St. Patrick's Day storm: Ground-based GPS measurements. *Space Weather.* **2015**, *13*, pp. 585–597, doi:10.1002/2015SW001237.

[81] Fagundes, P.R.; Cardoso, F.; Fejer, B.; Venkatesh, K.; Ribeiro, B.; Pillat, V. Positive and negative GPS-TEC ionospheric storm effects during the extreme space weather event of March 2015 over the Brazilian sector. *J. Geophys. Res. Space Phys.* **2016**, *121*, pp. 5613–5625, doi:10.1002/2015JA022214.

[82] Tsurutani, B.; Mannucci, A.; Iijima, B.; Abdu, M.A.; Sobral, J.H.A.; Gonzalez, W.; Guarnieri, F.; Tsuda, T.; Saito, A.; Yumoto, K.; others. Global dayside ionospheric uplift and enhancement associated with interplanetary electric fields. *J. Geophys. Res. Space Phys.* **2004**, *109*, doi:10.1029/2003JA010342.

[83] Mannucci, A.; Tsurutani, B.; Iijima, B.; Komjathy, A.; Saito, A.; Gonzalez, W.; Guarnieri, F.; Kozyra, J.; Skoug, R. Dayside global ionospheric response to the major interplanetary events of 29–30 October 2003 "Halloween Storms". *Geophys. Res. Lett.* **2005**, *32*, doi:10.1029/2004GL021467.

[84] Lastovicka, J. Monitoring and forecasting of ionospheric space weather—effects of geomagnetic storms. *J. Atmos. Sol.-Terr. Phys.* **2002**, *64*, pp. 697–705, doi:10.1016/S1364-6826(02)00031-7.

[85] Fuller-Rowell, T.; Codrescu, M.; Rishbeth, H.; Moffett, R.; Quegan, S. On the seasonal response of the thermosphere and ionosphere to geomagnetic storms. *J. Geophys. Res.* **1996**, *101*, 2343–2353, doi:10.1029/95ja01614.

[86] Kleimenova, N.; Gromova, L.; Gromov, S.; Malysheva, L. Strong Magnetic Storm on 25–26 August 2018 with Reference to the Solar Cycle 24 Declining. *simi* **2019**, pp. 107–112, doi:10.1029/2005GL023486.

[87] Kleimenova, N.; Gromova, L.; Gromov, S.; Malysheva, L. The Magnetic Storm of August 25–26, 2018: Dayside High Latitude Geomagnetic Variations and Pulsations. *Geomagn. Aeron.* **2019**, *59*, pp. 660–667, doi:10.1134/S0016793219060070.

[88] Aa, E.; Huang, W.; Liu, S.; Ridley, A.; Zou, S.; Shi, L.; Chen, Y.; Shen, H.; Yuan, T.; Li, J.; others. Midlatitude plasma bubbles over China and adjacent areas during a magnetic storm on 8 September 2017. *Space Weather.* **2018**, *16*, pp. 321–331, doi:10.1002/2017SW001776.

[89] Teh, W.L.; Chen, W.S. Dependency of the Ionospheric Storm on the Local Time of Storm Onset in the Southeast Asia Sector. In Proceedings of the 2019 6th International Conference on Space Science and Communication (IconSpace), IEEE, Johor Bahru, Malaysia, 28–30 July 2019; pp. 9–13, doi:10.1109/IconSpace.2019.8905941.

[90] Zhang, Y.; Liu, Y.; Mei, J.; Zhang, C.; Wang, J. A Study on the Characteristics of the Ionospheric Gradient under Geomagnetic Perturbations. *Sensors* **2020**, *20*, 1805, doi:10.3390/s20071805.

[91] Wen, D.; Mei, D. Ionospheric TEC disturbances over China during the strong geomagnetic storm in September 2017. *Adv. Space Res.* **2020**, *65*, pp. 2529–2539, doi:10.1016/j.asr.2020.03.002.

[92] Fedrizzi, M.; de Paula, E.R.; Kantor, I.J.; Langley, R.B.; Santos, M.C.; Komjathy, A. Mapping the low-latitude ionosphere with GPS. *GPS World* **2002**, *13*, pp. 41–47.

[93] Batista, I.S.; Abdu, M.; Souza, J.; Bertoni, F.; Matsuoka, M.; Camargo, P.; Bailey, G. Unusual early morning development of the equatorial anomaly in the Brazilian sector during the Halloween magnetic storm. *J. Geophys. Res. Space Phys.* **2006**, *111*, doi:10.1029/2005JA011428.

[94] de Abreu, A.; Sahai, Y.; Fagundes, P.R.; Becker-Guedes, F.; de Jesus, R.; Guarnieri, F.; Pillat, V.G. Response of the ionospheric F-region in the Brazilian sector during the super geomagnetic storm in April 2000 observed by GPS. *Adv. Space Res.* **2010**, *45*, pp. 1322–1329, doi:10.1016/j.asr.2010.02.003.

[95] Nogueira, P.; Abdu, M.; Batista, I.; De Siqueira, P. Equatorial ionization anomaly and thermospheric meridional winds during two major storms over Brazilian low latitudes. *J. Atmos. Sol.-Terr. Phys.* **2011**, *73*, pp. 1535–1543, doi:10.1016/j.jastp.2011.02.008.

[96] De Siqueira, P.; De Paula, E.; Muella, M.; Rezende, L.; Abdu, M.; Gonzalez, W. Storm-time total electron content and its response to penetration electric fields over South America. *Ann. Geophys.* **2011**, *29*, pp. 1765–1778, doi:10.5194/angeo-29-1765-2011.

[97] De Abreu, A.; Sahai, Y.; Fagundes, P.; De Jesus, R.; Bittencourt, J.; Pillat, V. An investigation of ionospheric F region response in the Brazilian sector to the super geomagnetic storm of May 2005. *Adv. Space Res.* **2011**, *48*, pp. 1211–1220, doi:10.1016/j.asr.2011.05.036.

[98] Figueiredo, C.; Wrasse, C.; Takahashi, H.; Otsuka, Y.; Shiokawa, K.; Barros, D. Large-scale traveling ionospheric disturbances observed by GPS dTEC maps over North and South America on Saint Patrick's Day storm in 2015. *J. Geophys. Res. Space Phys.* **2017**, *122*, pp. 4755–4763, doi:10.1029/2006JA012013.

[99] Bravo, M.; Villalobos, C.; Leiva, R.; Tamblay, L.; Vega-Jorquera, P.; Ovalle, E.; Foppiano, A. Ionospheric Response to the Space Weather Events of 4-10 September 2017: First Chilean Observations. *Open Atmos. Sci. J.* **2019**, *13*, doi:10.2174/1874282301812010001.

[100] Macho, E.P.; Correia, E.; Paulo, C.M.; Angulo, L.; Vieira, J.A.G. Ionospheric response to the June 2015 geomagnetic storm in the South American region. *Adv. Space Res.* **2020**, *65*, pp. 2172–2183.

[101] Kuai, J.; Liu, L.; Lei, J.; Liu, J.; Zhao, B.; Chen, Y.; Le, H.; Wang, Y.; Hu, L. Regional differences of the ionospheric response to the July 2012 geomagnetic storm. *J. Geophys. Res. Space Phys.* **2017**, *122*, pp. 4654–4668, doi:10.1002/2016JA023844.

[102] Jacobsen, K.S.; Andalsvik, Y.L. Overview of the 2015 St. Patrick's day storm and its consequences for RTK and PPP positioning in Norway. *J. Space Weather Space Clim.* **2016**, *6*, A9, doi:10.1051/swsc/2016004.

[103] Yang, L.; Gao, J.; Li, Z.; Li, F.; Chen, C.; Wang, Y. New Satellite Selection Approach for GPS/BDS/GLONASS Kinematic Precise Point Positioning. *Appl. Sci.* **2019**, *9*, 5280, doi:10.3390/app9245280.

[104] Abdallah, A.; Saifeldin, A.; Abomariam, A.; Ali, R. Efficiency of using GNSS-PPP for digital elevation model (DEM) production. *Artif. Satell.* **2020**, *55*, pp. 17–28, doi:10.2478/arsa-2020-0002.

[105] Yigit, C.O. Experimental assessment of post-processed kinematic Precise Point Positioning method for structural health monitoring. *Geomat. Nat. Hazards Risk* **2016**, *7*, pp. 360–383, doi:10.1080/19475705.2014.917724.

[106] Mendez Astudillo, J.; Lau, L.; Tang, Y.T.; Moore, T. Analysing the Zenith Tropospheric Delay Estimates in On-line Precise Point Positioning (PPP) Services and PPP Software Packages. *Sensors* **2018**, *18*, 580, doi:10.3390/s18020580.

[107] Shagimuratov, I.; Chernouss, S.; Despirak, I.; Filatov, M.; Efishov, I.; Tepenitsyna, N.Y. Occurrence of TEC fluctuations and GPS positioning errors at different longitudes during auroral disturbances. *Sun Geosph.* **2018**, *13*, pp. 89–94, doi:10.31401/SunGeo.2018.01.12.

[108] Luo, X.; Gu, S.; Lou, Y.; Xiong, C.; Chen, B.; Jin, X. Assessing the performance of GPS precise point positioning under different geomagnetic storm conditions during solar cycle 24. *Sensors* **2018**, *18*, 1784, doi:10.3390/s18061784.

[109] Poniatowski, M.; Nykiel, G. Degradation of Kinematic PPP of GNSS Stations in Central Europe Caused by Medium-Scale Traveling Ionospheric Disturbances During the St. Patrick's Day 2015 Geomagnetic Storm. *Remote Sens.* **2020**, *12*, 3582, doi:10.3390/rs12213582.

[110] Yasyukevich, Y.; Vasilyev, R.; Ratovsky, K.; Setov, A.; Globa, M.; Syrovatskii, S.; Yasyukevich, A.; Kiselev, A.; Vesnin, A. Small-Scale Ionospheric Irregularities of Auroral Origin at Mid-Latitudes during the 22 June 2015 Magnetic Storm and Their Effect on GPS Positioning. *Remote Sens.* **2020**, *12*, 1579, doi:10.3390/rs12101579.

[111] Yang, Z.; Mrak, S.; Morton, Y.J. Geomagnetic Storm Induced Mid-latitude Ionospheric Plasma Irregularities and Their Implications for GPS Positioning over North America: A Case Study. In Proceedings of the 2020 IEEE/ION Position, Location and Navigation Symposium (PLANS). IEEE, Portland, OR, USA, 20–23 April 2020; pp. 234–238, doi:10.1109/PLANS46316.2020.9110132.

[112] Rajesh, P.; Lin, C.; Lin, C.; Chen, C.H.; Liu, J.; Matsuo, T.; Chen, S.P.; Yeh, W.; Huang, C. Extreme Positive Ionosphere Storm Triggered by a Minor Magnetic Storm in Deep Solar Minimum Revealed by FORMOSAT-7/COSMIC-2 and GNSS Observations. *J. Geophys. Res. Space Phys.* **2021**, *126*, e2020JA028261.

[113] Seemala, G.; Valladares, C. Statistics of total electron content depletions observed over the South American continent for the year 2008. *Radio Sci.* **2011**, *46*, doi:10.1029/2011RS004722.

[114] Piñón, D.A.; Gómez, D.D.; Smalley, R.; Cimbaro, S.R.; Lauría, E.A.; Bevis, M.G. The history, state, and future of the Argentine continuous satellite monitoring network and its contributions to geodesy in Latin America. *Seismol. Res. Lett.* **2018**, *89*, pp. 475–482, doi:10.1785/0220170162.

[115] Orus, R.; Hernandez-Pajares, M.; Juan, J.; Sanz, J. Improvement of global ionospheric VTEC maps by using kriging interpolation technique. *J. Atmos. Sol.-Terr. Phys.* **2005**, *67*, 1598–1609, doi:10.1016/j.jastp.2005.07.017.

[116] Monte Moreno, E.; García Rigo, A.; Hernández-Pajares, M.; Yang, H. TEC Forecasting Based on Manifold Trajectories. *Remote Sens.* **2018**, *10*, 988, doi:10.3390/rs10070988.

[117] Monte-Moreno, E.; Hernandez-Pajares, M.; Lyu, H.; Yang, H.; Aragon-Angel, A. Estimation of Polar Depletion Regions by VTEC Contrast and Watershed Enhancing. *IEEE Trans. Geosci. Remote. Sens.* **2021**, pp. 1–20, doi:10.1109/TGRS.2021.3060107.

[118] Yang, H.; Monte-Moreno, E.; Hernandez-Pajares, M.; Roma-Dollase, D. Real-time interpolation of global ionospheric maps by means of sparse representation. *J. Geod.* **2021**, *95*, pp. 1–20, doi:10.1007/s00190-021-01525-5.

[119] Basu, S.; Groves, K.; Quinn, J.; Doherty, P. A comparison of TEC fluctuations and scintillations at Ascension Island. *J. Atmos. Sol.-Terr. Phys.* **1999**, *61*, pp. 1219–1226.

[120] Ma, G.; Maruyama, T. A super bubble detected by dense GPS network at east Asian longitudes. *Geophys. Res. Lett.* **2006**, *33*.

[121] Ke, F.; Qi, X.; Wang, Y.; Liu, X. Statistics of ionospheric responses to Southeast Asia's typhoons during 2006–2018 using the rate of change in the TEC index. *Adv. Space Res.* **2020**, *66*, pp. 1724–1742.

[122] Harsha, P.B.S.; Ratnam, D.V.; Nagasri, M.L.; Sridhar, M.; Raju, K.P. Kriging-based ionospheric TEC, ROTI and amplitude scintillation index (S 4) maps for India. *IET Radar Sonar Navig.* **2020**, *14*, pp. 1827–1836.

[123] Zhou, W.; Gu, S.; Ge, M.; Wang, J. Analysis of the Effect of the 06-09-2017 Solar Flare on GNSS Signal and Positioning Performance. In *China Satellite Navigation Conference*; Springer: Berlin/Heidelberg, Germany, 2018; pp. 555–569.

[124] Liu, X.; Yuan, Y.; Tan, B.; Li, M. Observational Analysis of Variation Characteristics of GPS-Based TEC Fluctuation over China. *ISPRS Int. J. Geo-Inf.* **2016**, *5*, 237, doi:10.3390/ijgi5120237.

[125] Nose, M.; Iyemori, T.; Sugiura, M.; Kamei, T. Geomagnetic Dst index. *World Data Cent. Geomagn. Kyoto* **2015**, *10*, pp. 15–31, doi:10.17593/14515-74000.

[126] Matzka, J.; Bronkalla, O.; Tornow, K.; Elger, K.; Stolle, C. Geomagnetic Kp index. V. 1.0, GFZ Data Services, 2021; Available online: https://dataservices.gfz-potsdam.de/panmetaworks/showshort.php?id=escidoc:5216888 (accessed on 6 December 2021). doi:10.5880/Kp.0001.

[127] Kotulak, K.; Krankowski, A.; Froń, A.; Flisek, P.; Wang, N.; Li, Z.; Błaszkiewicz, L. Sub-Auroral and Mid-Latitude GNSS ROTI Performance during Solar Cycle 24 Geomagnetic Disturbed Periods: Towards Storm's Early Sensing. *Sensors* **2021**, *21*, 4325, doi:10.3390/s21134325.

[128] Kotulak, K.; Zakharenkova, I.; Krankowski, A.; Cherniak, I.; Wang, N.; Fron, A. Climatology Characteristics of Ionospheric Irregularities Described with GNSS ROTI. *Remote Sens.* **2020**, *12*, 2634, doi:10.3390/rs12162634.

[129] Katsigianni, G.; Loyer, S.; Perosanz, F. PPP and PPP-AR Kinematic Post-Processed Performance of GPS-Only, Galileo-Only and Multi-GNSS. *Remote Sens.* **2019**, *11*, 2477, doi:10.3390/rs11212477.

[130] Kumar, S.; Singh, A. Changes in total electron content (TEC) during the annular solar eclipse of 15 January 2010. *Adv. Space Res.* **2012**, *49*, pp. 75–82, doi:10.1016/j.asr.2011.09.017.

[131] Founda, D.; Melas, D.; Lykoudis, S.; Lisaridis, I.; Gerasopoulos, E.; Kouvarakis, G.; Petrakis, M.; Zerefos, C. The effect of the total solar eclipse of 29 March 2006 on meteorological variables in Greece. *Atmos. Chem. Phys.* **2007**, *7*, 5543–5553, doi:10.5194/acp-7-5543-2007.

[132] Singh, A.K.; Singh, R.; Veenadhari, B.; Singh, A. Response of low latitude D-region ionosphere to the total solar eclipse of 22 July 2009 deduced from ELF/VLF analysis. *Adv. Space Res.* **2012**, *50*, pp. 1352–1361, doi:10.1016/j.asr.2012.07.005.

[133] Hoque, M.M.; Wenzel, D.; Jakowski, N.; Gerzen, T.; Berdermann, J.; Wilken, V.; Kriegel, M.; Sato, H.; Borries, C.; Minkwitz, D. Ionospheric response over Europe during the solar eclipse of March 20, 2015. *J. Space Weather Space Clim.* **2016**, *6*, A36, doi:10.1051/swsc/2016032.

[134] Sun, Y.Y.; Liu, J.Y.; Lin, C.C.H.; Lin, C.Y.; Shen, M.H.; Chen, C.H.; Chen, C.H.; Chou, M.Y. Ionospheric bow wave induced by the moon shadow ship over the continent of United States on 21 August 2017. *Geophys. Res. Lett.* **2018**, *45*, pp. 538–544, doi:10.1002/2017GL075926.

[135] Paul, A.; Das, T.; Ray, S.; Das, A.; Bhowmick, D.; DasGupta, A. Response of the equatorial ionosphere to the total solar eclipse of 22 July 2009 and annular eclipse of 15 January 2010 as observed from a network of stations situated in the Indian longitude sector. *Ann. Geophys.* **2011**, *29*, pp. 1955–1965, doi:10.5194/angeo-29-1955-2011.

[136] An-hua, C.; Sheng-Bing, Y.; Ji-Sheng, X. Ionospheric responses to a total solar eclipse deduced by the GPS beacon observations. *Wuhan Univ. J. Nat. Sci.* **1999**, *4*, pp. 439–444, doi:10.1007/BF02832278.

[137] Afraimovich, E.L.; Lesyuta, O.S. Ionospheric response to the total solar eclipse of 21 June 2001. *arXiv* **2002**, arXiv:0201047.

[138] Momani, M.A.; Yatim, B.; Mohd Ali, M.A. Ionospheric and geomagnetic response to the total solar eclipse on 1 August 2008 over Northern Hemisphere. *J. Geophys. Res. Space Phys.* **2010**, *115*, A8, doi:10.1029/2009JA014999.

[139] Panda, S.K.; Gedam, S.; Rajaram, G.; Sripathi, S.; Bhaskar, A. Impact of 15 Jan 2010 annular solar eclipse on the equatorial and low latitude ionosphere over Indian region from Magnetometer, Ionosonde and GPS observations. *arXiv* **2015**, arXiv:1506.05245.

[140] Sharma, S.; Dashora, N.; Galav, P.; Pandey, R. Total solar eclipse of 22 July 2009: Its impact on the total electron content and ionospheric electron density in the Indian zone. *J. Atmos. Sol. Terr. Phys.* **2010**, *72*, pp. 1387–1392, doi:10.1016/j.jastp.2010.10.006.

[141] Tsai, H.; Liu, J. Ionospheric total electron content response to solar eclipses. *J. Geophys. Res. Space Phys.* **1999**, *104*, pp. 12657–12668, doi:10.1029/1999JA900001.

[142] Farges, T.; Le Pichon, A.; Blanc, E.; Perez, S.; Alcoverro, B. Response of the lower atmosphere and the ionosphere to the eclipse of 11 August 1999. *J. Atmos. Sol. Terr. Phys.* **2003**, *65*, pp. 717–726, doi:10.1016/S1364-6826(03)00078-6.

[143] Lei, J.; Dang, T.; Wang, W.; Burns, A.; Zhang, B.; Le, H. Long-Lasting Response of the Global Thermosphere and Ionosphere to the 21 August 2017 Solar Eclipse. *J. Geophys. Res. Space Phys.* **2018**, *123*, pp. 4309–4316, doi:10.1029/2018JA025460, doi:.

[144] Bravo, M.; Martínez-Ledesma, M.; Foppiano, A.; Urra, B.; Ovalle, E.; Villalobos, C.; Souza, J.; Carrasco, E.; Muñoz, P.R.; Tamblay, L.; et al. First Report of an Eclipse From Chilean Ionosonde Observations: Comparison with Total Electron Content Estimations and the Modeled Maximum Electron Concentration and Its Height. *J. Geophys. Res. Space Phys.* **2020**, *125*, e2020JA027923, doi:10.1029/2020JA027923.

[145] Aa, E.; Zhang, S.R.; Shen, H.; Liu, S.; Li, J. Local and conjugate ionospheric total electron content variation during the 21 June 2020 solar eclipse. *Adv. Space Res.* **2021**, *68*, pp. 3435–3454, doi:10.1016/j.asr.2021.06.015.

[146] He, L.; Heki, K.; Wu, L. Three-Dimensional and Trans-Hemispheric Changes in Ionospheric Electron Density Caused by the Great Solar Eclipse in North America on 21 August 2017. *Geophys. Res. Lett.* **2018**, *45*, pp. 10933–10940, doi:10.1029/2018GL080365.

[147] Le, H.; Liu, L.; Yue, X.; Wan, W. The ionospheric behavior in conjugate hemispheres during the 3 October 2005 solar eclipse. *Ann. Geophys.* **2009**, *27*, pp. 179–184, doi:10.5194/angeo-27-179-2009.

[148] Zhang, S.R.; Erickson, P.J.; Vierinen, J.; Aa, E.; Rideout, W.; Coster, A.J.; Goncharenko, L.P. Conjugate Ionospheric Perturbation During the 2017 Solar Eclipse. *J. Geophys. Res. Space Phys.* **2021**, *126*, e2020JA028531, doi:10.1029/2020JA028531.

[149] Verhulst, T.G.W.; Stankov, S.M. Height Dependency of Solar Eclipse Effects: The Ionospheric Perspective. *J. Geophys. Res. Space Phys.* **2020**, *125*, e2020JA028088, doi:10.1029/2020JA028088.

[150] Afraimovich, E.; Kosogorov, E.; Lesyuta, O. Effects of the 11 August 1999 total solar eclipse as deduced from total electron content measurements at the GPS network. *J. Atmos. Sol. Terr. Phys.* **2002**, *64*, pp. 1933–1941, doi:10.1016/S1364-6826(02)00221-3.

[151] Stankov, S.M.; Bergeot, N.; Berghmans, D.; Bolsée, D.; Bruyninx, C.; Chevalier, J.M.; Clette, F.; De Backer, H.; De Keyser, J.; D'Huys, E.; et al. Multi-instrument observations of the solar eclipse on 20 March 2015 and its effects on the ionosphere over Belgium and Europe. *J. Space Weather Space Clim.* **2017**, *7*, A19, doi:10.1051/swsc/2017017.

[152] Yuan, Y.; Tscherning, C.; Knudsen, P.; Xu, G.; Ou, J. The ionospheric eclipse factor method (IEFM) and its application to determining the ionospheric delay for GPS. *J. Geod.* **2008**, *82*, pp. 1–8, doi:10.1007/s00190-007-0152-2.

[153] Park, J.; Shahbazi, A.; Kim, S.K.; Oberg, R. Ionospheric Response to the Total Solar Eclipse of 21 August 2017, and Its Impact on GNSS Positioning. *J. Surv. Eng.* **2019**, *145*, 05019001, doi:10.1061/(ASCE)SU.1943-5428.0000270.

[154] Filjar, R. Horizontal GPS positioning accuracy during the 1999 solar eclipse. *J. Navig.* **2001**, *54*, pp. 293–296, doi:10.1017/S0373463301001370.

[155] Jia-Chun, A.; Ze-Min, W.; Dong-Chen, E.; Wei, S. Ionospheric Behavior During the Solar Eclipse of 22 July 2009 and Its Effect on Positioning. *Chin. J. Geophys.* **2010**, *53*, pp. 731–739, doi:10.1002/cjg2.1543.

[156] Abou-Galala, M.; Rabah, M.; Kaloop, M.; Zidan, Z.M. Assessment of the accuracy and convergence period of Precise Point Positioning. *Alex. Eng. J.* **2018**, *57*, 1721–1726, doi:10.1016/j.aej.2017.04.019.

[157] Turel, N.; Arikan, F. Probability density function estimation for characterizing hourly variability of ionospheric total electron content. *Radio Sci.* **2010**, *45*, pp. 1–10, doi:10.1029/2009RS004345.

[158] Dow, J.; Neilan, R.; Rizos, C. The International GNSS Service in a Changing Landscape of Global Navigation Satellite Systems. *J. Geod.* **2008**, *83*, pp. 191–198, doi:10.1007/s00190-008-0300-3.

[159] Piñón, D.; Gomez, D.; Smalley, B.; Cimbaro, S.; Lauría, E.; Bevis, M. The History, State, and Future of the Argentine Continuous Satellite Monitoring Network and Its Contributions to Geodesy in Latin America. *Seismol. Res. Lett.* **2018**, *89*, pp. 475–482, doi:10.1785/0220170162.

[160] Friis-Christensen, E.; Lühr, H.; Hulot, G. Swarm: A constellation to study the Earth's magnetic field. *Earth Planets Space* **2006**, *58*, pp. 351–358, doi:10.1186/BF03351933.

[161] Pignalberi, A. TITIPy: A Python tool for the calculation and mapping of topside ionosphere turbulence indices. *Comput. Geosci.* **2021**, *148*, 104675, doi:10.1016/j.cageo.2020.104675.

[162] Swarm L1b Product Definition. 2018. Available online: https://earth.esa.int/eogateway/documents/20142/37627/swarm-level-1b-product-definition-specification.pdf/12995649-fbcb-6ae2-5302-2269fecf5a08 (accessed on 15 March 2022).

[163] Swarm L2 TEC Product Description. 2017. Available online: https://earth.esa.int/eogateway/documents/20142/37627/swarm-level-2-tec-product-description.pdf/8fe7fa04-6b4f-86a7-5e4c-99bb280ccc7e (accessed on 15 March 2022).

[164] Alkan, R.M.; Erol, S.; Ozulu, I.M.; Ilci, V. Accuracy comparison of post-processed PPP and real-time absolute positioning techniques. *Geomat. Nat. Hazards Risk* **2020**, *11*, pp. 178–190, doi:10.1080/19475705.2020.1714752.

[165] De Michelis, P.; Consolini, G.; Pignalberi, A.; Tozzi, R.; Coco, I.; Giannattasio, F.; Pezzopane, M.; Balasis, G. Looking for a proxy of the ionospheric turbulence with Swarm data. *Sci. Rep.* **2021**, *11*, 6183, doi:10.1038/s41598-021-84985-1.

[166] Yasyukevich, Y.V.; Kiselev, A.V.; Zhivetiev, I.V.; Edemskiy, I.K.; Syrovatskii, S.V.; Maletckii, B.M.; Vesnin, A.M. SIMuRG: System for ionosphere monitoring and research from GNSS. *GPS Solut.* **2020**, *24*, 69, doi:10.1007/s10291-020-00983-2.

[167] Pignalberi, A.; Pietrella, M.; Pezzopane, M.; Habarulema, J. Investigating different vTEC calibration methods for data assimilation in ionospheric empirical models. *Adv. Space Res.* **2021**, *68*, pp. 2138–2151, doi:10.1016/j.asr.2020.10.040.

[168] Kundu, S.; Chowdhury, S.; Palit, S.; Mondal, S.K.; Sasmal, S. Variation of ionospheric plasma density during the annular solar eclipse on 26 December 2019. *Astrophys. Space Sci.* **2022**, *367*, 44, doi:10.1007/s10509-022-04069-y.

[169] Reinisch, B.; Galkin, I. Global Ionospheric Radio Observatory (GIRO). *Earth Planets Space* **2011**, *63*, pp. 377–381, doi:10.5047/eps.2011.03.001.

[170] Dang, T.; Lei, J.; Wang, W.; Zhang, B.; Burns, A.; Le, H.; Wu, Q.; Ruan, H.; Dou, X.; Wan, W. Global Responses of the Coupled Thermosphere and Ionosphere System to the August 2017 Great American Solar Eclipse. *J. Geophys. Res.* **2018**, *123*, pp. 7040–7050, doi:10.1029/2018JA025566.

[171] Huba, J.D.; Drob, D. SAMI3 prediction of the impact of the 21 August 2017 total solar eclipse on the ionosphere/plasmasphere system. *Geophys. Res. Lett.* **2017**, *44*, pp. 5928–5935, doi:10.1002/2017GL073549.

[172] Jonah, O.F.; Goncharenko, L.; Erickson, P.J.; Zhang, S.; Coster, A.; Chau, J.L.; de Paula, E.R.; Rideout, W. Anomalous Behavior of the Equatorial Ionization Anomaly During the 2 July 2019 Solar Eclipse. *J. Geophys. Res. Space Phys.* **2020**, *125*, e2020JA027909, doi:10.1029/2020JA027909.

[173] Martínez-Ledesma, M.; Bravo, M.; Urra, B.; Souza, J.; Foppiano, A. Prediction of the Ionospheric Response to the 14 December 2020 Total Solar Eclipse Using SUPIM-INPE. *J. Geophys. Res. Space Phys.* **2020**, *125*, e2020JA028625, doi:10.1029/2020JA028625.

[174] Sergeenko, N. Irregular Phenomena in Magnetically Conjugate Regions of the F2 Layer of the Ionosphere. *Geomagn. Aeron.* **2018**, *58*, 823–830, doi:10.1134/S0016793218060166.

[175] Reinisch, B.W.; Dandenault, P.B.; Galkin, I.A.; Hamel, R.; Richards, P.G. Investigation of the Electron Density Variation During the 21 August 2017 Solar Eclipse. *Geophys. Res. Lett.* **2018**, *45*, pp. 1253–1261, doi:10.1002/2017GL076572.

[176] Anderson, D.; Anghel, A.; Chau, J.; Veliz, O. Daytime vertical E × B drift velocities inferred from ground-based magnetometer observations at low latitudes. *Space Weather* **2004**, *2*, S11001, doi:10.1029/2004SW000095.

[177] Cherniak, I.; Zakharenkova, I. Ionospheric Total Electron Content Response to the Great American Solar Eclipse of 21 August 2017. *Geophys. Res. Lett.* **2018**, *45*, pp. 1199–1208, doi:10.1002/2017GL075989.

Annexes

Annex A. Geomagnetic Conditions During Solar Cycle 25 up to the 306th Day of the Year 2022

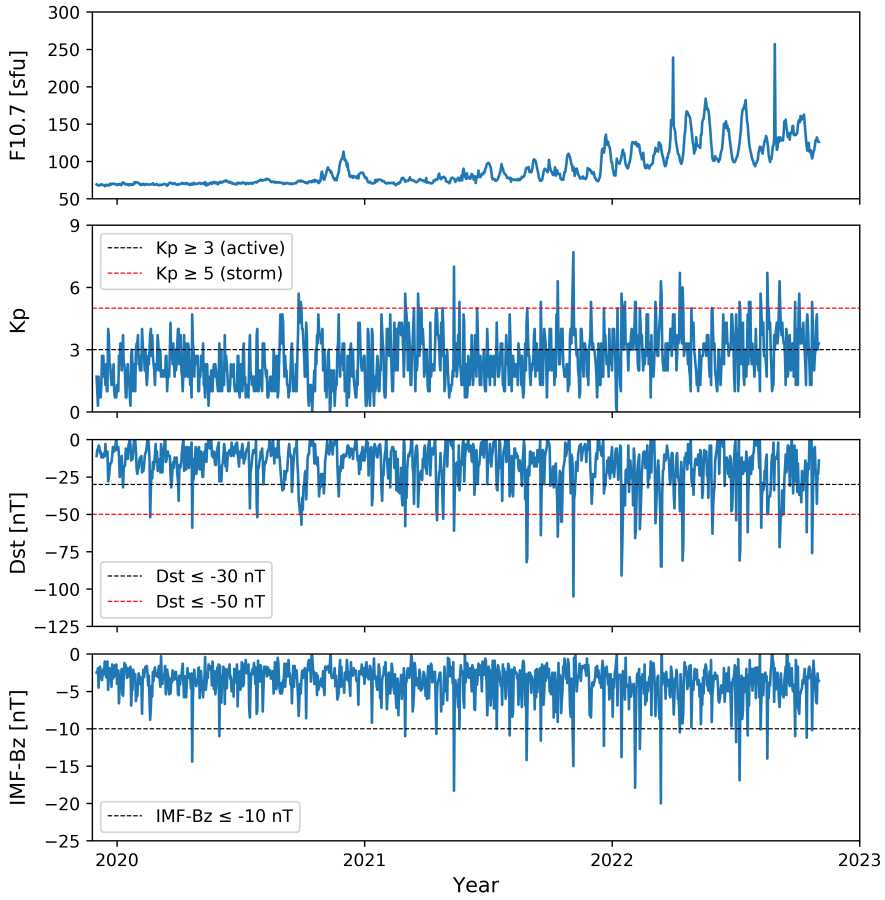

Figure A.1: Peak values for the 10.7 cm solar radio flux (F10.7 in sfu), variations of 3-hourly Kp, disturbance storm time (Dst in nT), and interplanetary magnetic field (IMF) Bz component in geocentric solar magnetospheric (GSM) coordinate (IMF-Bz in nT) indices that characterize the geomagnetic conditions during Solar Cycle 25 to the 306th day of the year 2022.

Table A.1: DoYs with geomagnetic storm levels (Kp$\geqslant$5 and/or Dst$\leqslant$-50nT) during Solar Cycle 25 to the 306th day of the year 2022. The geomagnetic data was downloaded from OMNIWeb Plus Data (https://omniweb.gsfc.nasa.gov, last accessed on 30 November 2022).

Year	**DoY**	**Kp**	**Dst [nT]**	**IMF-Bz [nT]**	**Tsw [K]**	**Vsw [km/s]**	**F10.7 [sfu]**
2020	49	3.7	−52	−8.8	26993	395	69.4
2020	111	4.7	−59	−14.4	7342	371	68.9
2020	207	4	−52	−7.5	44094	401	72.6
2020	268	5.7	−40	−8.3	45707	525	74.1
2020	270	4.7	−50	−4.0	67305	599	72.9
2020	271	5.3	−45	−5.3	47844	635	74.4
2020	272	5	−57	−3.6	144645	657	74.1
2021	60	5.7	−58	−11.0	28629	500	72.7
2021	61	5	−33	−3.9	63022	655	73.3
2021	73	5	−43	−5.0	117579	580	74.2
2021	79	5.7	−45	−3.7	30259	653	74.1
2021	84	5	−25	−4.4	34713	462	74.8
2021	106	5	−48	−10.7	22162	474	75.2
2021	107	4.7	−54	−5.1	120600	636	75.9
2021	115	5	−41	−6.6	16552	502	78.7
2021	116	4.3	−53	−6.7	68426	489	79.2
2021	132	7	−61	−18.3	25290	502	76.3
2021	140	5.3	−34	−10.0	58760	577	74
2021	166	5	−19	−4.1	19046	585	77.9
2021	239	4.3	−82	−14.2	7896	415	91.3
2021	240	5	−79	−8.2	7076	377	91.7
2021	260	5.3	−64	−11.6	23263	405	74.1
2021	285	6.3	−65	−9.1	17877	485	83.1
2021	290	4	−55	−7.9	12441	382	76.9
2021	291	3.3	−55	−6.1	12731	376	75.3
2021	307	6.3	−18	−10.7	63983	725	87.6
2021	308	7.7	−105	−15.0	7792	762	92.3
2021	334	5.3	−28	−8.5	11387	460	87.5
2021	353	5	−36	−12.3	25603	447	111.6

Continued on next page...

Table A.1 - continued from previous page.

Year	DoY	Kp	Dst [nT]	IMF-Bz [nT]	Tsw [K]	Vsw [km/s]	F10.7 [sfu]
2022	8	5	−14	−6.9	10130	398	99.1
2022	14	5.7	−91	−13.8	23054	423	106.6
2022	15	4.7	−73	−4.4	105500	567	111.8
2022	16	4.3	−50	−2.3	113047	620	115.6
2022	18	5	−34	−3.6	118773	623	110.8
2022	19	5.3	−44	−6.1	6461	696	101.9
2022	34	5.3	−66	−17.9	44274	573	122.9
2022	35	5.3	−61	−9.3	15585	578	126
2022	41	5	−60	−12.7	12465	429	114.9
2022	42	4.3	−50	−8.8	5615	568	110.2
2022	64	5.3	−56	−8.3	83053	580	118.2
2022	71	4.7	−51	−6.2	16221	406	123.1
2022	72	6.3	−85	−20.0	16904	535	121.4
2022	73	5.7	−85	2.8	5157	450	113.6
2022	100	6.7	−48	−10.5	37994	496	101.4
2022	104	6	−81	−9.3	23625	546	104
2022	105	5	−71	−7.9	32337	660	111
2022	117	5	−26	−9.8	48515	479	143.4
2022	147	5	−38	−9.1	24783	465	116.7
2022	148	5	−63	−5.5	126108	543	104.5
2022	183	4.7	−54	−11.8	10095	355	103.6
2022	188	5.3	−81	−16.9	14265	404	125.3
2022	189	5	−74	−8.9	14735	417	133.9
2022	200	4.7	−62	−10.9	12001	488	148.8
2022	202	5.3	−24	−6.9	40807	451	125.6
2022	204	5.3	−23	−4.0	121479	649	114.1
2022	219	5.7	−30	−10.1	13996	573	119.4
2022	220	5	−59	−6.7	165143	616	116.2
2022	229	6.7	−50	−14.0	9569	524	125.7
2022	230	5	−49	−4.7	178595	608	119.4
2022	231	5	−39	−5.9	122336	705	107.9
2022	246	5	−35	−6.1	33719	575	125.6
2022	247	6.3	−72	−7.1	176649	717	130.4
2022	248	5	−60	−5.2	106530	688	132.4
2022	250	3.7	−51	−4.8	137434	611	128.1
2022	253	3.3	−50	−5.8	57234	483	137.7
2022	270	5.3	−28	−11.0	48846	657	135.1
2022	276	5.7	−37	−8.0	129690	544	155.3
2022	287	4.3	−62	−11.2	25883	440	119.9
2022	295	5.3	−76	−10.2	24999	388	103.9

Annexes

Annex B. Supplementary Materials: Ionospheric Behavior During the 10 June 2021 Annular Solar Eclipse and Its Impact on GNSS Precise Point Positioning

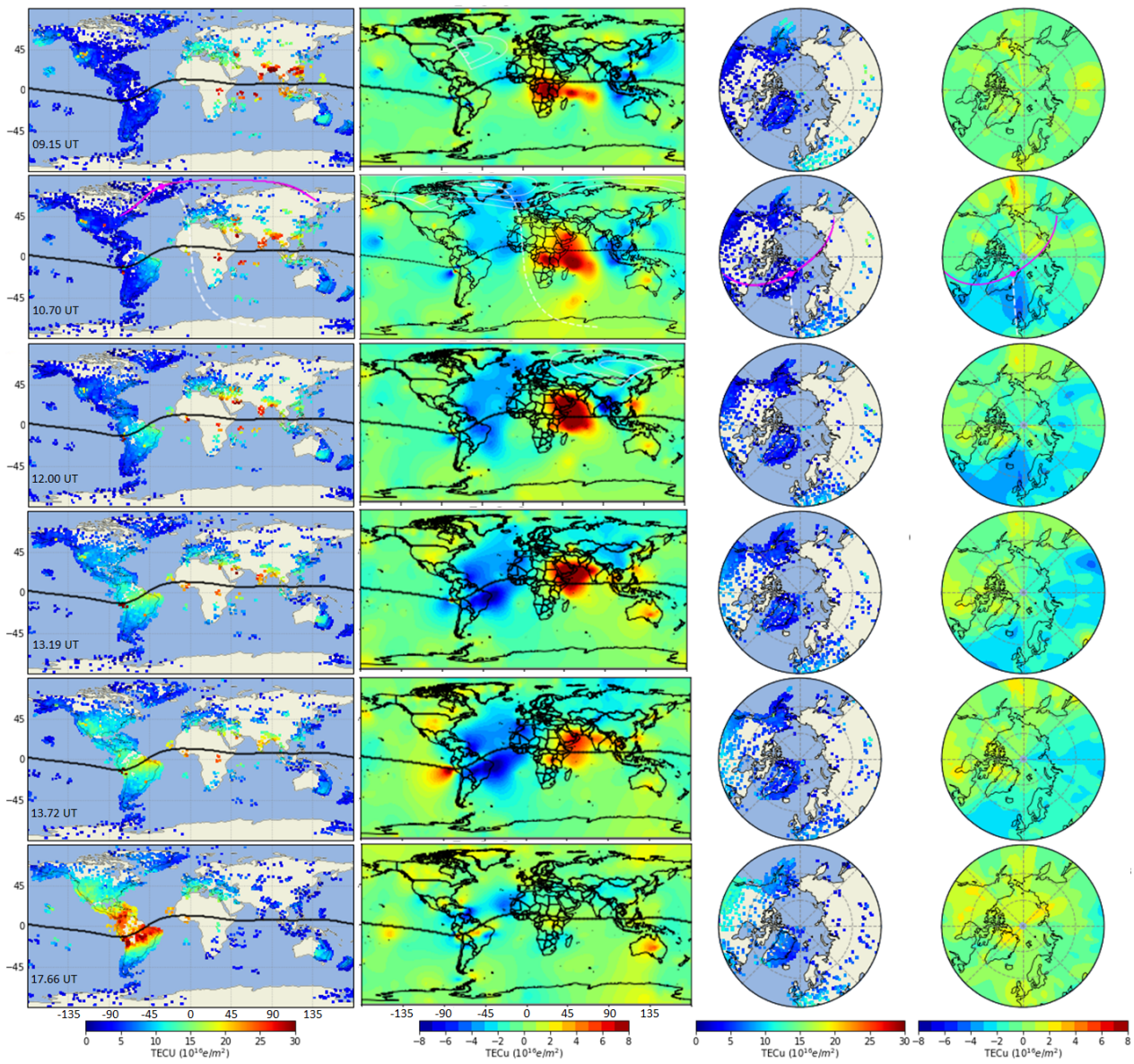

Figure B.1: Ionospheric TEC maps during the 10 June 2021 Annular Solar Eclipse. World in cylindrical equidistant projection (**left, center-left panels**); and Northern Hemisphere polar plots between 45° N and 90° N (**right, center-right panels**). VTECe at IPP (**left, center-right panels**). DVTEC[TECu] using the Kriging interpolation method (**center-left, right panels**). From top to bottom panels: 09.15 UT, 10.70 UT (GE time), 12.00 UT, 13.19 UT (P4 time), 13.72 UT, and 17.66 UT. Eclipse obscuration mask from 20% obscuration and with intervals of 20% (white line), annular eclipse path (magenta line) and the maximum obscuration (magenta dot) at 350 km altitude are also shown. The white dashed line start from the maximum obscuration of the solar eclipse to its conjugate location in the southern hemisphere at 350 km altitude.

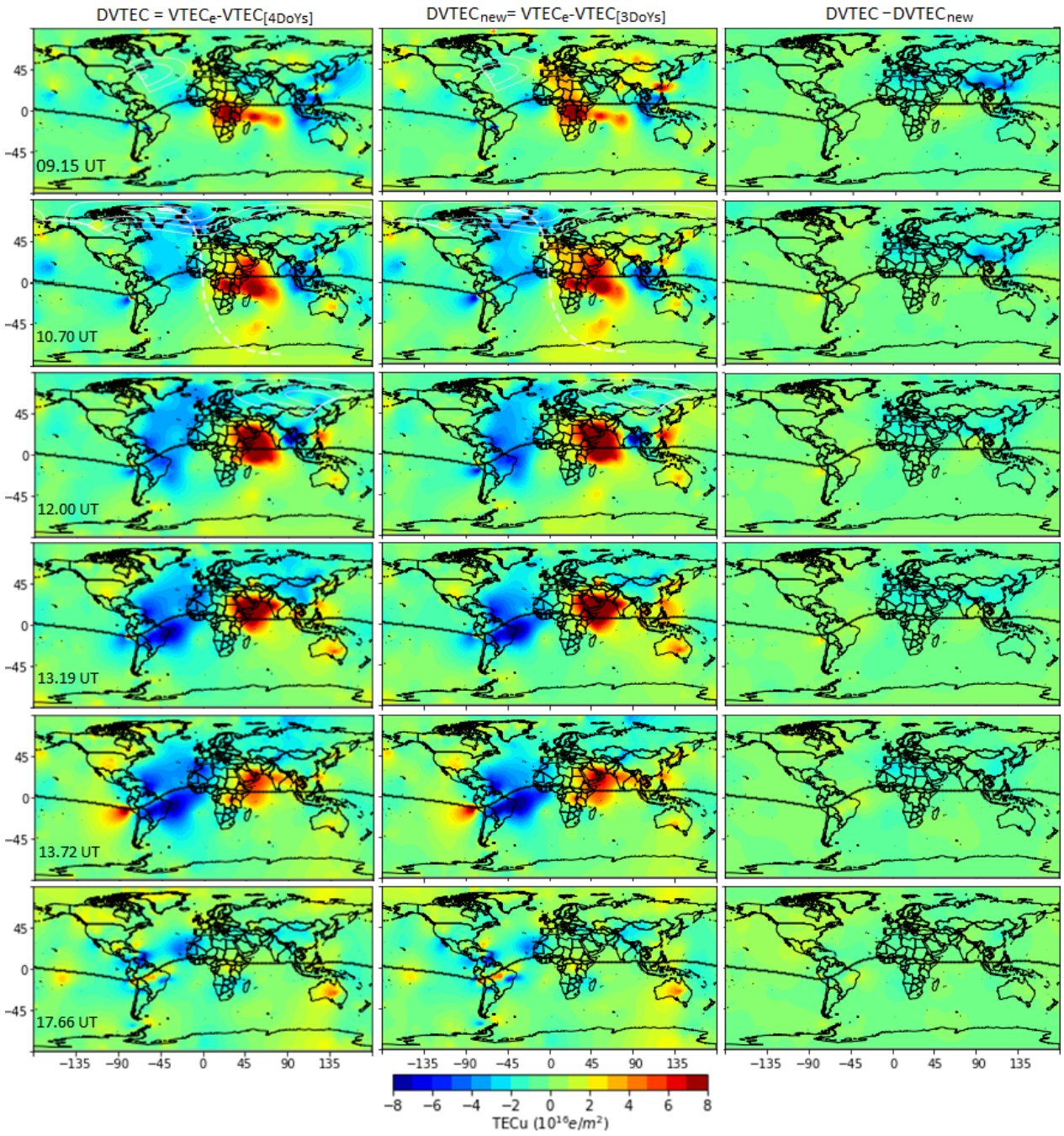

Figure B.2: DVTEC[TECu] maps using the Kriging interpolation method to the eclipse day. DVTEC estimated with four reference days (DoYs 159, 160, 162, and 163) (**left panels**). DVTECnew calculated with three reference days (DoYs 159, 160, and 163), without the DoY 162 (**middle panels**). DVTEC-DVTECnew (**right panels**). From top to bottom panels: 09.15 UT, 10.70 UT (GE time), 12.00 UT, 13.19 UT (P4 time), 13.72 UT, and 17.66 UT. Eclipse obscuration masks from 20% obscuration and with intervals of 20%, at 350 km altitude (white line) are shown. The white dashed line start from the maximum obscuration of the solar eclipse to its conjugate location in the southern hemisphere.

Table B.1: Mean and standard deviation for each map of Figure B.2 (right panels).

DVTEC - DVTECnew Map	**Mean [TECu]**	**Standard Deviation [TECu]**
09.15 UT	-0.43	0.67
10.70 UT	-0.30	0.64
12.00 UT	-0.25	0.52
13.15 UT	-0.25	0.46
13.72 UT	-0.21	0.45
17.66 UT	0.01	0.39

Table B.2: 3D-RMS, Greenland (36 stations), South America (335 stations). Where each column represents the percentage of stations with 3D-RMS in certain intervals between 8–14 UT.

Region	**RMS**	**Percentage of GNSS Stations on DoYs**				
	Intervals [cm]	**159 [%]**	**160 [%]**	**161 [%]**	**162 [%]**	**163 [%]**
Greenland	$3D<2$	28	31	2	5	0
	$2\leqslant 3D<3$	67	64	81	78	86
	$3\leqslant 3D<4$	3	3	14	11	11
	$4\leqslant 3D<5$	0	0	0	0	0
	$3D\geqslant 5$	2	2	3	6	3
South America	$3D<2$	32	30	17	20	33
	$2\leqslant 3D<3$	54	53	61	56	51
	$3\leqslant 3D<4$	9	11	13	16	10
	$4\leqslant 3D<5$	3	4	6	5	4
	$3D\geqslant 5$	2	2	3	3	2

Table B.3: Maximum 3D positioning error, Greenland (36 stations), South America (335 stations). Where each column represents the percentage of stations with maximum 3D positioning error in certain intervals between 8–14 UT.

Region	**MAX**	**Percentage of GNSS Stations on DoYs**				
	Intervals [cm]	**159 [%]**	**160 [%]**	**161 [%]**	**162 [%]**	**163 [%]**
Greenland	3D<5	0	0	0	0	0
	5⩽3D<10	86	53	41	33	50
	10⩽3D<20	8	44	56	58	47
	20⩽3D<40	6	3	3	6	0
	3D⩾40	0	0	0	3	3
South America	3D<5	8	8	8	7	7
	5⩽3D<10	72	66	58	59	67
	10⩽3D<20	19	24	31	32	24
	20⩽3D<40	1	2	3	2	2
	3D⩾40	0	0	0	0	0

Table B.4: Maximum ROTI, Greenland (36 stations), South America (335 stations). Where each column represents the percentage of stations with a maximum ROTI in certain intervals between 8–14 UT.

Region	**ROTI**	**Percentage of GNSS Stations on DoYs**				
	Intervals [TECu/min]	**159 [%]**	**160 [%]**	**161 [%]**	**162 [%]**	**163 [%]**
Greenland	0.25<ROTI	6	39	39	0	0
	0.25⩽ROTI<0.5	22	11	14	0	36
	0.5⩽ROTI<1	28	19	8	28	17
	ROTI⩾1	44	31	39	72	47
South America	0.25<ROTI	88	84	89	76	85
	0.25⩽ROTI<0.5	10	14	7	22	13
	0.5⩽ROTI<1	1	1	1	1	1
	ROTI⩾1	1	1	3	1	1